1-1-2012

The Integrin Equilibrium: Balancing Protein-Protein and Protein-Lipid interactions

David Thomas Moore
University of Pennsylvania, dtm@mail.med.upenn.edu

The Integrin Equilibrium: Balancing Protein-Protein and Protein-Lipid interactions

Abstract

On circulating platelets, the integrin fibrinogen receptor &alphaIIb&beta3 favors inactive conformations. Platelets rapidly activate &alphaIIb&beta3 to bind fibrinogen, mediating a platelet clot. Resting &alphaIIb&beta3 is stabilized by interactions between the &alphaIIb and &beta3 transmembrane domains. Binding of talin-1 and kindlin-3 to the integrin cytoplasmic domain stabilizes separation of the TMs and receptor activation. Src family kinases are needed for transmission of extracellular signals into the cell. We have sought to better understand how signals are transmitted across the &alphaIIb&beta3 TM domain. First we characterized the structure and dynamics of the active and inactive integrin cytoplasmic domain to determine how motifs that bind talin-1 and kindlin-3 are affected by the integrin activation state and the membrane environment. The &alphaIIb&beta3 cytoplasmic domain is disorded, while the &beta3 subunit contains two &alpha-helices, which interact with the phospholipid bilayer. The close proximity of &alphaIIb to &beta3 in the inactive state induces a kink that projects the &beta-chain parallel to the membrane surface. This kink is likely to stabilize interactions between helices in &beta3 with the membrane and possibly compete with binding to talin-1 and kindlin-3. The &beta3 cytoplasmic domain becomes increasingly dynamic further from the membrane, suggesting that distal kindlin-3 binding residues should be more accessible to interact with their binding partners. We also studied the interaction between talin-1 and the &beta3 cytoplasmic domain to determine how the membrane environment affects formation of the talin-1/&beta3 complex. The membrane significantly increases the affinity of talin-1 for &beta3, but that the ternary integrin/talin-1/membrane complex is not significantly more stable than the talin-1/membrane complex alone. We also performed preliminary experiments characterizing the interaction between &alphaIIb&beta3 and both kindlin-3 and c-Src. Unlike talin-1, kindlin-3 does not require the membrane to bind the integrin cytoplasmic domain with high affinity. The interaction between c-Src and the integrin was extremely weak suggesting that it might require colocalization through other interactions. Finally, we developed a simplified model showing how thermodynamic coupling between integrin subunits might allow &alphaIIb&beta3 to adopt multiple activation states.

Degree Type
Dissertation

Degree Name
Doctor of Philosophy (PhD)

Graduate Group
Biochemistry & Molecular Biophysics

First Advisor
William F. DeGrado

Keywords
Hemostasis, Integrin, Protein-lipid interactions, Protein-protein interactions, Receptor, Transmembrane

Subject Categories
Biochemistry | Biophysics

THE INTEGRIN EQUILIBRIUM: BALANCING PROTEIN-PROTEIN AND

PROTEIN-LIPID INTERACTIONS

David T. Moore

A DISSERTATION

in

Biochemistry and Molecular Biophysics

Presented to the Faculties of the University of Pennsylvania

in Partial Fulfillment of the Requirements for the

Degree of Doctor of Philosophy

2012

Supervisor of Dissertation

W F DeGrado

William F. DeGrado, Professor of Pharmaceutical Chemistry, University of California, San Francisco

Graduate Group Chairperson

_____

Kathryn M. Ferguson, Associate Professor of Biochemistry and Biophysics

Dissertation Committee

Joel S. Bennett, Professor of Medicine

Rebecca G. Wells, Associate Professor of Medicine

John W. Weisel, Professor of Cell and Developmental Biology

Carol J. Deutsch, Professor of Physiology

Mark A. Lemmon, Professor of Biochemistry and Biophysics

Gregory A. Caputo, Assistant Professor of Chemistry and Biochemistry, Rowan University

Dedicated to my family.

ACKNOWLEDGEMENTS

ABSTRACT

THE INTEGRIN EQUILIBRIUM: BALANCING PROTEIN-PROTEIN AND

PROTEIN-LIPID INTERACTIONS

David T. Moore

William F. DeGrado

On circulating platelets, the integrin fibrinogen receptor αIIbβ3 favors

inactive conformations. Platelets rapidly activate αIIbβ3 to bind fibrinogen,

mediating a platelet clot.   Resting αIIbβ3 is stabilized by interactions

between the αIIb and β3 transmembrane domains. Binding of talin-1 and

kindlin-3 to the integrin cytoplasmic domain stabilizes separation of the

TMs and receptor activation. Src family kinases are needed for

transmission of extracellular signals into the cell. We have sought to

better understand how signals are transmitted across the αIIbβ3 TM

domain. First we characterized the structure and dynamics of the active

and inactive integrin cytoplasmic domain to determine how motifs that

bind talin-1 and kindlin-3 are affected by the integrin activation state and

the membrane environment. The αIIb cytoplasmic domain is disorded,

while the β3 subunit contains two α-helices, which interact with the

phospholipid bilayer. The close proximity of αIIb to β3 in the inactive state induces a kink that projects the β-chain parallel to the membrane surface. This kink is likely to stabilize interactions between helices in β3 with the membrane and possibly compete with binding to talin-1 and kindlin-3. The β3 cytoplasmic domain becomes increasingly dynamic further from the membrane, suggesting that distal kindlin-3 binding residues should be more accessible to interact with their binding partners. We also studied the interaction between talin-1 and the β3 cytoplasmic domain to determine how the membrane environment affects formation of the talin-1/β3 complex. The membrane siginificantly increases the affinity of talin-1 for β3, but that the ternary integrin/talin-1/membrane complex is not significantly more stable than the talin-1/membrane complex alone. We also performed preliminary experiments characterizing the interaction between αIIbβ3 and both kindlin-3 and c-Src. Unlike talin-1, kindlin-3 does not require the membrane to bind the integrin cytoplasmic domain with high affinity. The interaction between c-Src and the integrin was extremely weak suggesting that it might require colocalization through other interactions. Finally, we developed a simplified model showing how thermodynamic coupling between integrin subunits might allow αIIbβ3 to adopt multiple activation states.

Table of Contents

List of Tables

List of Figures

Chapter 1 Background

I. Introduction

In multicellular organisms, integral membrane proteins mediate adhesion and signal transduction across the plasma membrane. Such processes are often dynamically regulated and reversible, suggesting that they can be described as linked equilibria. Changes in conformation, oligomeric state, or protein-protein contacts in extracellular, transmembrane (TM), and cytoplasmic domains can shift the equilibrium between different receptor functional states and transmit information across the membrane. In order to develop effective therapies to target signaling receptors, these equilibria must be understood to prevent undesired side effects. The importance of understanding these processes is illustrated by the platelet fibrinogen receptor integrin, αIIbβ3. Small molecules that mimic fibrinogen successfully block ligand binding to αIIbβ3, but stabilize active receptor conformations, resulting in either a paradoxical prothrombotic state or clearance of platelets and severe bleeding. In the following chapters, the regulation of αIIbβ3 is discussed. In particular, we focus on the mechanisms of transmembrane signal transduction and how coupled protein-protein and protein-lipid interactions allow multidomain receptors such as αIIbβ3 to integrate multiple signals to produce surprisingly diverse functions.

II. Platelet integrins.

Platelets are highly specialized cell fragments that are released from bone marrow megakaryocytes and are necessary for normal arterial clotting (4). Functional thrombocytopenia in the presence of normal platelet counts results from loss of the platelet fibrinogen receptor integrin αIIbβ3. The integrin αIIbβ3 mediates formation of the platelet clot and patients whose platelets lack normal αIIbβ3 function present with the bleeding diathesis Glanzmann thrombasthenia (5, 6). Severe bleeding can also result in patients with normal platelet counts and functional integrins via loss of signal transduction molecules that regulate the αIIbβ3 (7-10). Finally, a decreased number of circulating platelets (thrombocytopenia) can result from spurious activation of the receptor by small molecules or autoimmune antibodies (11).

Resting platelets circulate with αIIbβ3 in an inactive conformation. In the presence of damaged vasculature, numerous signals are integrated by the platelet, culminating in the activation of αIIbβ3, which binds fibrinogen and von Willebrand's factor to form a platelet plug (12). The integrin family of receptors is ubiquitously expressed in metazoa (13). Functional receptors are heterodimeric, composed of α and β subunits (Figure 1.1). Each subunit has a large ectodomain, a single transmembrane domain, and a relatively short cytoplasmic domain. In

humans, there are eighteen α-chains and eight β-chains that combine to form 24 integrin heterodimers. Although these receptors are differentially expressed, recognize unique ligands, and occupy distinct functional niches, they contain common structural elements. In particular the transmembrane and cytoplasmic domains are highly conserved, consistent with their importance in regulating integrin function through protein-protein interactions (14).
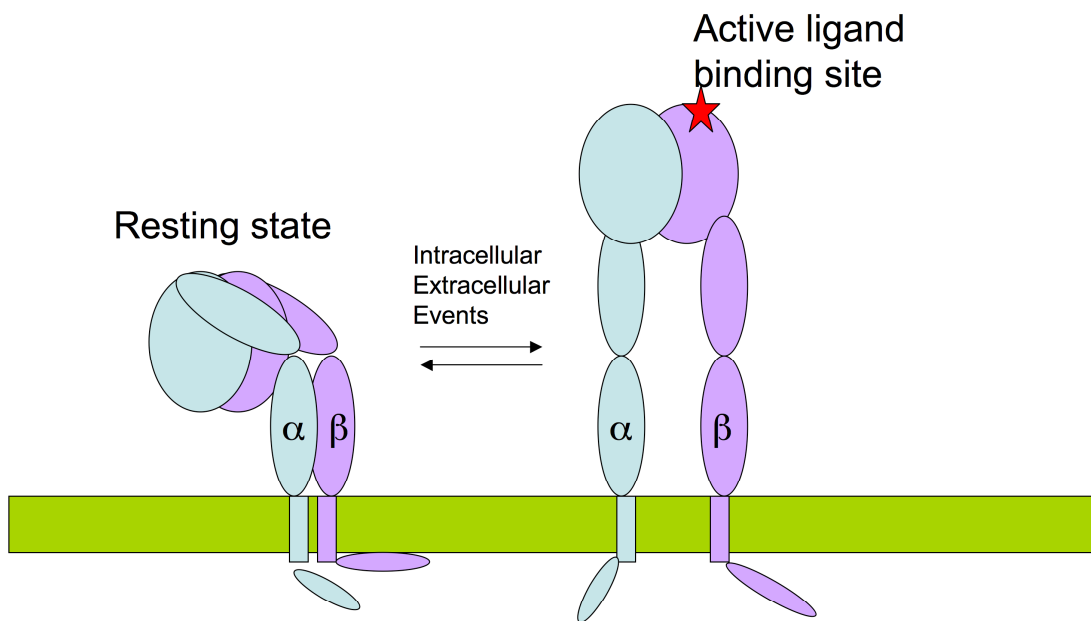
Figure 1.1 Simplified integrin equilibrium.

Integrins are in equilibrium between inactive (left) and active (right) states. This equilibrium is modulated by both intracellular and extracellular events. Integrins possess highly modular domain structures that communicate between each other establishing an elaborate coupled equilibrium. Interactions between the intregrin TM domains stabilize the

inactive conformation. Soluble factors can bind to each modular subdomain and shift the equilibrium between states.

On a resting platelet, the transmembrane and membrane-proximal domains of inactive αIIbβ3 form an extended heterodimeric interface (15-17). Activation of αIIbβ3 requires TM domain separation. This separation is dramatic (100 Å) and propagates to the ectodomain, stabilizing significant conformational changes that allow ligand binding (18). The term "inside-out signaling" refers to the classical mode of integrin activation in which intracellular signaling molecules bind to the integrin cytoplasmic domain and stabilize separation of the α and β TM domains, which results in subsequent activation of the extracellular ligand binding site. However, αIIbβ3 can also be activated through extracellular interactions. This suggests that the activation state of αIIbβ3 can be described as a linked equilibrium in which intracellular, TM, and cytoplasmic conformational states are coupled and either stabilized or destabilized by interactions with other molecules.

Inside-out activation requires the evolutionarily related talin and kindlin protein families (19, 20). There are two talin paralogs (talin-1 and 2) and three kindlin paralogs (kindlin-1, 2, and 3). In platelets, αIIbβ3 requires talin-1 and kindlin-3 only (21) (22). Patients who lack kindlin-3 function have Leukocyte Adhesion Deficiency III (LAD-III) in which platelets are unable to activate αIIbβ3 and immune cells are unable to activate β2 integrins resulting in both severe bleeding and impaired

4

immune function (7-10). Both talins and kindlins contain phospholipid binding domains, suggesting that their interactions with the inner leaflet may play a role in the regulation of αIIbβ3.

Integrin "outside-in signaling" can refer to one of two processes. The first is stabilization of an active integrin conformation by extracellular ligands. The second refers to signaling events downstream of integrin activation and ligand binding. Generally, these events require integrin oligomerization and involve recruitment of a number of signaling molecules including Src-family kinases (SFKs) (23). However, the dynamics of the signaling complexes remains an area of active research.

Talin and kindlin are members of the membrane-binding FERM (band 4.1/Ezrin/Radixin/Moesin) domain family. Their interactions with the αIIbβ3 cytoplasmic domains are likely to occur simultaneously with binding to the plasma membrane. Therefore, any equilibrium description of integrin protein-protein interactions must include interactions with the inner membrane leaflet. For simplicity, interactions between soluble proteins and the inner leaflet can be divided into two categories. First, proteins can bind using a combination of nonspecific electrostatic interactions with lipid head groups and hydrophobic interactions through insertion of hydrophobic side chains (24, 25). Second, there are a host of domains that differentiate between lipid head groups with a spectrum of specificity (26). However, "non-specific" electrostatics are likely to play a role in even "specific" head group recognition as lipid binding domains are often

positively charged and the inner leaflet of the plasma membrane is greater than 20% negatively-charged phosphatidylserine (PS).

The majority of negatively-charged lipids reside on the inner leaflet of the plasma membrane bilayer. PS is the most prevalent monovalent anionic lipid in mammalian cells and platelets, representing greater than 20% of the inner leaflet (26). The distribution of PS is asymmetric and it is actively transported from outer leaflet to the cytosolic face of the plasma membrane. During apoptosis or platelet activation, PS redistributes such that roughly half is on both the outer and inner leaflets. Exposed PS serves as an inflammatory nidus and a site for the assembly of clotting factor complexes.

The laboratories of Honig, McLaughlin, and Murray have developed models for negatively charged bilayers containing monovalent lipids (27, 28). They found that the molar partition coefficient varies exponentially with the percentage of PS (28, 29), *i.e.* the ΔG of association is linear with percentage charged lipid concentration. These experiments were extended to the interaction of the myristoylated anchor of c-Src a kinase involved in outside-integrin signaling. While the myristoyl tail produced significant thermodynamic driving force for membrane association, electrostatics increased the affinity significantly (29). Phosphoinositides are negatively-charged lipids that exist in much lower concentrations than phosphatidylserine, but are more dynamically regulated to produce local concentrations of specific lipids to regulate signal transduction (26). As

6

they contain a number of phosphates, they are negatively-charged and contribute a significant amount of electrostatic driving force to protein-lipid interactions (24). Their ability to support highly specific protein-lipid interactions is dependent on the phosphate geometry at different locations on the inositol ring and can be differentiated with surprising precision (26, 30).

Several lines of evidence suggest that PtdIns(4,5)P_2, plays a significant role in integrin regulation and the turnover of integrin complexes (31) (32). Likewise, it has been suggested that an interaction between talin-1 and PtdIns(4,5)P_2 directly competes with autoinhibitory interactions between the integrin binding FERM domain and its C-terminal rod domain (33). The talin FERM domain binds directly to the C-terminus of phosphatidylinositol-4-phosphate-5-kinase-γ (PIP5KIγ), a lipid kinase that generates PtdIns(4,5)P_2 from PtdIns(4)P, suggesting that talin may recruit PtdIns(4,5)P_2 to integrin signaling complexes. However, PIP5KIγ knockout cell lines continue to support inside-out integrin activation, but exhibit loss of integrity under mechanical stress (34), suggesting that PtdIns(4,5)P_2 may recruit secondary signaling molecules or simply reinforce talin-lipid interactions under mechanical shear.

Chapter 2 NMR analysis of the αIIb β3 cytoplasmic interaction suggests a mechanism for integrin regulation.

Abstract

The integrin αIIbβ3 is a transmembrane (TM) heterodimeric adhesion receptor that exists in equilibrium between resting and active ligand binding conformations. In resting αIIbβ3, the TM and cytoplasmic domains of αIIb and β3 form a heterodimer that constrains αIIbβ3 in its resting conformation.   To study the structure and dynamics of the cytoplasmic domain heterodimer, we prepared a disulfide-stabilized complex consisting of portions of the TM domains and the full cytoplasmic domains. NMR and hydrogen-deuterium exchange of this complex in micelles showed that the αIIb cytoplasmic domain is largely disordered, but it interacts with and influences the conformation of the β3 cytoplasmic domain. The β3 cytoplasmic domain consists of a stable proximal helix contiguous with the TM helix and two distal amphiphilic helices.   To confirm the NMR structure in a membrane-like environment, we studied the β3 cytoplasmic domain tethered to phospholipid bilayers. Hydrogen-deuterium exchange mass spectrometry and circular dichroism spectroscopy demonstrated that the β3 cytoplasmic domain becomes more ordered and helical under these conditions, consistent with our NMR

results. Further, these experiments suggest that the two distal helices associate with lipid bilayers, but undergo fluctuations that would allow rapid binding of cytoplasmic proteins regulating integrin activation, such as talin-1 and kindlin-3. Thus, these results provide a framework for understanding the kinetics and thermodynamics of protein interactions involving integrin cytoplasmic domains and suggest that such interactions may act in a concerted fashion to influence integrin stalk separation and exposure of extracellular ligand binding sites.

I. Introduction

Integrins, ubiquitous heterodimeric adhesion receptors, reside on cell surfaces in equilibrium between resting low-affinity and active high-affinity conformations. Interactions involving the transmembrane (TM) and cytoplasmic domains of integrin α and β subunits maintain the low affinity conformation, whereas intracellular signaling events disrupt these interactions, resulting in global conformational changes that activate the integrin (18). Following ligand binding, integrins cluster into complexes that initiate intracellular signaling pathways (35).

On circulating platelets, the integrin $\alpha IIb\beta 3$ is maintained in a resting conformation until platelets encounter vascular damage where it is rapidly shifted to its active conformation. This enables $\alpha IIb\beta 3$ to mediate platelet aggregation by binding soluble ligands such as fibrinogen and von Willebrand factor (5). Activation occurs when intracellular proteins such as talin-1 and kindlin-3 bind to conserved motifs in the $\beta 3$ cytoplasmic

domain, thereby disrupting TM and cytoplasmic domain heterodimers (19). It has been proposed that membrane-proximal αIIb and β3 cytoplasmic domain sequences form an activation-constraining "clasp", featuring a salt-bridge between αIIb Arg995 and β3 Asp723 (36). However, studies specifically designed to detect this salt bridge have failed to do so (37).

Although structures for the αIIbβ3 cytoplasmic domain heterodimer have been determined using soluble peptides and NMR, they may not reflect native contacts because they fail to account for constraining TM interactions (38, 39). To investigate the structure and dynamics of the cytoplasmic domain heterodimer as it exists in resting αIIbβ3, we covalently trapped the complex by introducing an inter-subunit disulfide bond near the C-terminal ends of the αIIb and β3 TM helices. The location of the crosslink was based on a computational model of the αIIbβ3 TM heterodimer (40). While this work was in progress, three structures for the αIIbβ3 TM heterodimer plus short segments of the cytoplasmic domains were reported, confirming the model used to guide the introduction of the disulfide bond (15-17).

We used NMR and hydrogen-deuterium exchange (HDX) mass spectrometry to study the structure and dynamics of the αIIbβ3 cytoplasmic domain heterodimer in micelles and phospholipid bilayers. The αIIb cytoplasmic domain was largely disordered, but the β3 cytoplasmic domain consisted of a proximal helix contiguous with the TM helix and two distal helices. The conformation of the proximal helix was

influenced by the presence of the αIIb cytoplasmic domain, whereas the conformations of the distal helices were similar to those observed previously in a monomeric protein corresponding to the β3 TM and cytoplasmic regions (37). Further, the distal helices were amphiphilic and likely lie along the inner surface of the platelet membrane. However, their interaction with the membrane is not so stable as to impede rapid binding of cytoplasmic proteins. Thus, our results provide a framework for understanding the kinetic and thermodynamic coupling between the cytoplasmic domains of integrins and intracellular signaling molecules, interactions that act in a concerted fashion to induce cytoplasmic and TM domain separation and the exposure of extracellular binding sites for integrin ligands.

II. Results

Model αIIbβ3 cytoplasmic domain constructs.

Figure 2.1A and 2.1B shows the sequences of the αIIbβ3 TM and cytoplasmic domains. Our laboratory's previous structural studies of the αIIbβ3 cytoplasmic domain focused on the lone β3 cytoplasmic domain in the absence of αIIb (Figure 2.1C) (37). Given that integrin activation involves separation of the αIIb and β3 cytoplasmic domains, we reasoned that the structure of this construct would mimic that of the active integrin conformation. In order to understand how αIIb and β3 might interact with each other in the inactive integrin state in which TM interactions place the

11

two cytoplasmic domains in close proximity, we designed a disulfide cross-linked NMR construct (Figure 2.1D). Furthermore, to better under stand how the membrane environment might participate in the structure and dynamics of αIIbβ3, we designed two constructs for HDX analysis of the active and inactive αIIbβ3 conformations in the presence of phospholipid bilayers (Figure 2.1E and F).

A β3 Transmembrane and Cytoplasmic Domains

PKGPDILVVLLSVMGAILLIGLAALLI^{712}WKLLI^{719}TIHDRKEFAKFEEERARAKWDTANNPLYKEATSTFTNITYRGT^{762}

Transmembrane   Cytoplasmic

B αIIb Transmembrane and Cytoplasmic Domains

PIWWVLVGVLGGLLLLTILVLAM^{987}WKVGFFK^{994}-RNRPPLEEDDEEGE^{1008}

Transmembrane   Cytoplasmic

C β3 Transmembrane and Cytoplasmic Domain NMR Construct

GSA-PKGPDILVVLLSVMGAILLIGLAALLI^{712}WKLLI^{719}TIHDRKEFAKFEEERARAKWDTANNPLYKEATSTFTNITYRGT^{762}

D αIIbβ3 Cytoplasmic Domain NMR Construct

SPE-C^{987}-WKVGFFKRNRPPLEEDDEEGE^{1008}
$|$
HisTag-SPE-C^{712}-LIWKLLITIHDRKEFAKFEEERARAKWDTANNPLYKEATSTFTNITYRGT^{762}

E β3 Cytoplasmic Domain HDX Construct

GSHMG-C^{719}-TIHDRKEFAKFEEERARAKWDTANNPLYKEATSTFTNITYRGT^{762}
$|$
Maleimide-PE (C16)$_2$

F αIIbβ3 Cytoplasmic Domain HDX Constructs

GSHMG-C^{719}-TIHDRKEFAKFEEERARAKWDTANNPLYKEATSTFTNITYRGT^{762}
$|$
Ac-C^{994}-RNRPPLEEDDEEGE^{1008}

Figure 2.1 The sequences of the αIIbβ3 TM and cytoplasmic domains and experimental constructs used.

 (A) The sequence of the β3 TM and cytoplasmic domains. (B) The sequence of the αIIb TM and cytoplasmic domains. (C) The sequence of the previously reported (37) NMR construct containing the β3 TM and

cytoplasmic domains spanning from residue 691 to 762. The N-terminus contains a Gly-Ser-Ala that remains from the thrombin cleavage site. (D) The sequence of the NMR construct containing the αIIbβ3 cytoplasmic domains spanning from β3 residue 713 to 762 and αIIb residue 988 to 1008. The β3 sequence contains an N-terminal His-tag as well as a Ser-Pro-Glu helical cap. The αIIb sequence contains an N-terminal Ser-Pro-Glu helical cap. (E) The sequence of the lipid-immobilized HDX construct containing the β3 cytoplasmic domain spanning from residue 720 to 762. It contains an N-termina Gly-Ser-His-Met-Gly from the thrombin cleavage site and the NdeI restriction site. The β3 cytoplasmic domain was covalently attached to maleimide-functionalized phosphatidylethanolamine via a cysteine substitution at position 719. (F) The sequence of the bilayer-tethered αIIbβ3 HDX construct spanning β3 residues 720 to 762 and αIIb residues 995 to 1008. The αIIbβ3 heterodimer contains a disulfide cross-link between β3 residue 719 and αIIb residue 954. The N-terminus of αIIb is functionalized with a myristoyl group for membrane immobilization. *{(C) made by RHL; (D) made by DGM; (E) and (F) made by DTM}*

Our NMR construct (Figure 2.1D) contained the complete αIIb and β3 cytoplasmic domains plus a portion of their TM helices. The peptides were crosslinked by a disulfide bond between Cys residues replacing Met987 and Leu712 in the TM domains of αIIb and β3, respectively. The position for the disulfide bond was based on a model of the resting αIIbβ3 TM heterodimer (41). Recently published NMR structural studies and disulfide crosslinking experiments confirm that a disulfide bond can be accommodated at this position with little change in backbone structure (15-17). For NMR experiments, the αIIb and β3 peptides were labeled biosynthetically with ^{13}C and ^{15}N in *E. coli* and disulfide-crosslinked after activating the β3 Cys with 2,2'-dithiobis(5-nitropyridine) (42). The resulting disulfide-crosslinked construct migrated as a single species in polyacrylamide gels with an apparent molecular weight consistent with the

mass of the heterodimers. Following disulfide bond reduction, two peptides were observed that migrated with lower apparent molecular weights (Figure 2.2A).
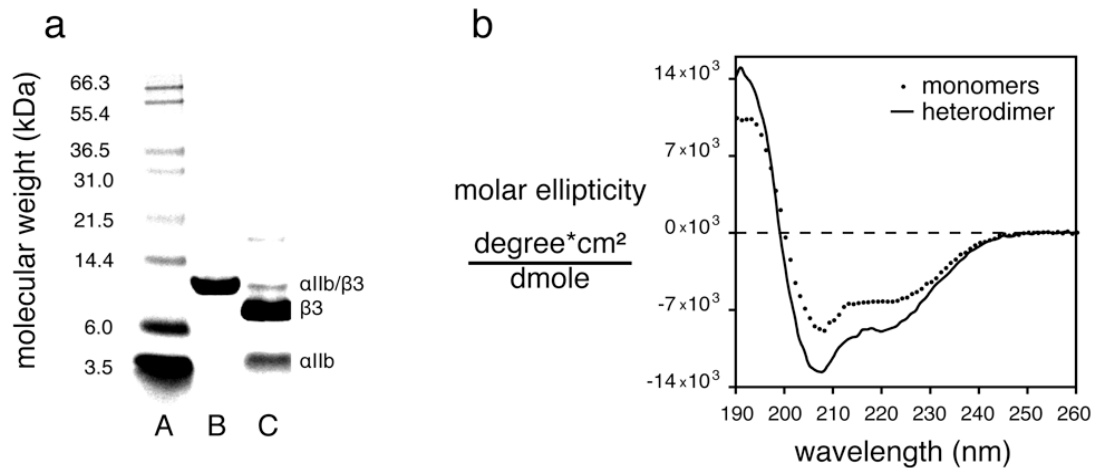
Figure 2.2 The αIIbβ3 cytoplasmic domain heterodimer construct before and after reducing its disulfide bond.

The αIIbβ3 cytoplasmic domain heterodimer construct before and after disulfide reduction. (a) Coomassie stained SDS-PAGE of the NMR construct. Lane A, molecular weight markers. Lane B, the disulfide-crosslinked construct. Lane C, the construct following disulfide bond reduction. Differences in band intensity reflect differences in the molecular weights of αIIb and β3 peptides, the β3 peptide is three times larger than αIIb per mole. (b) Circular dichroism (CD) spectra of the αIIbβ3 heterodimer before (solid line) and after reduction (dotted line). *{Performed by DGM.}*

The NMR construct was not stable in the absence of detergents and when transferred to phospholipid bilayers resulted in precipitation of the mixture. We reasoned that the NMR construct might be unstable in bilayers due to the incomplete TM domain, which would be unable to span the bilayer. Therefore two new constructs were designed for studies in the presence of phospholipids. The intention of these constructs was to mimic

14

the αIIbβ3 cytoplasmic domain as it exited the bilayer. The first construct was designed to model the active β3 cytoplasmic domain in the absence of αIIb. In a recent disulfide crosslinking study (15) that mapped the interface between αIIb and β3 TM and membrane proximal regions, residue Ile719 was found to be the first β3 cytoplasmic residue to be accessible to chemical cross-linking, suggesting that it is accessible to the cytosolic compartment and likely at the membrane/cytosol interface. Ile719 was also predicted to be at the membrane/cytosol interface when the β3 TM and membrane proximal regions were modeled using the E(z) membrane insertion potential (43). Based upon these findings, we reasoned that residue 719 would be appropriate for covalent attachment to the phospholipid headgroups. To do so, we introduced a cysteine residue, which was reacted with the surface of bilayers containing maleimide-functionalized phosphatidylethanolamine (Figure 2.1E, top). The β3 cytoplasmic domain reacted readily with the bilayers and after two hours, only the immobilized construct was observed (Figure 2.3A).

As for our NMR experiments, a disulfide cross-linked αIIbβ3 construct was designed for HDX studies in the presence of bilayers. Besides placing Ile719 at the membrane surface recent disulfide cross-linking studies (15) also found that position 719 was part of a helical interface between αIIb and β3. In that study residue 719 readily formed a disulfide bond with position 994 in αIIb. Using similar chemistry as for the NMR construct, the β3 cytoplasmic domain was attached to αIIb

15

cytoplasmic domain via a disulfide bond between residues 719 and 994 respectively. As disulfide chemistry was used to form the heterodimer, maleimide chemistry could not be used for immobilization on the membrane surface. Instead, a myristoyl group was covalently attached to the N-terminus of αIIb. The myristoylated αIIbβ3 construct was purified by HPLC (Figure 2.3B).
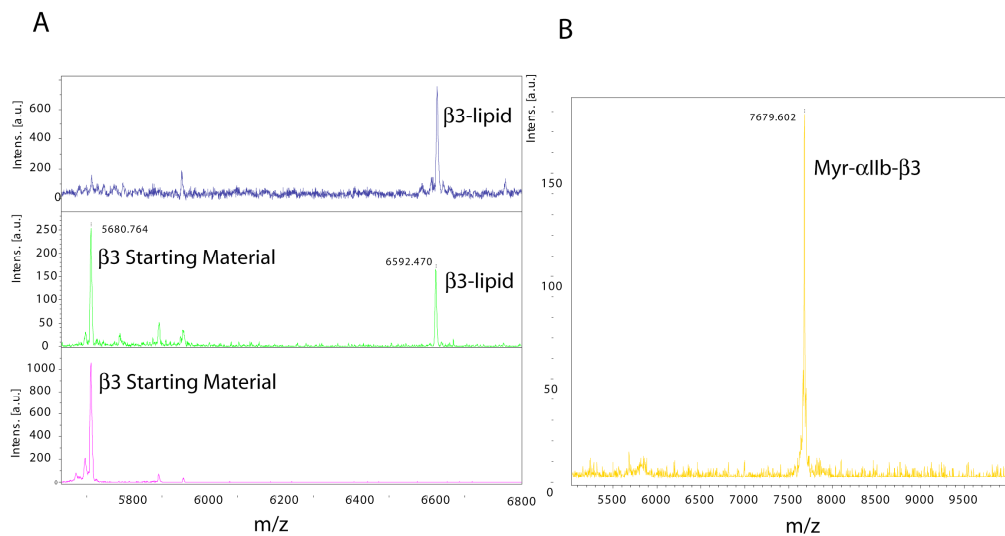
Figure 2.3 Mass spectra of membrane tethered αIIbβ3 cytoplasmic domains.

(A) The β3 cytoplasmic domain peptide (MW = 5680) containing an N-terminal cysteine residue was reacted with large unilamellar vesicles (LUVs) for 1.5 hours at pH 6.8 producing the lipid conjugated β3 cytoplasmic domain (MW = 6592). MALDI-TOF mass spectrometry was performed on the starting material (bottom, magenta), the reaction after 30 minutes (middle, green), and the reaction after 1.5 hours (top, blue). (B) Myristoylated-αIIbβ3 heterodimer was prepared as described in the methods, purified by HPLC, and subjected to MALDI-TOF mass spectrometry. *{Performed by DTM.}*

16

Association of the αIIb and β3 cytoplasmic domains influences their conformation.

Due to the inclusion of TM domain residues, the heterodimeric construct was insoluble in aqueous buffers and was studied in dodecylphosphocholine (DPC) micelles, similar to our previous analysis of the monomeric β3 TM and cytosolic regions (37). CD spectroscopy of the disulfide-linked construct contained bands at 190, 208, and 222 nm consistent with helical secondary structure (Figure 2.2B). Disulfide bond reduction resulted in a decrease in the magnitude of the molar ellipticity at 222 nm, indicating that the disulfide-linked construct was more structured than its component monomers.

The interface between αIIb and β3 was mapped by comparing ^{13}C resonances of the disulfide-linked and monomeric peptides. Like the monomeric β3 cytoplasmic domain (37), Cα resonances of the β3 cytoplasmic domain in the disulfide-linked construct were consistent with the presence of three helices: a proximal helix contiguous with the β3 TM domain (TMproxH) and two distal cytoplasmic helices (CytoH1 and CytoH2) (Figure 2.4A). No differences were observed between the distal helices of monomeric and disulfide-linked β3, but there were significant differences in the residues that define the proximal helix. The largest differences occurred at residues 720 through 724, eight to twelve residues downstream from the disulfide bond (Figure 2.4B), implying that the differences reflect αIIb and β3 interactions rather than local perturbations caused by the disulfide bond itself. Further, the chemical shifts are

17

indicative of increased helical content, consistent with the increased helical character in the CD spectrum following disulfide bond formation.

A

Cα resonance minus Cα random coil (ppm)

TM/proximal helix

helix 1

helix 2

β3 residue number

— disulfide-linked heterodimer   — β3 monomer

B

^{13}C HSQC

carbon chemical shift (ppm)

Ile719 Hβ-Cβ

Ile719 Hδ1-Cδ1

Ile719 Hγ2-Cγ2

^{13}C HSQC

Lys716 Hγ2-Cγ

Lys716 Hγ3-Cγ

Ile719 Hγ13-Cγ1

proton chemical shift (ppm)

19
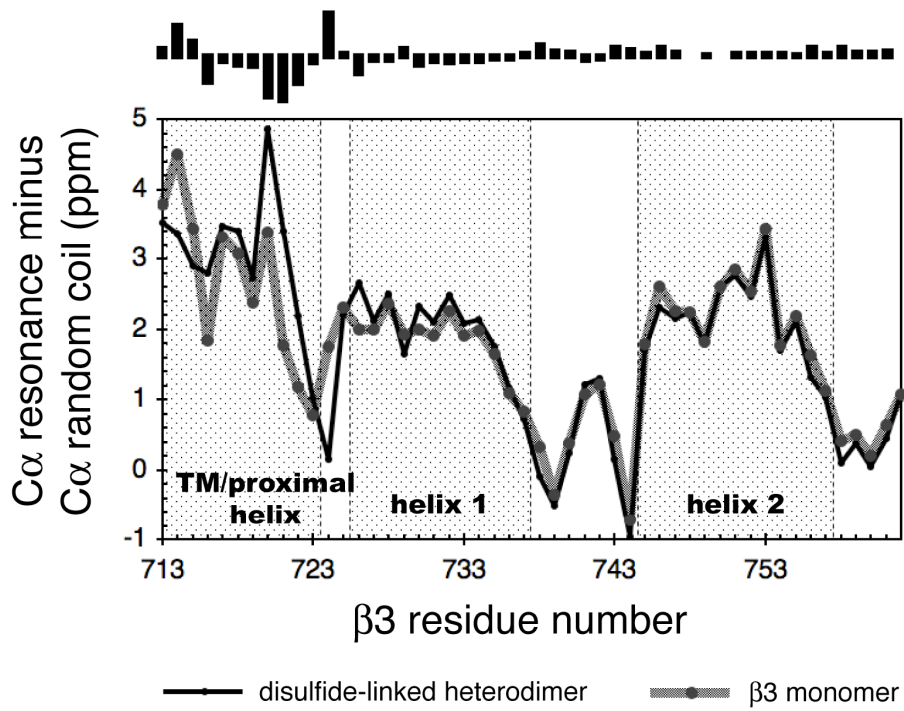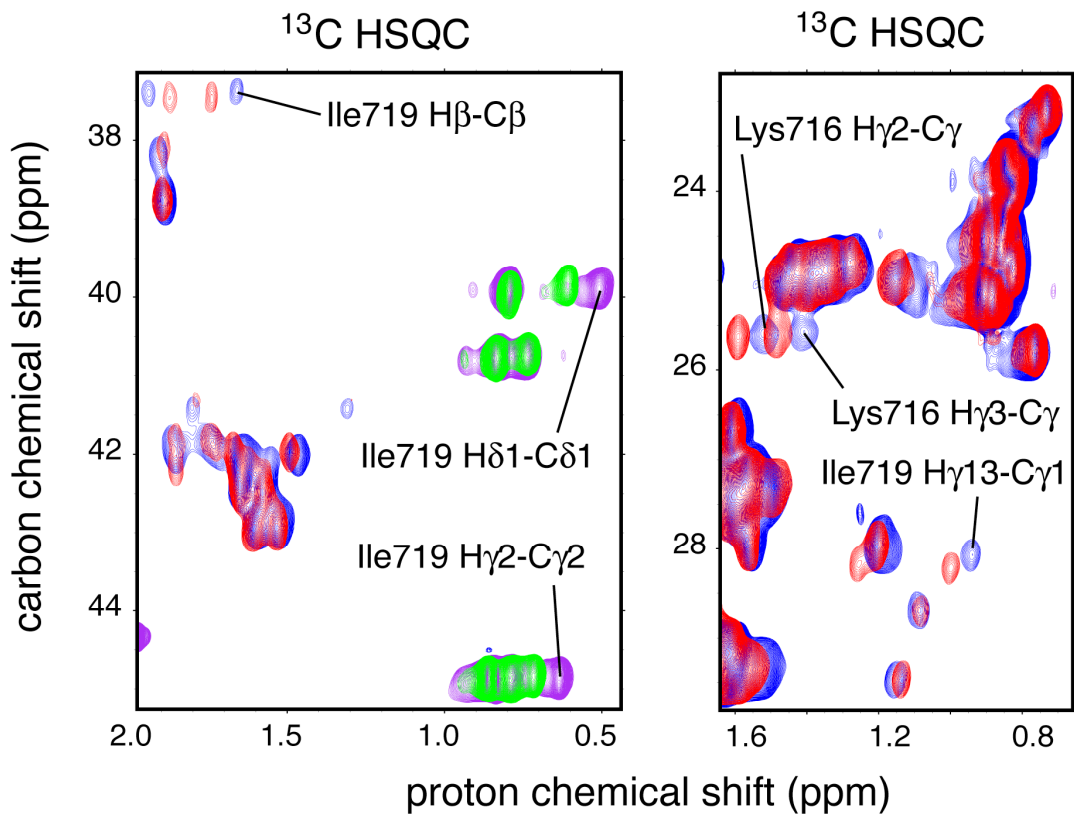
Figure 2.4 Interaction between αIIb and β3 cytoplasmic domains.

(A) Cα chemical shifts define three helical regions of β3 in the disulfide-linked heterodimer. Differences between the Cα resonances in the αIIbβ3 heterodimer and β3 monomer are shown as bars above the graph. (B) ^{13}C HSQC spectra of aliphatic atoms in the αIIbβ3 heterodimer (blue/purple) and the αIIb and β3 monomers (red and green). *{Performed by DGM.}*

The ^{13}C HSQC spectra of the disulfide-linked and reduced states were compared in order to determine the interface between the α and β chains (Figure 2.4B). The chemical shifts of the Lys716 and Ile719 side chains changed when the disulfide bond was reduced, while no differences were observed for neighboring residues, suggesting that Lys716 and Ile719 interact directly with αIIb (further supporting the choice of disulfide cross-link in Figure 2.1F). Thus, Lys716 and Ile719 define a face of TMproxH that includes Asp723, a residue postulated to form a salt bridge with αIIb Arg995 (36). Analysis of the Asp723 side chain neither confirmed nor refuted its interaction with αIIb. We did not identify NOEs between Arg995 guanidine protons and β3 sidechains. The Arg995 resonances were characteristic of a dynamic side chain and did not change substantially when the disulfide bond was reduced. Further, NMR spectra and HDX results suggest that Asp723 and Arg995 are highly solvent-exposed. Thus, any acid/base interaction would appear to be dynamic and partially screened under physiological salt conditions.

Structure of the β3 cytoplasmic domain crosslinked to the αIIb peptide

Three-dimensional structures were calculated for the αIIb and β3 cytoplasmic domains using intra- and interchain NOEs, HN-Hα J-couplings, and statistical analysis of chemical shifts (Figure 2.5A). We were unable to assign more than 5 strong NOEs between αIIb and β3, precluding calculation of a high-resolution structure. Moreover, the intra-amide ^{1}H-^{15}N HSQC peak heights for αIIb became progressively greater from its N- to its C-terminus, implying that the αIIb cytoplasmic domain is largely unstructured near its C-terminus (Figure 2.6A). Thus, we focused on defining the structure of β3 in the presence of αIIb. A structure for β3 was computed using 16 long-range, 235 medium-range, 259 short-range, and 202 intra NOE restraints, 84 dihedral angle restraints, and 24 hydrogen bonds (Table S2.1).
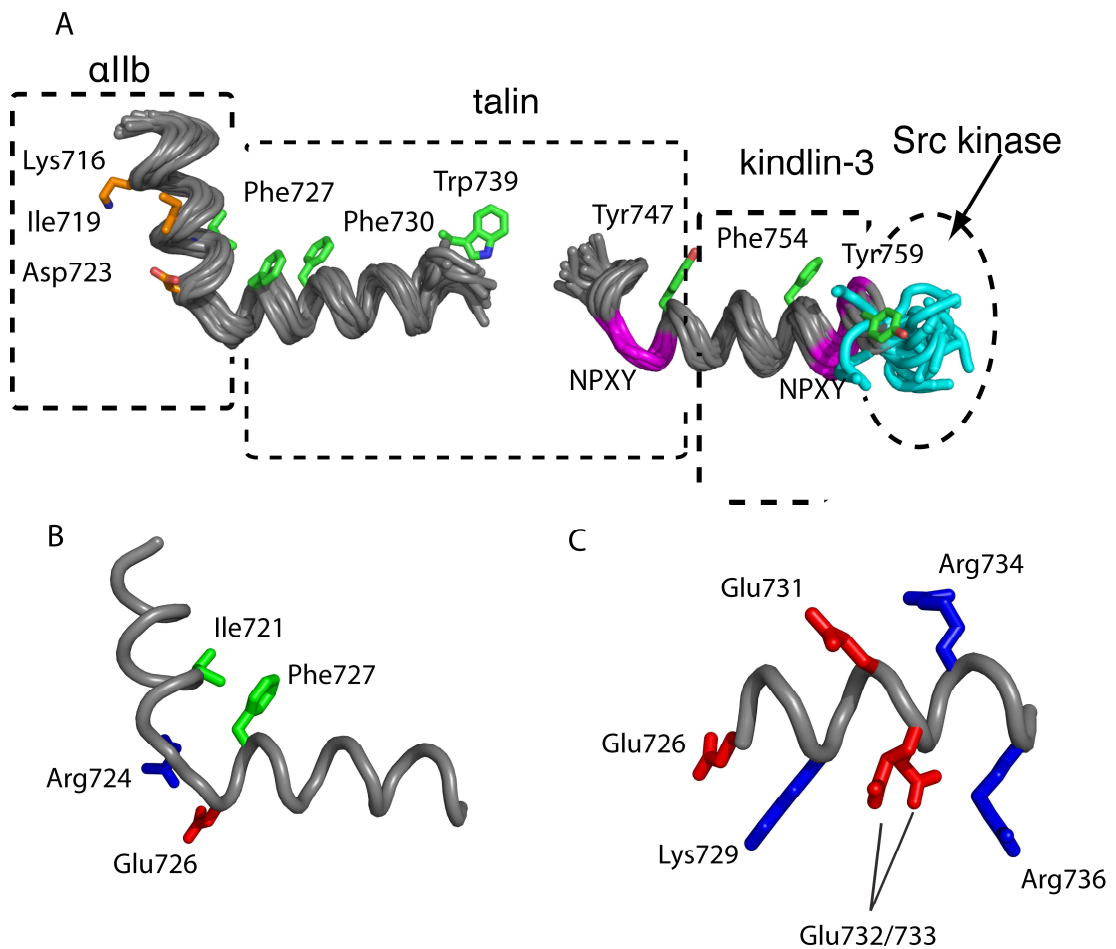
Figure 2.5 The structure of the β3 cytoplasmic domain.

(A) Twenty structures in the NMR ensemble, consisting of two regions encompassing residues Leu713-Trp739 and Asp740-Thr762, were aligned separately over well-ordered regions. Domains interacting with αIIb, talin-1, kindlin-3, and c-Src are enclosed by dashed lines and side chains that make up interfaces are depicted as sticks. The two β3 NPXY motifs are colored magenta and the Src-binding RGT motif is colored cyan. (B) A single residue hinge at Arg724 is stabilized by packing between residues Ile721 and Phe727 (green) and an electrostatic interaction between Arg724 (blue) and Glu726 (red). (C) The first cytosolic helix (residues Glu726-Arg736) is stabilized by a network of complementary charged residues. Positively charged residues are colored blue and negatively charged residues red.   *{Structure solved by DGM.}*

22

The C-terminal ends of TMproxH and CytoH1 pack together in a well-structured helix-turn-helix motif. Arg724 serves as a single-residue hinge between the two helices, having ϕ/ψ angles in the β/PPII region of the Ramachandran plot and producing a $100.5 \pm 8.8°$ angle between the two helices. A series of interactions, including strong NOEs between Phe727 and Ile721, as well as electrostatic interaction between Arg724 and Glu726, stabilize the turn (Figure 2.5B). CytoH1 itself is stabilized by a highly favorable arrangement of 12 intra-helical electrostatic interactions between residues i and $i+3/4$ (Figure 2.5C).

CytoH1 is followed by a flexible linker spanning residues 738-743. CytoH2 is then initiated by Asn744, the first residue of an NPXY motif consisting of residues Asn744-Tyr747 (44, 45). Although NPXY motifs are often found in β-turns, they are also helix initiation sites (46). Indeed, Asn744-Tyr747 adopts an identical conformation in a crystal structure of the F2F3 domains of talin-1 fused to a portion of the β3 cytoplasmic domain (pdb code 1MK7, chain A residues 744-747) (44).

Conformational flexibility of the αIIbβ3 cytoplasmic domains in micelles

The dynamics of the cross-linked αIIb and β3 cytoplasmic domains in DPC micelles were studied by measuring the intensity of intra-amide ^{1}H-^{15}N HSQC peaks (Figure 2.6A) (47, 48). αIIb residues Val990-Asn996 and β3 residues Leu713-Glu726, comprising the TM-proximal helices, displayed similar peak intensities, indicating limited mobility and stable

structures. β3 CytoH1 was somewhat more dynamic, while CytoH2 showed graded mobility, becoming increasingly less structured near its C-terminus. As noted, ^{1}H-^{15}N HSQC peak intensities for αIIb became progressively greater near its C-terminus, implying that the terminal region of the αIIb cytoplasmic domain is largely unstructured. These findings were confirmed by NMR measurements of amide proton exchange with solvent deuterons (HDX, Figure 2.6B) (49). Indeed, H-^{15}N HSQC spectra of TMproxH were highly protected from HDX, while the distal helices exchanged in a rapid time regime that was not amenable to NMR studies.
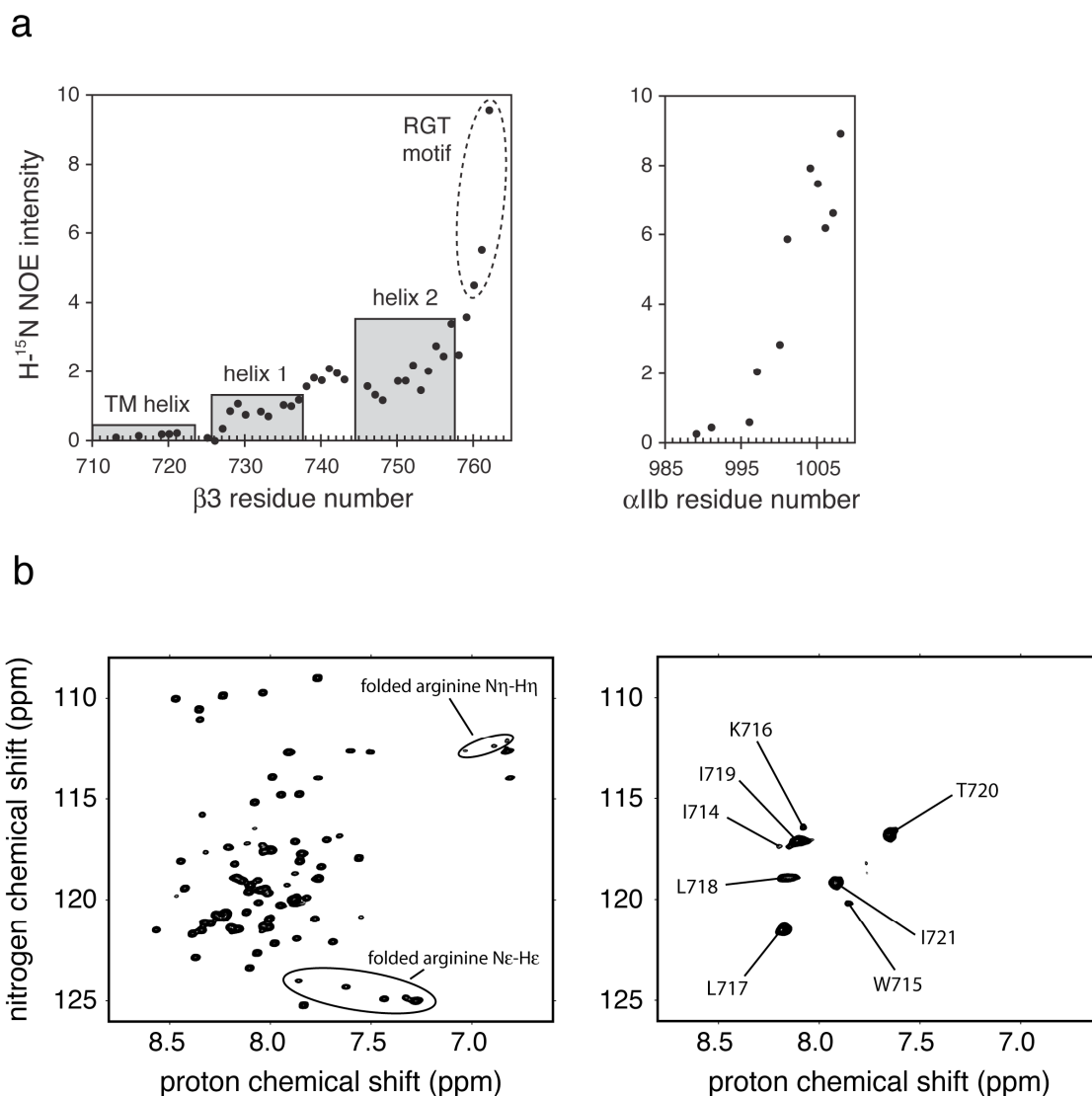
Figure 2.6 Backbone dynamics of the αIIbβ3 cytoplasmic domain heterodimer.

(A) Backbone dynamics were inferred from intra-amide ^{1}H-^{15}N HSQC peak heights and were compared with the corresponding isolated β3 construct (37). (B) ^{15}N HSQC spectrum of the disulfide-linked complex before and after HDX. The β3 backbone amides Ile714-Ile721 are protected from HDX, suggesting they form stable hydrogen bonds in a helix. Other helical regions exchange with deuterium on the minute time-scale, suggesting they make excursions from helical conformations. {*Performed by DGM*}

Conformational flexibility of the αIIbβ3 cytoplasmic domain in phospholipid bilayers.

Accordingly, we used mass spectrometry to measure HDX kinetics for the distal helices in phospholipid bilayer vesicles, a condition more closely resembling natural membranes than detergent micelles. This type of experiment has been used to determine membrane protein structure and measure unfolding rates (50, 51). We focused on the β3 segment spanning residue Thr720 to the C-terminus, because, as discussed above, this represents the portion of β3 accessible to the cytosolic compartment and the full-length NMR construct was not stable in bilayers. The cytoplasmic domain was studied in aqueous solution as well as tethered to preformed large unilamellar vesicles (LUVs). As with our NMR studies, β3 was probed in the presence and absence of αIIb in order to determine the effects of αIIb on its structure.

CD spectroscopy revealed that when the β3 cytoplasmic domain was covalently tethered to bilayers, the peptide's α-helical content increased and the random coil signature decreased (Figure 2.7), indicating that the β3 cytoplasmic domain interacts with phospholipid bilayers. To measure HDX, free and tethered β3 peptides were incubated in D_2O buffer for varying periods of time, after which amide deuterium exchange was quenched at pH 2.5. The quenched peptides were injected onto an immobilized pepsin column to generate fragments that were analyzed by tandem LC/MS. Free β3 peptide exchanged rapidly with D_2O (Figure 2.8, red), indicating that its conformation was largely disordered, consistent

26

with CD results (Figure 2.7). When the $\beta3$ peptide was membrane-bound, the most membrane proximal region, Thr720-Glu732, remained tethered to the lipid after proteolysis and was not observed. However, we observed two fragments that contained portions of CytoH1 and CytoH2. Both fragments had two kinetically distinct classes of amides: one class had unprotected amides that exchanged at a rate indicative of an unstructured backbone; the second class exchanged with a protection factor on the order of 10^2 to 10^3, indicative of a helix making occasional excursions to less well-structured conformations that allow HDX. The fragment containing the C-terminus of CytoH1, the flexible loop, and the N-terminus of CytoH2 (Glu733-Thr753) had approximately 8 protected amides (Figure 2.8A, green). The second fragment contained the C-terminus of CytoH2 (Asn756-Thr762) and had only one protected amide (Figure 2.8B, green). These results confirmed the location of CytoH1, which was identified by NMR, as well as the hierarchy of increasing disorder that progresses from the N- to the C-terminus of the $\beta3$ cytoplasmic domain.
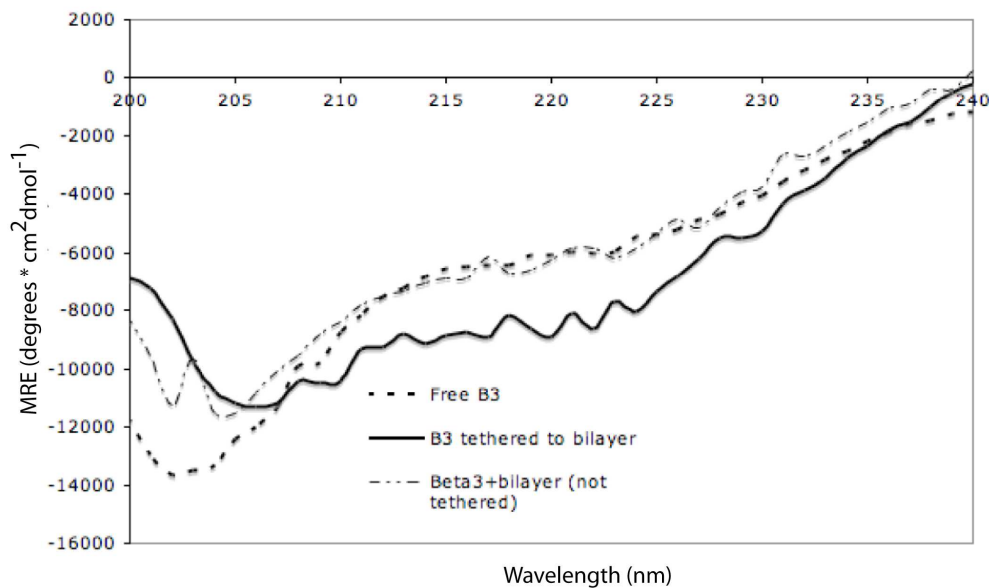
Figure 2.7 Circular dichroism confirms that interactions with phospholipids stabilizes a helical conformation.

CD spectra were taken of free β3 in the absence of lipid (black dots), membrane- tethered β3 (solid line), and β3 mixed with lipids, but not reacted with the maleimide head group (grey dots and lines). CD spectra of β3 alone were taken of 30 μM β3 in 25 mM phosphate 100 mM NaCl, pH 6.8. For lipid conjugated β3, 15 μM β3 was conjugated to 1 mM total lipid containing 20% POPG, 12% maleimide-PE, and 68% POPC in 25 mM phosphate with 100 mM NaCl, pH 6.8. Unconjugated β3 in the presence of lipid contained 15 μM β3 and 1mM total lipid containing 20% POPG and 80% POPC*. {Spectra are representative of three independent experiments. Performed by DTM]*

Our NMR results suggest that when αIIb is held in close proximity to β3 – as would be expected in the inactive αIIbβ3 conformation – a kink is stabilized in β3. We hypothesized that such a kink would project distal β3 cytoplasmic elements such as CytoH1 and CytoH2 parallel to the membrane and encourage their interactions with the bilayer beyond the interactions observed with lipid-immobilized β3. We therefore sought to

28

determine by HDX whether this kink in the presence of bilayers might stabilize distal structures observed by NMR. As described above, we synthesized and purified a disulfide cross-linked αIIbβ3 construct with an N-terminal myristoyl membrane anchor. This peptide was not water soluble, but was readily solubilized when extruded with phospholipid bilayers. When HDX experiments were performed on this αIIbβ3 construct, similar pepsin cleavage products were observed. Again, the N-terminus was not seen, because of its covalent attachment to αIIb, but peptides containing residues Glu733-Thr753 and the Asn756-Thr762 were observed. Like β3 in the absence of αIIb (Figure 2.8A, green), the peptide spanning Glu733-Thr753 was found to have approximately 8 protected amides in the presence of bilayers (Figure 2.8A, blue). The protection pattern for the most distal fragment was quite different, though. The peptide containing Asn756-Thr762 was found to be significantly protected from exchange. In the presence of bilayers, the heterodimeric αIIbβ3 cytoplasmic domain had 3-4 amides with protection factors on the order of 10^2-10^3 (Figure 2.8B, blue). These results support the NMR-based model that the presence of αIIb stabilizes the interaction between β3 and the membrane. It is possible that the protection of the distal β3 segment from HDX could arise from direct interactions with αIIb and as opposed to a helical interaction with the membrane, however, NOEs between αIIb and the β3 segment were not observed in the NMR.
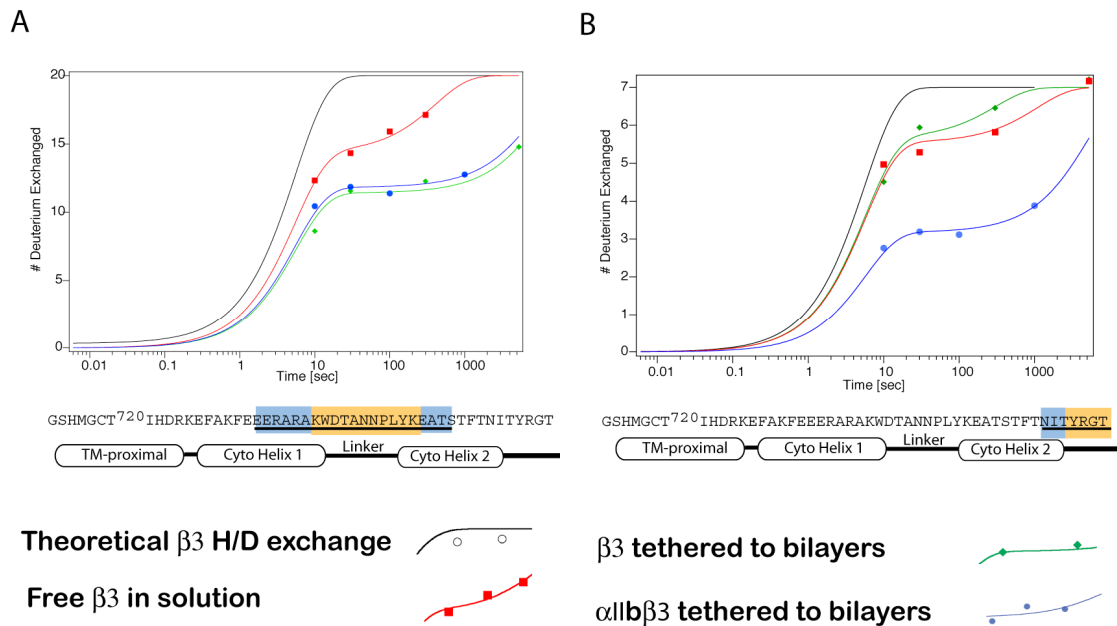
Figure 2.8 HDX-MS of the αIIbβ3 cytoplasmic domain in phospholipid bilayers.

Model αIIbβ3 cytoplasmic domain constructs were prepared in pH 6.8 phosphate with 100 mM NaCl. Each sample was diluted 1:10 in pH 6.8 phosphate with 100 mM NaCl containing 90% D_2O on ice. Deuteration was quenched at pH 2.5 on ice and samples were injected onto a pepsin column in tandem with LC-MS to resolve fragments and calculate deuteration. The deuteration reaction for each sample was fit to a double exponential rate equation assuming subpopulations of rapidly and slowly exchanging amides. Peptide fragments containing (A) Glu733-Thr753 and (B) Asn756-Thr762 were observed. For each peptide a theoretical curve based upon the predicted intrinsic exchange rate for a disordered peptide was generated (black). HDX was performed on free β3 cytoplasmic domain (red), the β3 cytoplasmic domain covalently immobilized on phospholipid bilayers containing 20% POPG, 12% maleimide-PE, and 68% POPC (green) which is predicted to model the active β3 state, and disulfide cross-linked αIIbβ3 in phospholipid bilayers containing 20% POPG and 80% POPC (blue) which is predicted to model the inactive state. Residues highlighted in blue are predicted to be protected from exchange based upon the NMR structure. Residues highlighted in orange correspond to regions found to be disorganized in the NMR structure or at the N-termini of helices and not predicted to be protected from exchange. *{Experiments performed once by DTM}*

The increased helicity of the β3 cytoplasmic domain (Figure 2.7) in the presence of bilayers and its protection from HDX under these conditions suggest that it interacts with the membrane surface. We used E(z), a depth-dependent potential (43), to assess the binding of the β3 helices in membranes. As expected, TMproxH was predicted to partition into the bilayer perpendicular to the membrane as an extension of the TM helix, whereas CytoH1 and CytoH2 were predicted to lie along the membrane surface, stabilized by hydrophobic residues Phe727 and Phe730 in CytoH1 and Leu746, Tyr747, Ala750, Phe754, and Ile757 in CytoH2 (Figure 2.9A).

III. Discussion

We have studied the structure and dynamics of the platelet integrin αIIbβ3 cytoplasmic domain. We found the αIIb cytoplasmic domain intrinsically disordered, consistent with its paucity of hydrophobic residues and a recent NMR study using phospholipids bicelles (52). Nonetheless, chemical shift perturbations indicate that αIIb interacts with the TM proximal portion of β3 over the length of 12 residues, implying that αIIb has a conformational bias toward structures that interact with β3. This type of intrinsically disordered interaction has been found in proteins that couple multiple signaling events to an overall equilibrium (53). In the case of αIIbβ3, an intrinsically disordered interface would allow the integrin to

rapidly shift between resting and active conformations following a breach in vascular integrity.

The N-terminal portion of the β3 cytoplasmic domain consists of a highly stable helix contiguous with the C-terminal end of the TM helix and separated from a second surface-associated helix by a single-residue hinge at Arg724. The remainder of the cytoplasmic domain consists of a short unstructured region, a second cytoplasmic helix and a flexible C-terminal tail. CytoH1 and CytoH2 are likely stabilized by interactions with the membrane bilayer (Figure 2.9A), although they are not so stable as to lock the cytoplasmic domain into a single fixed conformation. Instead, CytoH1 and CytoH2 undergo frequent excursions into non-helical conformations within the aqueous environment. The association of CytoH1 and CytoH2 with membranes is consistent with previous NMR experiments observing NOEs between micellar DPC and Trp739/Tyr747 (54). Amphiphilic domains proximal to TM domains have also been detected in proteins such as voltage gated channels (55, 56), phospholamban (57), and the influenza M2 proton channel (58, 59). The association of cytoplasmic helices with membranes can change in response to gating ligands or post-translational modification. For example, the cytoplasmic helix of the pH-activated M2 channel changes its orientation in response to pH. Also, aromatic residues in the cytoplasmic domain of the T-cell receptor CD3ε subunit were found to insert into membranes, including a tyrosine in its NPXY motif (60). Following T-cell

32

receptor activation, the amphiphilic domain is released from the membrane.

a

b

Available to Kindlin

c

Kindlin

Kindlin

Activated-signaling integrin

Talin   Kindlin

Talin   Kindlin

Talin

Talin
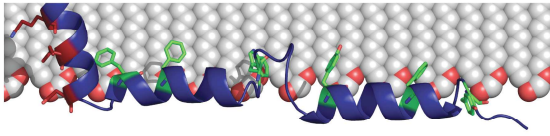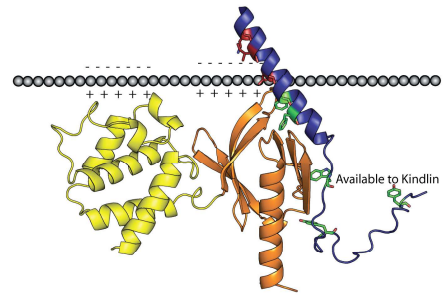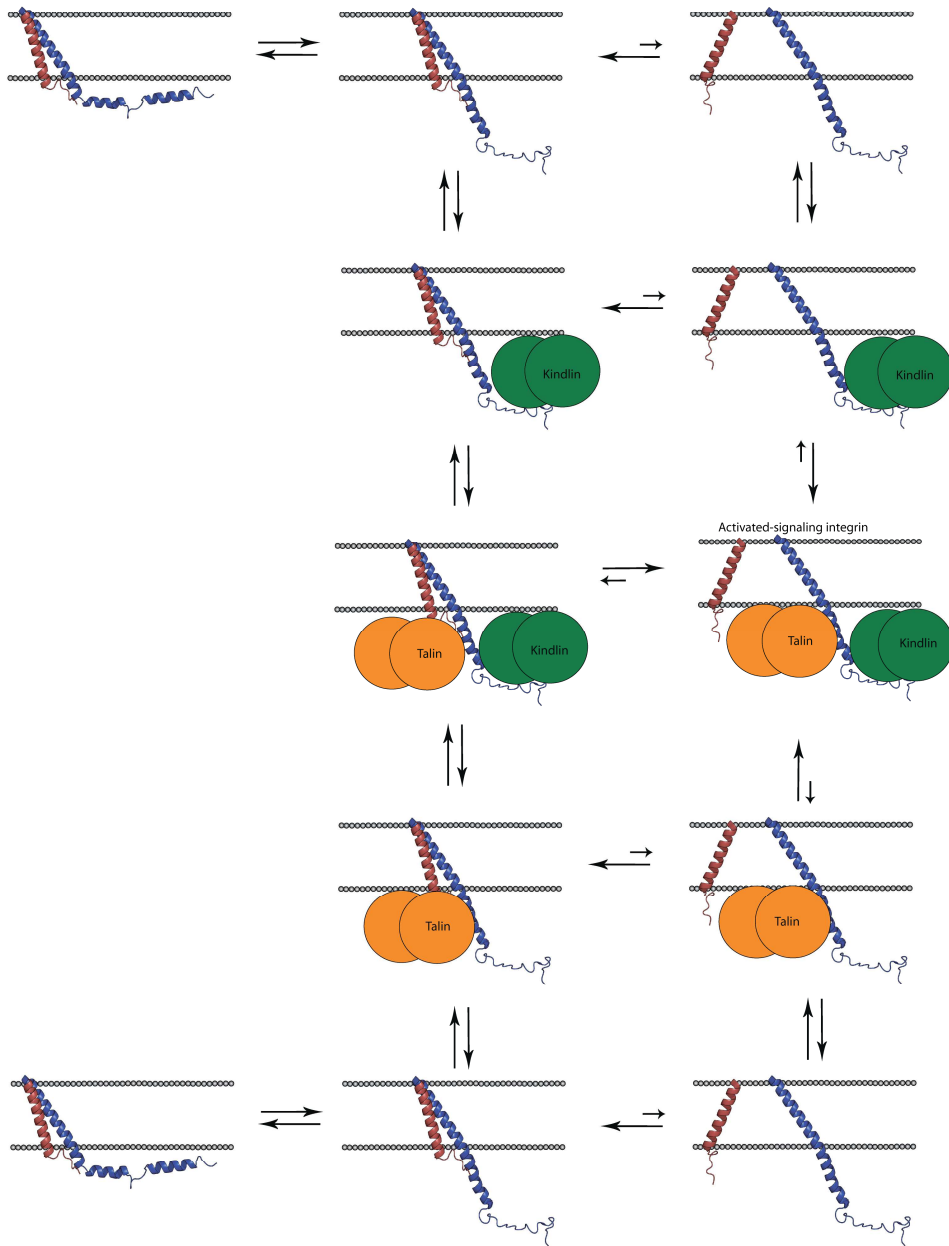
Figure 2.9 A linked equilibrium describing the activation of αIIbβ3 by intracellular signaling molecules.

(A) The E(z) membrane insertion potential was used to model the interaction of β3 with the membrane. It predicts that aromatic residues (green) on one face of CytoH1 and CytoH2 will preferentially bind the membrane. (B) The dynamic nature of the β3 cytoplasmic domain makes protein-protein interaction motifs accessible. Dissociation of αIIb and extension of the β3 TM-proximal helix to join CytoH1 allows talin-1 to bind and places positively-charged residues on talin-1's upper surface in a favorable position to interact electrostatically with the inner membrane leaflet. β3 is also now available to bind kindlin. Residues that are perturbed by the αIIb cytoplasmic domain are shown in red. (C) An equilibrium model of talin-1 and kindlin-3 binding the integrin cytoplasmic domain. To the left is a resting conformation with helices CytoH1 and CytoH2 interacting with the bilayer. The fully inactive state is not competent to bind talin-1 or kindlin-3 because the membrane obstructs access to β3. To the right is a fully active conformation with separated TM and cytoplasmic domains. In between exists an ensemble of states in which the integrin is not active, but the β3 cytoplasmic domain samples a wide range of conformations and is accessible to intracellular molecules. Although talin-1 and kindlin-3 can bind the ensemble of free cytoplasmic domains in the middle column, available data are insufficient to predict the order of binding. Therefore, equilibria depicting talin-1 binding first (top) and kindlin-3 binding first (bottom) are shown. However the fact that both kindlin-3 and talin-1 are necessary for activation suggests that both bind to the integrin cytoplasmic domain.

The marginally stable interactions between the membrane bilayer and the β3 cytoplasmic helices are likely important for allowing kinetic access to cytoplasmic proteins, such as talin-1 and kindlin-3, responsible for triggering αIIbβ3 activation (19). The structure of β3 elucidated here presumably represents the resting state which must undergo structural changes to allow binding of these proteins. The talin-1 binding site, extending from the C-terminus of the TM helix through CytoH1 to the NPxY motif near the N-terminus of CytoH2, is masked in the NMR structure by interactions with the αIIb tail and the phospholipid bilayer.

Interaction with membranes is facilitated by the bend between TMproxH and CytoH1 at Arg724; if this residue instead continues the TMproxH α-helix (Figure 2.9B), CytoH1 becomes an extension of the TM helix, allowing binding of the talin-1 head domain (61, 62). This orientation not only allows interaction of the talin-1 F3 domain with the β3 tail, but also electrostatic interactions between acidic lipids on the cytoplasmic leaflet of the bilayer and positively charged residues in talin-1's F2 and F3 domains. Moreover, the interaction of the β3 tail with talin-1 removes the C-terminal region of β3 from the membrane and positions its kindlin-binding site for simultaneous interaction with kindlin-3. Such a tandem interaction has recently been demonstrated for dimerization of the PTB domain of the cytoplasmic adaptor protein Dok7 (63). Displacement of this segment from the membrane also destabilizes the C-terminal β3 helix, allowing it to more easily conform to the requirements for kindlin-3 binding.

The interactions of talin-1 and kindlin-3 with β3 show the hallmarks of a cooperative system; association of either protein with its β3 binding site occurs at the thermodynamic expense of disrupting favorable β3-membrane binding interactions. Moreover, binding of one protein primes the system for a more favorable interaction with the second. Thus, the sites are both kinetically and thermodynamically linked, as shown in Figure 2.9C. The talin-1 binding event is likely the key step in tail separation, given the proximity of the talin-1 interacting site to the αIIbβ3 interface. Thus, at sufficiently high talin-1 concentrations, it should be

possible to activate αIIbβ3, even in the absence of kindlin-3 (64). However, under physiologic conditions, our model predicts that kindlin-3 also plays a pivotal role for interaction of talin-1 with the β3 tail. At present, it is unclear whether there is a preferred temporal sequence for binding of kindlin-3 versus talin-1 during physiological αIIbβ3 activation. However, the greater mobility of the kindlin-3 binding site in the β3 cytoplasmic domain suggests it might have a kinetic advantage over talin-1, assuming both are present in appropriate forms for binding. Figure 2.9C (top and bottom) illustrates both kinetic possibilities for the initial binding step. Once initial binding occurs, subsequent interactions and conformational changes become increasingly favorable, ultimately tipping the equilibrium towards tail separation and αIIbβ3 activation (Figure 2.9C, middle panel). This thermodynamic coupling model could be extended to any number of cytoplasmic events playing negative or positive roles in activation. We predict that direct interactions of the β3 cytoplasmic domain with αIIb and the phospholipid bilayer help restrain αIIbβ3 in a resting state. Any protein that binds more tightly to the separated cytoplasmic domains than the cytoplasmic domain heterodimer will have an activating effect. Furthermore, proteins that negatively impact talin-1 binding will have an inhibitory effect on αIIbβ3 activation.

IV. Methods

Plasmid Constructs—A cDNA encoding αIIb residues Trp988-Glu1008 was cloned into the vector pET-16b (Novagen) as a C-terminal

fusion with the designed protein α_3D (65). The region between the αIIb sequence and α_3D included a proline to disrupt secondary structure, two glycines as a flexible spacer, a thrombin cleavage site, an SPE N-terminal helix cap, and a cysteine for crosslinking to the β3 peptide. The αIIb peptide sequence was: α_3D-P-GG-LVPR-SPE-C-WKVGFFKRNRPPLEEDDEEGE. A cDNA encoding β3 residues Leu713-Thr761 was cloned into the vector pET-15b (Novagen) downstream from a polyhistidine tag. The construct included an SPE N-terminal helix cap followed by a cysteine for crosslinking. The β3 peptide sequence was:

MGSSHHHHHHSSGLVPRGSHM-SPE-C-

LIWKLLITIHDRKEFAKFEEERARAKWDTANNPLYKEATSTFTNITYRGT.

The fidelity of the constructs was confirmed by DNA sequencing.

A shortened β3 cytoplasmic domain (MGSSHHHHHHSSGLVPRGS-|-H MG-C-TIHDRKEFAKFEEERARAKWDTANNPLYKEATSTFTNITYRGT) was cloned into the pet-28a vector. It contained a cysteine for reaction with phospholipid bilayers or αIIb.

Protein Expression and Purification—The α_3D-αIIb fusion protein and the His-tagged β3 protein were expressed in *E. coli* strain BL21 and labeled biosynthetically with ^{13}C glucose and/or ^{15}N ammonium chloride (Cambridge Isotope Laboratories). The α3D-αIIb fusion protein was isolated from the supernatant of bacterial lysates, cleaved with thrombin, and purified by reverse-phase HPLC. The His-tagged β3 protein was

isolated on Ni-NTA resin using the QIAExpressionist protocol for denaturing conditions (Qiagen) and purified by reverse-phase HPLC. These protocols generated >10 mg of the αIIb and β3 proteins per liter culture. The molecular weight of each product was confirmed by mass spectroscopy.

The His-β3 construct used for HDX was expressed in BL21-DE3 *E. coli* and purified using Ni-NTA chromatography on an Akta FPLC (General Electric Healthcare). Purified His-β3 was dialyzed into 50mM Tris, 100 mM NaCl, pH 7.5 and cleaved with thrombin overnight at room temperature. The resulting peptide (GSHMG-C-TIHDRKEFAKFEEERARAKWDTANNPLYKEATSTFTNITYRGT) was purified by reverse phase HPLC on a C4 preparative column (Vydac) on a water/acetonitile/^{i}PrOH gradient in 0.1% TFA.

SDS-PAGE of αIIbβ3 NMR construct-The disulfide cross-linked heterodimer was dissolved in LDS loading buffer and run on a NUPAGE SDS-PAGE gel. Excess TCEP was added to an identical sample and run in an adjacent lane. The gel was washed and stained with Coomassie GelCode stain (Pierce).

Synthesis of the myristoylated αIIb cytoplasmic domain–αIIb-CT was synthesized on Wang resin preloaded with an Asp residue using a Symphony peptide synthesizer at 0.1 mM scale in 25% DMSO/75% NMP

39

with Fmoc-chemistry. αIIb-CT was myristoylated on resin by reacting the protected peptide with 5-fold excess HBTU activated myristic acid (Sigma) for three hours at room temperature. αIIb-CT was cleaved from the resin TFA/triethylsilane/water (95/2.5/2.5 v/v) for three hours and precipitated into dry-ice cold diethylether. β3-NITYRGT was purified by reverse phase HPLC (Varian Prostar) using a C4 preparative column (Vydac) on a water/acetonitrile/^{i}PrOH gradient with 0.1% TFA.

Formation of a disulfide-linked αIIbβ3 cytoplasmic domain heterodimer for NMR—The β3 peptide was dissolved at 5 mg/ml in 50 mM MES buffer, pH 6.0, containing 2M guanidine, after which its cysteine thiol was activated with a 5-fold molar excess of 2-2'dithio-bis-(5-nitropyridine) dissolved in DMSO (42). After excess 2-2'dithio-bis-(5-nitropyridine) was removed on a PD-10 column (GE Healthcare), the activated β3 was reacted with a slight molar excess of the αIIb protein in guanidine-MES buffer, pH 6.5. Disulfide-linked αIIbβ3 was purified using reverse phase HPLC in a gradient with 60% iPrOH, 30% ACN, 10% H_2O with 0.1% TFA. Its molecular weight confirmed by mass spectrometry.

Preparation of a disulfide-linked membrane-tethered αIIbβ3 cytoplasmic domain heterodimer for HDX. The β3 cytoplasmic domain was prepared as described earlier. To form the myristoylated αIIbβ3 heterodimer, the β3 cytoplasmic domain was reacted with 2-2'dithio-bis-(5-nitropyridine) in 50% acetic acid to produce activated 2-thio-(5-

nitropyridine) adduct, which was transferred to pH 5 sodium acetate buffer and separated from unreacted 2-2'dithio-bis-(5-nitropyridine) by passage over a PD-10 buffer exchange column (GE Healthcare). The activated β3 was diluted nine fold with acetonitrile and reacted with a slight excess of Myr-αIIb. It was crucial to perform this reaction in an organic solvent, as Myr-αIIb homodimers were the primary product in aqueous buffers, likely due to formation of micelles or aggregates due to the myristic functional group that produced a high local concentration of Myr-αIIb thiol that displaced β3 from the αIIbβ3 heterodimer. The reaction was diluted with pH 2 water and immediately frozen and lyophilized for purification by reverse phase HPLC on a gradient with 60% iPrOH, 30% ACN, 10% H_2O with 0.1% TFA.

Preparation of membrane tethered β3. Lyophilized Cys-β3 construct was lyophilized and re-dissolved in bilayer conjugation buffer (25mM sodium phosphate or MOPS, 100 mM NaCl, pH 6.8). Large unilamelar vesicles (LUVs) were generated by evaporating a mixture of 20% 1-palmitoyl-2-oleoyl-*sn*-glycero-3-phospho-(1'-*rac*-glycerol) (POPG, Avanti Polar Lipids), 4 fold molar excess of 1,2-dipalmitoyl-*sn*-glycero-3-phosphoethanolamine-N-[4-(p-maleimidomethyl)cyclohexane-carboxamide] (16:0 PE MCC, Avanti Polar Lipids) relative to β3 peptide, and 1-palmitoyl-2-oleoyl-*sn*-glycero-3-phosphocholine (POPC, Avanti Polar Lipids) to a thin film under nitrogen and re-suspending the dried lipids in the bilayer conjugation buffer. LUVs were prepared by extruding

41

20 times through a 0.1 μm filter (Avanti Polar Lipids). β3 peptide was reacted with 4 fold molar excess 16:0 10 PE MCC. The conjugation reaction was performed at pH 6.8 to minimize lysine amine-maleimide side reaction which is strongly disfavored at below pH 7.

NMR Spectroscopy—Purified, disulfide-linked αIIbβ3 heterodimer was dissolved at 1 mM in 5 mM sodium phosphate buffer, pH 6.0, containing 100 mM perdeuterated DPC (Cambridge Isotope Laboratories), 10% deuterium oxide, and 0.02% sodium azide. Samples were analyzed at 37ºC on a 750 MHz NMR spectrophotometer equipped with a Varian probe (66).

CD spectroscopy for the NMR sample—CD spectra of 10 μM disulfide-linked αIIbβ3 heterodimer in 5 mM sodium phosphate buffer, pH 6.5, containing 10mM dodecylphosphocholine (DPC) were collected on a JASCO J-810 spectropolarimeter with a path length of 1 mm before and after the addition of a 5-fold molar excess of the reducing agent tris(2-carboxyethyl) phosphine hydrochloride (Sigma-Aldrich). Measurements were made stepwise for each 1 nm between 190 nm to 260 nm and averaged over ten scans.

Assignment of chemical shifts—The backbone, aliphatic, and aromatic resonances in the αIIb and β3 subunits were assigned using a standard battery of experiments.(66) Complete residue-specific assignments for the Hα, N, Cα, and Cβ resonances in β3 were obtained using the HNCACB(67) and CBCA(CO)NH(68) experiments. Carbonyl

42

carbons were assigned from HNCO experiments.(69) Aliphatic protons and carbons were identified using H(CCCO)NH,(70, 71) (H)CC(CO)NH,(70, 72, 73) and H(C)CH-TOCSY(74-77) experiments. Pro-chiral leucine and valine methyls were distinguished in the ^{13}C-coupled carbon HSQC of a metabolically labeled sample expressed in media containing 10% ^{13}C glucose.(78) Aromatic resonances were assigned using HBCBCGCDHD and HBCBCGCDCEHE experiments,(79) an aromatic carbon HSQC, an aromatic ^{13}C-edited NOESY, and other NOESY experiments. Assignments for αIIb residues 988-1000 were completed using the same strategy. Additionally, resonances in the αIIb acidic tail E_{1001}EDDEEGE$_{1008}$ were identified, but were not useful for structural analysis due to spectral overlap. Proton chemical shifts were referenced to residual water signal, while ^{13}C and ^{15}N chemical shifts were indirectly referenced. Chemical shifts were deposited in the BioMagResBank (80).

Identification of NOEs—Nuclear Overhauser Effect restraints (NOEs) were obtained from an ^{15}N-editied NOESY, an aliphatic ^{13}C-edited NOESY, an aromatic ^{13}C-edited NOESY, and a 4D ^{13}C-edited NOESY.(81, 82) Mixing times were optimized for different NOESYs and ranged from 80 ms in the ^{13}C-edited NOESYs to 100 ms in the ^{15}N-editied NOESY. The solvent contained 99% D_2O in the 4D NOESY.

HN-Hα J-coupling—Phi dihedral angle restraints were obtained from HN-Hα J-couplings measured in the HNHA experiment.(81) Phi

angles were calculated using the Karplus equation with coefficients A = 6.51, B = -1.76, and C = 1.60. $\beta3$ residues Lys716-Thr720, Phe727-Arg736, and Leu746-Asn756 were given helical phi restraints based on chemical shift analyses, NOE patterns, and HDX experiments that suggest they reside in helices. Other residues were given J-coupling restraints that restrict the phi dihedral to 1-4 possible angles.

Hydrogen-deuterium exchange (HDX)— HDX was performed by lyophilizing a NMR sample and re-dissolving it in deuterium oxide. Exchange was monitored in the HSQC experiment and the first time-point was taken at 11 minutes.

Residual dipolar couplings (RDCs)— RDCs were obtained for samples aligned in axially stretched polyacrylamide gels. A dried, 6mm diameter, 5.5% polyacrylamide gel was soaked with an NMR sample for 72 hours, then funneled into a 4.2mm diameter NMR tube.(83) Cα-C' RDCs were obtained using a Cα-coupled HNCO experiment.(69)

Implementation of distance restraints—Distance restraints were derived from NOE experiments and HDX. NOESY cross-peak volumes were converted to upper distance limits by the program CALIBA of the CYANA package (84). NOE peaks were divided into three classes with different calibration functions and constants: a $1/r^6$ dependence was used for backbone-proton-backbone-proton NOE values, and a $1/r^4$ dependence for NOEs involving side-chain protons and methyl groups. The upper and lower cutoffs for NOEs before application of pseudoatom

corrections were set as 2.4 and 6.0 Å for strong and weak NOEs, respectively. During the structure calculation and NOE assignment, the calibration curves were refined iteratively based on plots of cross-peak volumes versus average proton-proton distances in the current structures. For each distance constraint, the lower limit was set as 1.8 Å, which corresponds to two hydrogen van der Waals radii. Additionally, 24 hydrogen bonds were used for the regular secondary elements Glu711-Asp723, Glu726-Ala736, and Pro745-Ile758. 5 hydrogen bond restraints, which were also confirmed from HDX, were implemented by setting the N to i+4 O distance to 3.0 Å with 10% error, while the remaining hydrogen bond restraints were held with 20% error.

Implementation of angle restraints—Dihedral angle restraints were derived from TALOS+(85) (86) and J-coupling experiments.(81) The TALOS algorithm predicts backbone phi and psi angles based on protein sequence and assigned resonances from a database of known structures. TALOS-derived phi and psi dihedral restraints were used for β3 residues Cys712 - Thr758, except for residues Arg724, Lys738 and Trp739, which were predicted to be helical with high confidence, consistent with NOE patterns, HDX, and J-coupling. Additionally, phi dihedral angle restraints were obtained from HN-Hα J-couplings. β3 residues Leu713-Asp723, Glu726-Arg736, and Pro745-Thr758 were given helical phi and psi angle restraints based on chemical shift analysis, NOE patterns, and HDX experiments which suggest they reside in helices. Other residues were

given J-coupling restraints that restrict the phi dihedral to 1-4 possible angles.(81)

Implementation of RDC restraints—RDCs were measured and evaluated. Nonetheless, the dynamics of the αIIbβ3 construct prevented fruitful refinement of the structural ensemble using RDCs.

Structure Calculation—Data were processed with FELIX, analyzed with Sparky and Xeasy (87) , and structures were calculated using CYANA (84) and finally refined by XPLOR-NIH.(88) Structure calculations and refinement algorithms were based on the anneal.py and refine.py example scripts that come with the XPLOR-NIH package. Structures were calculated for the β3 portion of the disulfide linked αIIb/β3 construct consisting of the SPE N-terminal helix cap, the cysteine used to form the disulfide crosslink, and β3 residues 713-762:

SPE-C-

LIWKLLITIHDRKEFAKFEEERARAKWDTANNPLYKEATSTFTNITYRGT

where the italicized residues were engineered and the rest of the construct corresponds to the β3 cytosolic domain. Each algorithm included an initial, high temperature simulated annealing cycle followed by a longer simulated annealing cycle with both cycles restricted to torsional movements. After the simulated annealing cycles, the output conformation was minimized in both torsional and Cartesian space. The energy function included a repulsive van der Waals term and potentials that enforced bond lengths, bond angles, and improper angles.

Additionally, the refinement algorithm included a potential that enforced backbone geometries that are consistent with Ramachandran space. Other potentials enforced NMR restraints as described below.

No violations >0.5 Å per conformer were observed. The statistics of the structure determination are summarized in Table S2.1 and show that a high-resolution and high-quality structure was obtained. The final structure was deposited in the PDB(89) (accession code: 2KV9).

Calculation of a structural ensemble for the β3 cytoplasmic domain—NOE distance restraints were derived from a 3D ^{15}N-edited NOESY, 3D aliphatic ^{13}C-edited NOESY, 3D aromatic ^{13}C-edited NOESY, and a 4D ^{13}C-edited NOESY (75). Hydrogen bonding distances and geometry restraints (90) were implemented for the backbone amides of the β3 regions Glu711-Asp723, Glu726-Ala736, and Pro745-Ile758, predicted to reside in α-helices based upon NOEs and TALOS+. The ϕ and ψ dihedrals of β3 residues Cys712-Thr758 (excluding Arg724, Lys738 and Trp739) were restrained based on a statistical analysis of chemical shifts using the TALOS+ algorithm (85). Structures were calculated using CYANA (84) and refined with XPLOR-NIH using a protocol similar to the anneal.py and refine.py example scripts that come with the software package (88, 91). A summary of the structural restraints is reported in Table S2.1.

Circular Dichroism (CD) spectroscopy of lipid-conjugated β3. CD spectra were taken on a JASCO J-810 spectropolarimeter. 15 μM β3 was

conjugated to 1 mM total lipid and probed in 25 mM phosphate with 100 mM NaCl, pH 6.8. Spectra of free β3 were obtained of 30 μM β3. Measurements were made stepwise for each 1 nm between 200 nm to 240 nm and averaged over three scans.

Pepsin-LC-MS/MS HDX. A stock solution consisted of 15 μM β3 peptide or β3 peptide conjugated to lipid in 25 mM phosphate and 100 mM NaCl, pH 6.8. H-to-D exchange was initiated by diluting 5 or 10 μL of peptide stock solution into 15 or 10 μL of deuterated buffer, respectively. The reaction mixtures were then incubated for 10 seconds to 1.4 hours, as were non-deuterated control samples. Peptides fragments were collected on a reverse phase trap column (4 μL bed volume, ExSAR) for 3 min. Peptide fragments were eluted from the trap and separated chromatographically on a reverse phase column (4 μL bed volume, ExSAR) using a linear HPLC gradient of 12% to 45% acetonitrile over 11 minutes (pH 2.5, 0°C) at a 6 μL/min flow rate.   Peptides were ionized by ESI for mass spectrometric analysis in a Thermo Fisher OrbiTrap-LTQ.

Resulting mass spectra were analyzed using the DXMS software package (Sierra Analytics). The deuterium values per peptide were corrected for the deuterium content in the reaction conditions, as well as for deuterium loss in liquid handling by assuming an average of 75% deuterium recovery.   Intrinsic exchange curves were generated using HXpep (92). Experimental curves were generated from the exchange rates generated by exponential fitting of intrinsic curves. Fitting of the

48

experimental curves gives the slowing factor, which is a measure of the H-to-D exchange protection when compared to a random coil structure.

Supplemental

Table S2.2.1 Summary of β3 structure statistics

Conformationally restricting distance constraints	
Intraresidue [$i = j$]	202
Sequential [$|i − j| = 1$]	259
Medium Range [$1 < |i − j| < 5$]	235
Long Range [$|i − j| => 5$]	16
Total	712
Dihedral angle constraints	
φ	42
ψ	42
Hydrogen bond restraints	24
Average number of constraints per residue	15.2
Average number of distance constraints violations per Xplor-NIH conformer	
> 0.5 Å	0
Average number of dihedral-angle constraint violations Xplor-NIH conformer	
> 5°	0
Average r.m.s.d. to the mean coordinates [Å]	
Residues 713-723 and 726-736, backbone heavy atoms	0.68 ± 0.25
Residues 713-723 and 726-736, all heavy atoms	1.56 ± 0.27
Residues 713-723,726-736 and 745-758 , backbone heavy atoms	4.63 ± 1.37
Residues 713-723,726-736 and 745-758, all heavy atoms	5.27 ± 1.46
PROCHECK(93) G-factors Z-score for all residues (φ and ψ / all dihedral angles) [a]	2.08 / 1.89
PROCHECK(93) G-factors Z-score for ordered residues (φ and ψ / all dihedral angles) [b]	2.68 / 2.60
MOLPROBITY(94) clash Z-score (all residues [a] / ordered residues [b])	-1.18 / -1.18
Ramachandran plot summary [%] (all residues [a] / ordered residues [b])	
most favored regions	90.8 / 94.5
Additionally allowed regions	7.8 / 5.2
generously allowed regions	1.1 / 0.3
disallowed regions	0.3 / 0.0

[a] Residues 709 - 762
[b] Residues 711-735, 738-758

Chapter 3 The affinity of talin-1 for the β3-integrin cytosolic domain is determined by its phospholipid bilayer environment.

Abstract

Binding of the talin-1 FERM domain to the β3 cytosolic tail causes activation of the integrin αIIbβ3. The FERM domain also binds to acidic phospholipids. Although much is known about the interaction of talin-1 with integrins and lipids, the relative contribution of each interaction to integrin regulation and possible synergy between them remain to be clarified. Here, we examined the thermodynamic interplay between FERM domain binding to phospholipid bilayers and to its binding sites in the β3 tail. We found that although both the F0F1 and F2F3 subdomains of the talin-1 FERM domain bind acidic bilayers, the full-length FERM domain bound with an affinity similar to F2F3, indicating that F0F1 does not significantly increase the affinity for the membrane. When free in solution, the β3 tail has weak affinity for the FERM domain. However, appending the tail to acidic phospholipids increased its affinity for the FERM domain by three orders of magnitude. Nonetheless, the affinity of the FERM for the appended tail was similar to its affinity for binding to bilayers alone. Thus, talin-1 binding to the β3 tail is a ternary interaction dominated by a favorable surface interaction with phospholipid bilayers and set by lipid composition. Nonetheless, interactions between the FERM domain, the β3 tail, and lipid bilayers were not optimized for a high-affinity synergistic

interaction, even at the membrane surface. Instead, the interactions appeared to be tuned in such a way that the equilibrium between inactive and active integrin conformations can be readily regulated.

I. Introduction

The integrin αIIbβ3 resides on the platelet surface in equilibrium between resting and active conformations (5, 6, 95-97). On circulating platelets, αIIbβ3 is constrained in its inactive conformation to prevent spontaneous platelet aggregation. Similarly, the cytoskeletal protein talin-1, whose binding to the β3 cytosolic tail (CT) stabilizes the active conformation of αIIbβ3 (98-100), is sequestered away from the β3 CT (101). Besides interacting with integrins, talin-1 interacts with negatively-charged phospholipids (102-104) and phosphoinositides (31, 33, 105, 106). Stimuli generated at sites of vascular damage recruit talin-1 to the platelet plasma membrane, thereby promoting αIIbβ3 activation (12, 19). Much is known about the interaction of talin-1 with integrins and lipids, but the relative contribution of each interaction to integrin regulation and possible synergy between them remain to be clarified. Elucidating these interactions is important for understanding events leading to and controlling the formation of integrin complexes and for potential pharmacologic modulation of integrin signaling.

Talin-1 is a 250 kD protein containing a 45 kD N-terminal head domain attached via a flexible linker to a 200 kD C-terminal rod domain (99). Because the head domain is packed against the rod domain in its inactive state (107), talin-1 recruitment to the membrane and to integrin β CTs requires disruption of this interaction (108). At integrin-mediated cellular adhesions, the orientation of talin-1 is highly polarized, with its head domain associated with the plasma membrane and its rod domain making numerous cytoskeletal contacts (108).

The talin-1 head domain is a member of the FERM (4.1/Ezrin/Radixin/Moeisin) domain family (109, 110). Canonical FERM domains, such as that of radixin, consist of F1, F2, and F3 subdomains adopting ubiquitin, acyl-CoA-binding protein, and PTB/PH domain folds, respectively, and are assembled into a trefoil arrangement (Figure 3.1 A and B). The talin-1 FERM domain contains a fourth subdomain, F0, preceding F1 that also adopts a ubiquitin-like fold (111). The four talin-1 subdomains have an extended, nearly linear, configuration (PDB code 3ivf, Figure 3.1C) (104). Whereas radixin binds its targets, such as the CD44 CT, in a groove formed by helix α1 and strand β5 of its F3 subdomain in an anti-parallel β-β fashion (Figure 3.1A), the talin-β integrin CT complex contains a second interface with the N-terminal helical portion of the CT (Figure 3.1D) (61, 112). This positions talin to modulate interaction between membrane-proximal cytosolic and transmembrane segments of integrin α and β subunits (1, 61, 112).
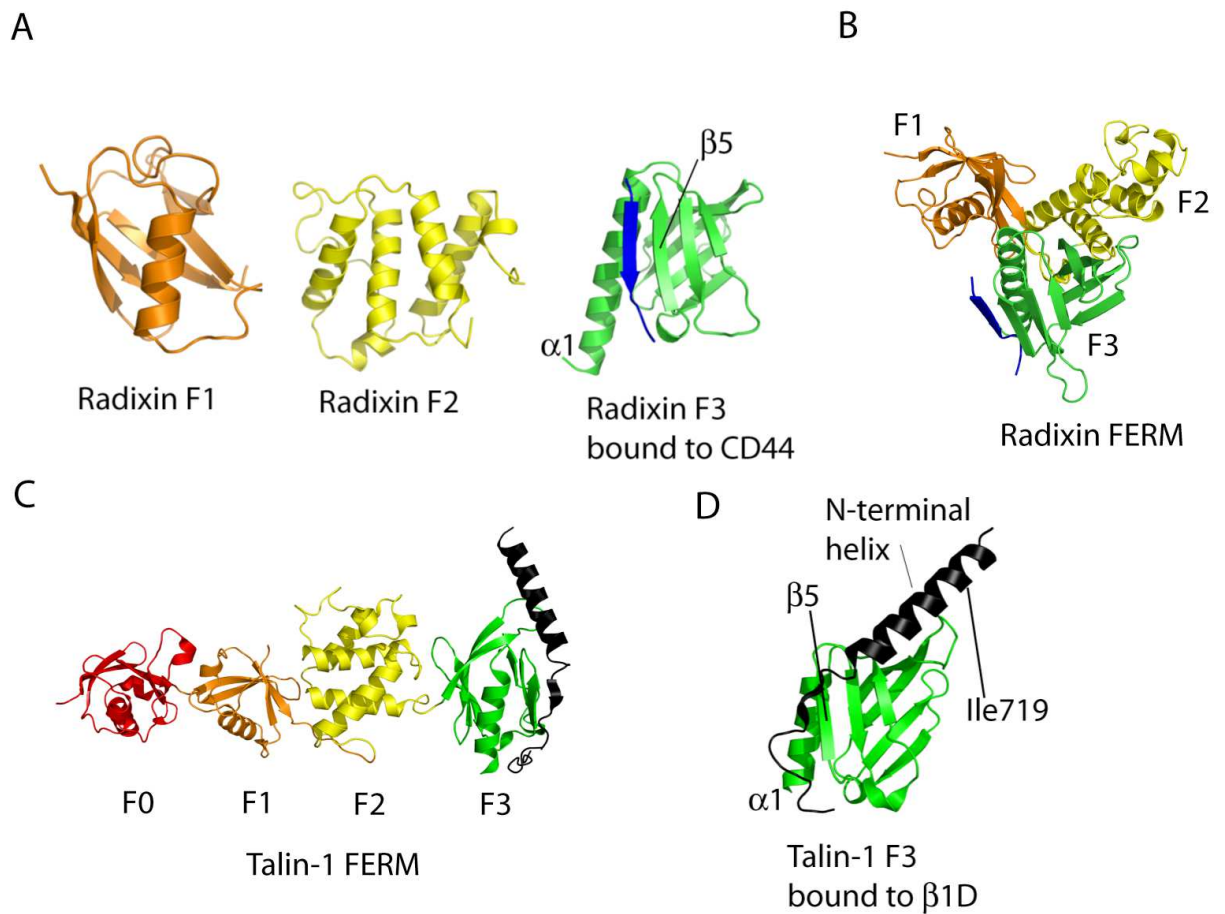
Figure 3.1 Comparison of the Talin-1 and Radixin FERM domains.

(A) The radixin FERM domain is composed of three subdomains: F1 (left, orange), F2 (center, yellow), and F3 (right, green). The CD44 cytoplasmic tail (blue) binds to a cleft in F3 formed by helix α1 and strand β5. (B) The radixin subdomains adopt a canonical trefoil shape. (C) The talin-1 FERM domain contains F1 (orange), F2 (yellow), and F3 (green) domains, as well as an F0 subdomain (red) that precedes F1. Instead of a trefoil, the talin-1 FERM subdomains are arrayed linearly. (D) Model of talin-1 F3 (green) bound to the integrin β1D CT (black). Two regions of the β1D CT interact with talin-1 F3: its C-terminal portion adopts an extended conformation and packs against a ridge formed by the interface of helix α1 and strand β5 in F3, while an N-terminal α-helix and a contiguous portion of the β1 transmembrane (TM) domain packs against the top of F3. Radixin structures were generated from PDB 2zpy. Talin-1 structures were modeled using PDB 3g9w and PDB 3ivf.

Here, we examine the thermodynamic interplay between phospholipid bilayers and β CT binding sites in the talin-1 FERM domain. The impetus for this study arose, in part, from conflicting findings regarding the ability of the talin-1 FERM domain to interact with the $\beta3$ CT. In solution, the affinity of talin-1 for β integrin CTs is nearly 1000-fold weaker than the affinity of radixin for CD44 (113) or of talin-1 for the C-terminus of PIP5KI-γ (61). However, talin-1 binds to the $\beta3$ CT with high affinity when the CT is immobilized on a carboxy-methylated dextran surface (114). This suggests that the interaction of talin-1 with integrins is optimal when the β subunit CT is presented on a hydrophilic negatively-charged surface such as the inner leaflet of plasma membranes.

To assess the interplay between membrane and β CT binding interactions, we tested whether the talin-1 FERM subdomains F0F1 and F2F3 (Figure 3.2B and C), each of which can interact with membranes (111), bind cooperatively or independently to a variety of negatively charged lipids and compared their binding to the complete FERM domain (F0-F3, Figure 3.2A). We then measured the effect of the membrane environment on the affinity of FERM domain binding to the $\beta3$ CT. We found that although the membrane environment increased the overall affinity of the FERM domain for $\beta3$, the interactions between the FERM domain, the $\beta3$ CT, and lipid bilayers were not optimized for a high-affinity synergistic interaction, even at the membrane surface. Instead, the

55

interactions appeared to be tuned in such a way that the equilibrium between inactive and active integrin conformations can be readily regulated.

A
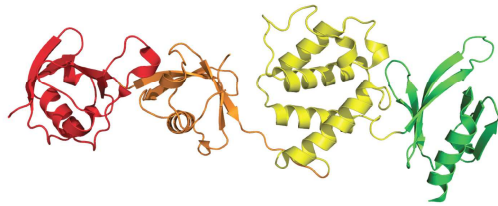
Talin-1 F0F1F2F3: LVPR -|- GSHM-V^{2}ALSLKISI....DIILKKKKS^{425}
                     Thrombin/MCS

B

Talin-1 F0F1: LVPR -|- GSHM-V^{2}ALSLKISI....LRRKFFYSD^{201}
                 Thrombin/MCS

C
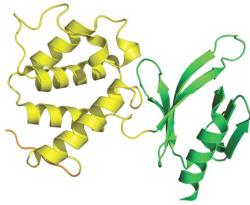
Talin-1 F2F3: LVPR -|- GSHM-S^{206}RDPVQLNL....DIILKKKKS^{425}

D

β3: LVPR -|- GSHMG-C^{719}-TIH**DRKEFAKFEEERARAKWDTANNPLY**KEATSTFTNITYRGT^{762}
       Thrombin/MCS

BODIPY-β3: LVPR -|- GSHMG-C^{719}-TIH**DRKEFAKFEEERARAKWDTANNPLY**KEATSTFTNITYRGT^{762}
                      Maleimide-BODIPY-TMR

LIPID-β3: LVPR -|- GSHMG-C^{719}-TIH**DRKEFAKFEEERARAKWDTANNPLY**KEATSTFTNITYRGT^{762}
                     Maleimide-PE (C16)$_2$

E

FITC-PIP5K1γ: FITC-βAla-S^{646}WVYSPLHY^{654}

Figure 3.2 Talin-1 and αIIbβ3 constructs used.

Talin-1 constructs encompassing the (A) F0, F1, F2, and F3 subdomains, (B) the F0 and F1 subdomains, and (C) the F2 and F3 subdomains. Each construct contains an N-terminal Gly-Ser-His-Met (GSHM) motif enabling cleavage by thrombin. (D) β3 CT constructs include the entire CT including the talin-1 recognition motif (bold) and preceded by a Cys residue at position 719 as well as an N-terminal GSHMG sequence for cleavage by thrombin (top); a fluorescent β3 CT construct in which a maleimide-BODIPY-TMR moiety is appended to C719 (middle); and a β3 CT construct in Cys719 was covalently modified with maleimide-functionalized phosphatidylethanolamine (bottom). (E) FITC-labeled peptide derived from PIP5KIγ. *{All talin and integrin constructs cloned, expressed, and purified by DTM. PIP5K1γ was synthesized by HJ.}*

II. Results

The talin-1 FERM domain contains an extended positively-charged surface.

Projection of an electrostatic surface on the talin-1 FERM domain revealed that it contains an extended positively-charged surface (Figure 3.3) (104). This is especially pronounced for the F2 and F3 subdomains. The F0 and F1 subdomains also contain positively charged surfaces and F1 contains a flexible loop that readily binds to membranes but was removed for crystallization (107). The positively-charged surfaces on F0F1 are not completely aligned with those on F2F3. Although this could reflect a strong bias for maintaining the surfaces in an unaligned state in solution or the selection of a single conformation from a flexible ensemble due to crystal packing, X-ray scattering studies argue against a flexible ensemble of structures (104). Thus, if the solution conformation is maintained, F0F1 should make only modest contributions toward the affinity of the overall complex over that of the F2F3 alone. Alternatively, if F0F1 and F2F3 change their mutual orientation away from the minimum energy solution

58

conformation, this would attenuate the affinity relative to the value expected if they were pre-organized to interact favorably with the surface.
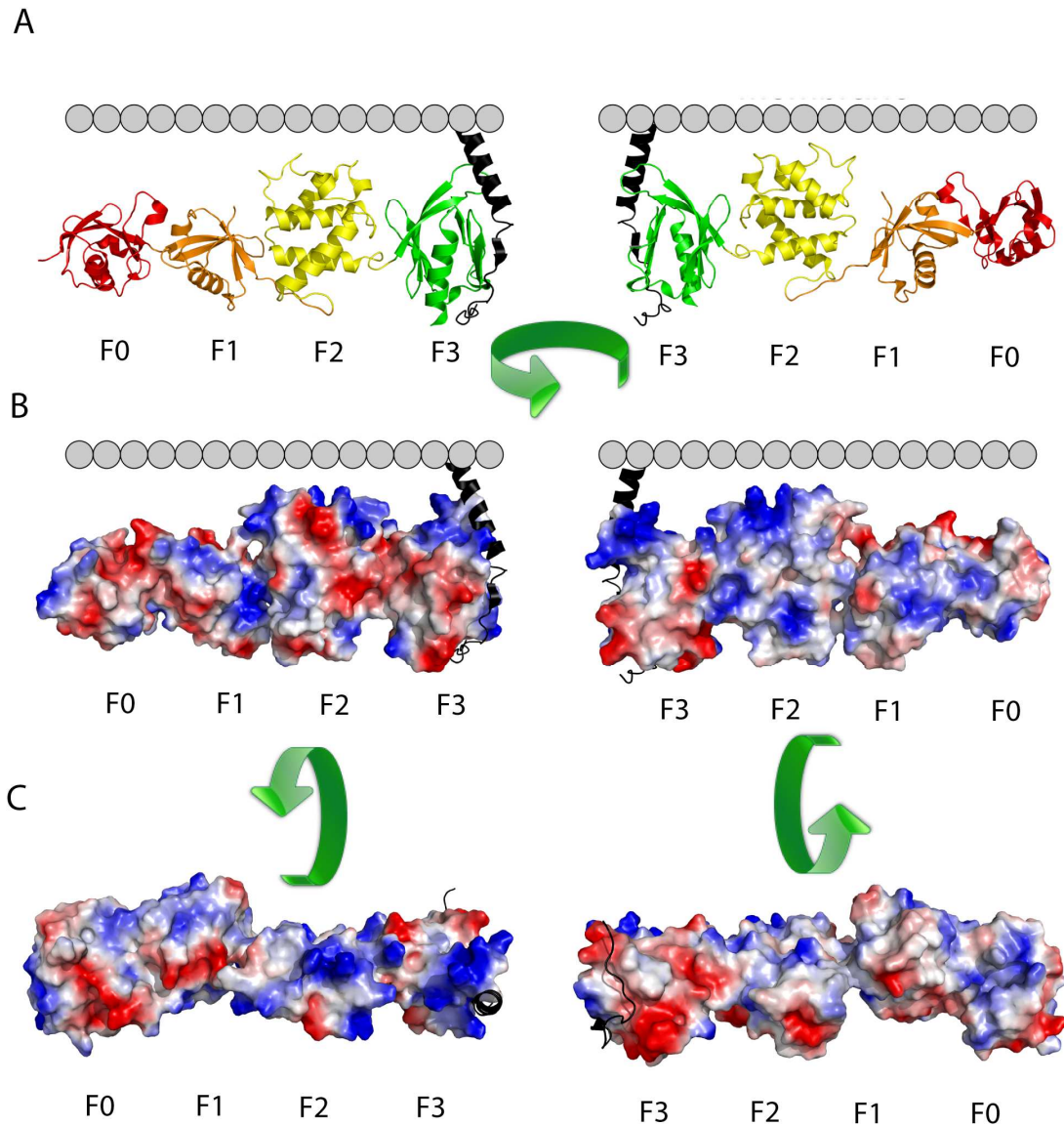
Figure 3.3 Orientation of the talin-1 FERM domain with respect to the inner leaflet of the plasma membrane.

As in Figure 3.1, the talin-1 F0-F3 subunit bound to a β-integrin was modeled using the crystal structure of the talin-1 FERM domain (pdb code 3ivf). (A) The interaction of talin-1 with the β integrin CT (black) places its FERM domain in proximity to the inner plasma membrane leaflet.   (B)

Projection of an electrostatic surface onto the talin-1 FERM domain. Red denotes negative and blue denotes positive-charge density. (C) Talin-1 FERM domain rotated 90° showing the electrostatic surface as viewed from the membrane (left) and cytosol (right). *{Models were generated by DTM using PyMOL}*

Binding of the talin-1 FERM domain fragment F2F3 to negatively-charged phospholipids.

Before studying the interaction of the talin-1 FERM domain with the β3 CT tethered to membrane, we investigated whether the F2F3 subdomain, which makes the most direct contact with the β3 CT, differentially recognizes negatively-charged phospholipids. We used surface plasmon resonance (SPR) to measure the interaction of F2F3 with phospholipid bilayers immobilized on a hydrophobically-modified Biacore L1 SPR chip (115). All measurements were made relative to a surface containing 100% phosphatidylcholine (PC). F2F3 binding to 20% POPS and 80% POPC was measured at steady state (Figure 3.4A) and conformed to a single-site binding model as a function of F2F3 concentration. The dissociation constant (K_d) for F2F3 binding to 20% phosphatidylserine (PS)-containing bilayers was 0.92 μM (Table 3.1). In comparison, the K_d for bilayers containing 10% PtdIns*(4,5)P₂* was 0.67 μM, suggesting that the F2F3 may have a slight preference for PtdIns*(4,5)P₂* over PS. Nonetheless, F2F3 bound to bilayers containing the diphosphoinositides PtdIns(3,5)*P₂* and PtdIns(3,4)*P₂* and the monophosphoinositide PtdIns(5)*P* with affinities similar to PtdIns*(4,5)P₂* and largely within the error of measurements (Figure 3.4B, Table 3.1),

60

indicating that it does not strongly differentiate between the negatively

charged head groups.

A
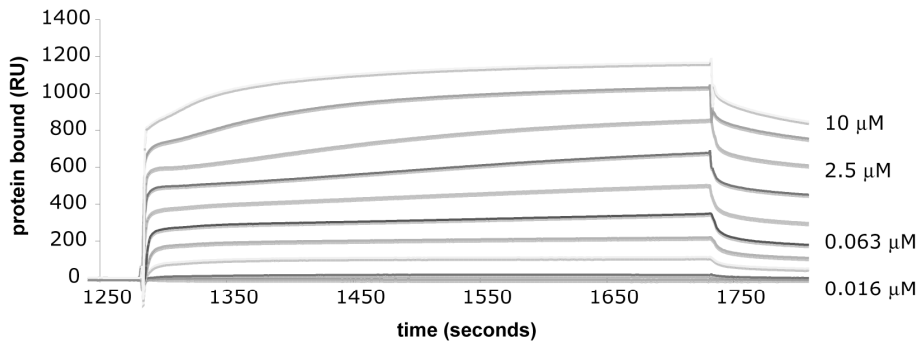
B
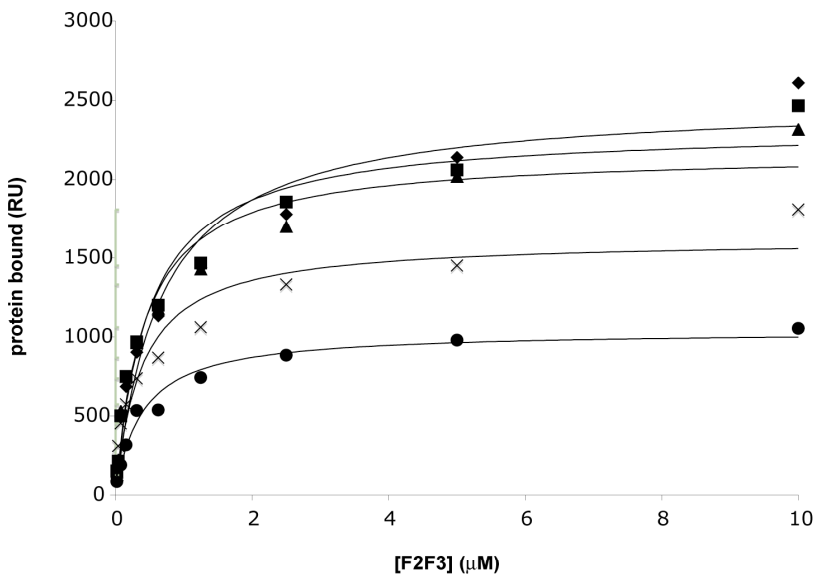
C
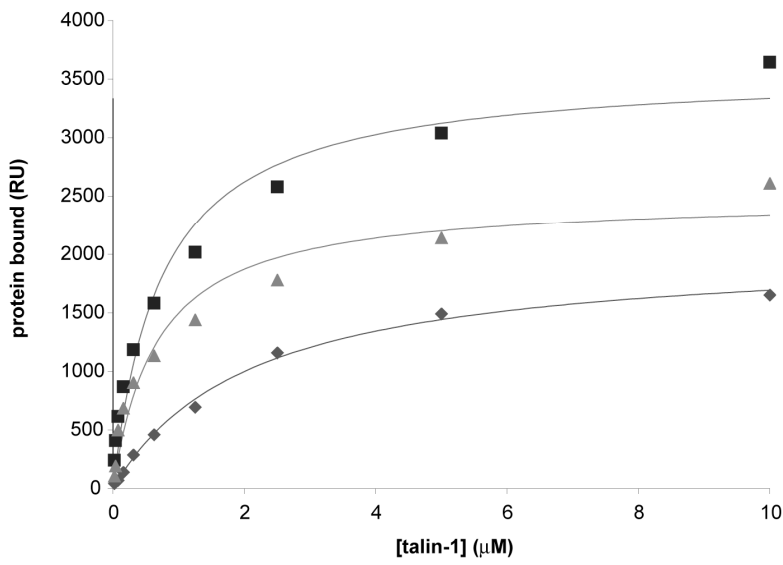
Figure 3.4 Steady state binding of the talin-1 FERM domain and its subdomains to phospholipid bilayers.

(A) SPR sensorgrams of F2F3 binding to a bilayer composed of 20% POPS and 80% POPC immobilized on a Biacore L1 SPR chip. F2F3 was injected in 2-fold increments up to a concentration of 10 μM. (B) Steady-state isotherms for F2F3 binding to negatively-charged phospholipids. Diamonds, 10% PtdIns(4,5)P_2; squares, 10% PtdIns(3,5)P_2; triangles, 10% PtdIns(3,4)P_2, Xs, PtdIns(5)P, circles, 20% phosphatidylserine. (C) Steady-state isotherms for F0-F3 (squares), F2F3 (triangles), and F0F1 (diamonds) binding to bilayers containing 10% PtdIns(4,5)P_2. Data from (B) and (C) were fit to a one-site binding model using BIAevaluation software. *{Three independent experiments were performed. Protein was purified by DTM. SPR was performed by PN. Data analysis was performed by DTM and PN.}*

Table 3.1 Steady-state SPR measurements of talin-1 F2F3 subdomain binding to phospholipids.

Binding to the indicated phospholipids (Figure 3.4B) was fit to a one-site binding model using BIAevaluation. The data represent the mean and standard deviations of three independent experiments.

Lipid (%)	K_d (μM)	Maximum Binding (RU)
PS (20%)	0.92 ± 0.260	1210 ± 66
PtdIns(4,5)P_2 (10%)	0.67 ± 0.07	2490 ± 225
PtdIns(3,4)P_2 (10%)	0.42 ± 0.09	2170 ± 146
PtdIns(3,5)P_2 (10%)	0.50 ± 0.053	2330 ± 193
PtdIns(5)P (10%)	0.37 ± 0.029	1770 ± 146

The total amount of F2F3 bound to bilayers depended on the net negative charge of the membrane, suggesting that electrostatics play a substantial role in the interaction. PtdIns(4,5)P_2, PtdIns(3,5)P_2, and PtdIns(3,4)P_2 each have a charge of (-4) per head group, while PtdIns(5)P

has a charge of (-3), and PS has a charge of (-1). If the interaction were dependent of charge, the amount of protein bound to 10% PtdIns(5)P, would be expected to be roughly ¾ the amount bound to 10% diphosphoinositides. Similarly, ½ as much talin-1 would be expected to bind to 20% PS as to 10% diphosphoinositides. The maximum resonance units (RU) of F2F3 bound to 10% PtdIns(4,5)P_2, 10% PtdIns(3,5)P_2, and 10% PtdIns(3,4)P_2 were similar at 2490, 2330, and 2170 RU, respectively. We found that approximately ¾ the amount of F2F3 bound to 10% PtdIns(5)P (1770 RU) and ½ the amount bound to 20% PS (1200 RU), confirming that total protein bound depends on the charge of the membrane.

Binding of talin-1 FERM domain and its subdomains to PtdIns(4,5)P$_2$.

Next, we compared the affinity of the complete talin-1 FERM domain (F0-F3) for PtdIns(4,5)P_2 with that of F0F1 and F2F3. PtdIns(4,5)P_2 was chosen as the lipid substrate for these measurements because F2F3 did not differentiate between various phosphoinositides. Phospholipid bilayers containing 10% PtdIns(4,5)P_2 were immobilized on a Biacore L1 chip and all measurements were made relative to a surface containing 100% PC. We found that F0-F3 bound to 10% PtdIns(4,5)P_2 with a K_d of 980 nM, comparable to the K_d for F2F3 of 670 nM, whereas the K_d for F0F1 was 2.6 μM (Table 3.2). Thus, both F0F1 and F2F3 readily interact with PtdIns(4,5)P_2, but when combined, the affinity for

bilayers was not enhanced. The relative stoichiometries of F0F1, F2F3, and F0-F3 also suggest that the subdomains do not form a cooperative membrane binding surface. The mass ratios for F0-F3, F2F3, and F0F1 are 2:1.1:1.0. F0-F3 has twice the mass of F2F3 and nearly twice the resonance units of F0-F3 (3960 RU) bound to the sensor chip as F2F3 (2490 RU) (Figure 3.4C, Table 3.2). Thus, F0-F3 and F2F3 have similar stoichiometries for the phospholipid surface. A similar amount of F0F1 bound to the sensor chip (2290 RU) as F2F3, but with lower affinity. Thus, although F0F1 can interact with PtdIns(4,5)P_2, the affinity and stoichiometry of the full FERM domain for PtdIns(4,5)P_2 is similar to that of F2F3, indicating that F0F1 does not substantially cooperate with F2F3 in FERM domain binding to membranes.

Table 3.2 Steady-state SPR measurements of talin FERM domain binding to phospholipid bilayers containing 10% PtdIns(4,5)P$_2$.

Binding results were fit to a one-site binding model using BIAevaluation. The data shown represent the mean and standard deviation of three independent experiments.

FERM domain construct	K_d (µM)	Maximum Binding (RU)
F0-F3	0.98 ± 0.10	3960 ± 258
F2F3	0.67 ± 0.07	2490 ± 220
F0F1	2.63 ± 0.84	2290 ± 258

Enthalpy of talin-1 FERM domain binding to PtdIns(4,5)$_2$.

It has been reported that the talin-1 FERM domain bind to negatively-charged vesicles in solution (104, 105, 111, 116, 117). To confirm these observations, we used isothermal titration calorimetry (ITC) to measure the enthalpy of F0-F3 binding to large unilamellar vesicles (LUVs) composed of 90% POPC and 10% PtdIns(4,5)P_2. As a positive control, we measured binding of the pleckstrin homology (PH) domain of PLC-δ1 to PtdIns(4,5)P_2 (30).

Titration of 100 μM PLC-δ1 PH domain into a LUV suspension containing 1%, 3%, and 10% PtdIns(4,5)P_2 generated binding isotherms with molar enthalpies of -11.7 kcal/mol, -10.2 kcal/mol, and -12.8 kcal/mol and dissociation constants of 2.8 μM, 2.1 μM, and 4.2 μM, respectively (Figure 3.5A, Table 3.3). These results are comparable to a previously published binding enthalpy of -11.9 kcal/mol and K_d of 1.1 μM for PLC-δ1 PH domain binding to 1% PtdIns(4,5)P_2 bilayers (30).
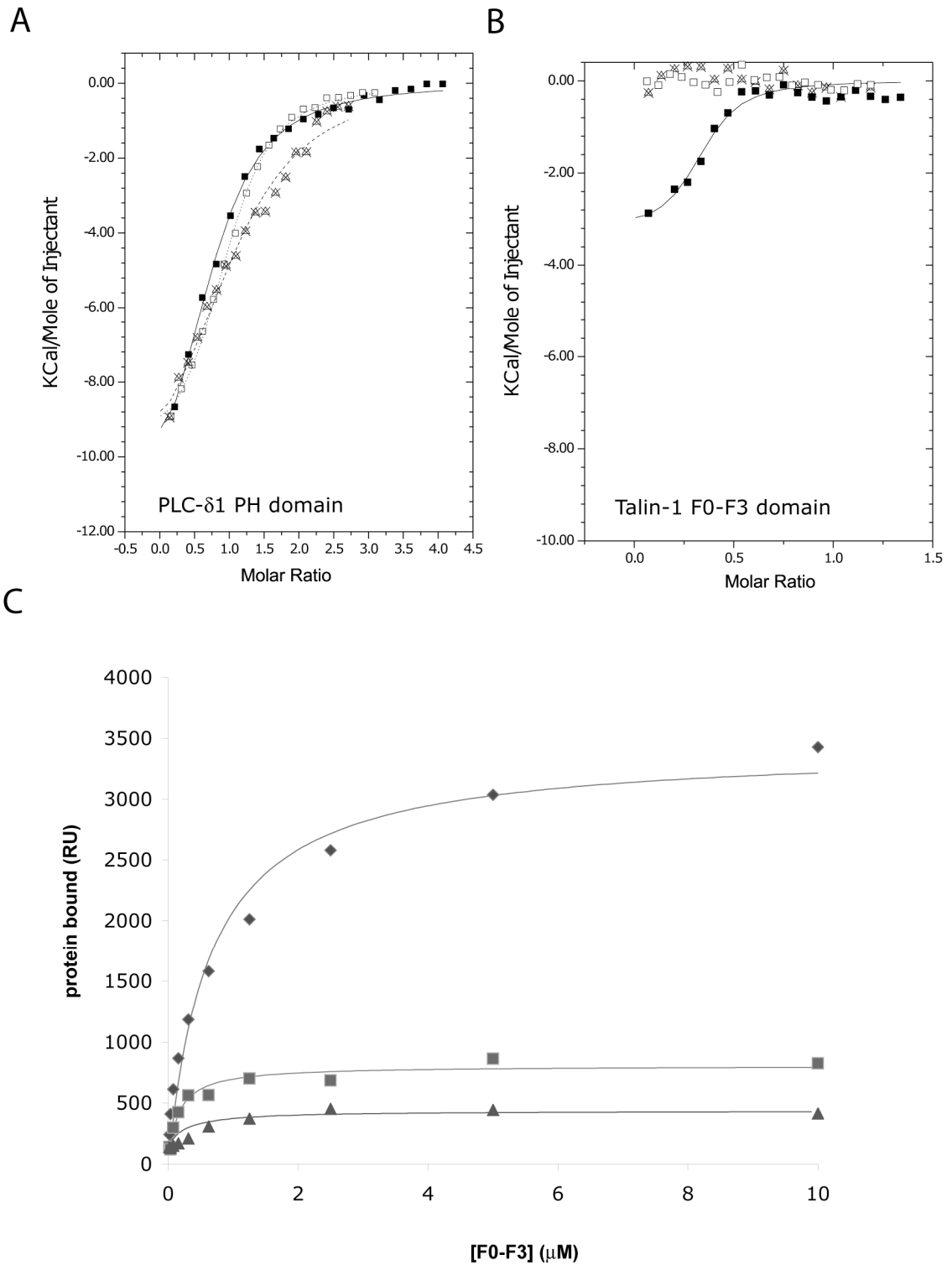
Figure 3.5 Comparison of PLC-δ1 PH domain and talin-1 FERM domain binding to PtdIns(4,5)P_2 and Ins(1,4,5)P_2.

(A) ITC titration of 100 μM PLC-δ1 PH domain into LUVs containing 1% (X), 3% (open squares), and 10% (closed squares) PtdIns(4,5)P_2. The titrations were globally fit to a OneSite binding model using MicroCal/Origin. (B) ITC titration of 190 μM talin-1 FERM domain (F0-F3) into LUVs containing 1% (X), 3% (open squares), and 10% (closed squares) PtdIns(4,5)P_2 No enthalpy was generated for 1% or 3% LUVs. Titration into 10% PtdIns(4,5)P_2 was globally fit to a OneSite binding model using MicroCal/Origin. (C) Steady-state binding isotherms for F0-F3 binding to 1% (triangles), 3% (squares) and 10% (diamonds) PtdIns(4,5)P_2 immobilized on a Biacore L1 SPR chip. *{PLC-δ1 ITC titrations were performed once to demonstrate accessibility of the PtdIns(4,5)P$_2$ headgroup. Talin-1 titration into 1% and 3% PtdIns(4,5)P$_2$ were performed in triplicate independent experiments. Talin-1 titration into 10% PtdIns(4,5)P$_2$ was performed in triplicate with the same protein sample. SPR data are representative of three independent experiments. ITC experiments were performed by DTM. DTM prepared protein samples for SPR experiments. PN performed SPR experiments. DTM and PN analyzed SPR data.}*

Table 3.3 ITC measurements of talin-1 FERM domain and PLC-δ1 binding to PtdIns(4,5)P$_2$ and Ins(1,4,5)P$_3$.

Measurements were performed at 20ºC in 25 mM MOPS pH 6.8 with 100 mM NaCl. Background heats of dilution were subtracted. Titrations were fit to OneSite binding isotherms using MicroCal/Origin and errors are reported as fitting errors. There was no net enthalpy for titration of F0-F3 into 1% and 3% PtdIns(4,5)P_2 and 2 mM Ins(1,4,5)P3. *{PLC-δ1 ITC experiments were performed once to demonstrate accessibility of PtdIns(4,5)P$_2$ on the bilayer surface – errors represent fitting errors. Talin-1 titration into 1% and 3% PtdIns(4,5)P$_2$ were performed in triplicate independent experiments. Talin-1 titration into 10% PtdIns(4,5)P$_2$ was performed in triplicate with the same protein sample. Talin-1 errors are standard deviations. }*

	K_a (x10^6 M^{-1})	K_d (μM)	ΔH (kcal/mol)	ΔS (cal/mol/K)	n
F0-F3 + 1% PtdIns(4,5)P_2	--------	--------	--------	--------	--------
F0-F3 + 3% PtdIns(4,5)P_2	--------	--------	--------	--------	--------

F0-F3 + 10% PtdIns(4,5)P_2	1.3 ± 0.6	0.781	-3.3 ± 0.4	-17.0	0.33 ± 0.03
F0-F3 + 2 mM Ins(1,4,5)P_3	--------	--------	--------	--------	--------
PLC-δ1 + 1% PtdIns(4,5)P_2	0.36 ± 0.08	2.82	-11.7 ± 1.0	-14.0	1.13 ± 0.07
PLC-δ1 + 3% PtdIns(4,5)P_2	0.47 ± 0.03	2.11	-10.2 ± 0.2	-8.37	0.97 ± 0.01
PLC-δ1 +10% PtdIns(4,5)P_2	0.24 ± .02	4.20	-12.8 ± 0.7	-18.3	0.75 ± 0.03
PLC-δ1 + 2 mM Ins(1,4,5)P_3	1.4 ± 0.2	0.72	-17.5 ± 0.7	-30.5	0.80 ± 0.02

Next we titrated 190 µM F0-F3 into a suspension of LUVs composed of 90% POPC and 10% PtdIns(4,5)P_2. After subtracting the heat of dilution, F0-F3 binding was slightly exothermic (≈ -3 kcal/mol) with a stoichiometry of ≈ 1 F0-F3 to 3 PtdIns(4,5)P_2 phospholipids (Figure 3.5B). Titration of higher F0-F3 concentrations resulted in precipitation of the mixture in the calorimetry cell – confirming the interaction of F0-F3 with membranes, but precluding thermodynamic analysis. Surprisingly, similar experiments using LUVs containing 1% and 3% PtdIns(4,5)P_2 did not generate measurable enthalpy (Figure 3.5B). Therefore, to confirm that F0-F3 actually binds to bilayers containing 1% and 3% PtdIns(4,5)P_2, we measured the interaction by SPR and found that it bound with high affinity (Figure 3.5C, Table 3.4). Furthermore, the amount of F0-F3 bound

to the chip scaled with the amount of PtdIns(4,5)P_2 on the surface. The Rmax for 10% PtdIns(4,5)P_2 was approximately 10 fold that for 1% PtdIns(4,5)P_2. The Rmax ratio of 10% to 3% PtdIns(4,5)P_2 was 4.4, which was greater than the expected 3.3. All other SPR measurements with F0F1, F2F3, and F0-F3 have Rmax values that scale appropriately with phospholipid charge and protein mass (Tables 3.1 and 3.2), therefore it is unclear why the 3% PtdIns(4,5)P_2 surface would deviate. The experiment was repeated several times with different protein preparations and lipid stocks.

Table 3.4 Steady-state SPR measurements of talin F0-F3 domain binding to phospholipid bilayers containing 10%, 3%, and 1% PtdIns(4,5)P_2.
Binding results were fit to a one-site binding model using BIAevaluation. The data shown represent the mean and standard deviation of three independent experiments.

Negatively Charged Phospholipid	K_d (µM)	Maximum Binding (RU)
10% PtdIns(4,5)P_2	0.98 ± 0.10	3960 ± 258
3% PtdIns(4,5)P_2	0.70 ± 0.21	901 ± 57
1% PtdIns(4,5)P_2	0.65 ± 0.28	427 ± 24

Lastly, we attempted to measure the interaction of F0-F3 with the inositol headgroup of PtdIns(4,5)P_2, Ins(1,4,5)P_3, free in solution (Figure 3.6). Two mM Ins(1,4,5)P_3 was titrated into a 150 µM F0-F3 solution, but

no binding enthalpy was generated. By contrast, titration of 120 μM
Ins(1,4,5)P_3 into a 6 μM solution of the PLC-δ1 PH domain generated an
exothermic binding curve with thermodynamic parameters comparable to
previously published results (Table 3.3) (30).
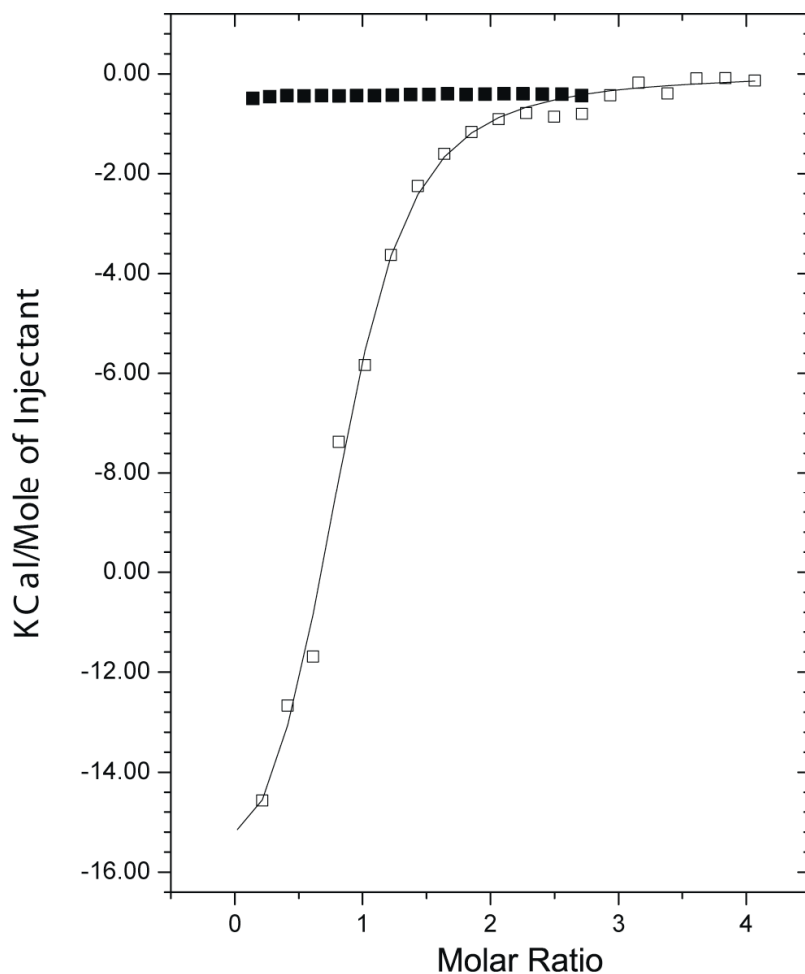
**Figure 3.6 Titration of Ins(1,4,5)P_3 into talin-1 F0-F3 does not
generate significant enthalpy.**

ITC titrations of 2 mM Ins(1,4,5)P_3 into 150 μM F0-F3 (filled squares) and
120 mM Ins(1,4,5)P_3 into 6.0 mM PLC-δ1 (open squares).   The titration
into PLC-δ1 could be fit to a OneSite model (MicroCal/Origin). All samples
were prepared in buffer matched 25 mM MOPS 100 mM NaCl, pH 6.8.
Background heats of dilution were subtracted.   *{Titration of Ins(1,4,5)P_3
into F0-F3 is representative of two independent experiments. Titration of
Ins(1,4,5)P_3 into PLC-δ1 was performed once to demonstrate activity of
Ins(1,4,5)P_3. Experiments performed by DTM.}*

Talin-1 FERM domain binding to the β3 CT immobilized on negatively charged carboxymethylated dextran.

Previous measurements of talin-1 FERM domain binding to the β3 CT used a β3 construct beginning at Lys716 and included a linker for attaching the construct to an SPR chip (114). Our β3 CT construct, designed to mimic the β3 CT as it exits the membrane, was attached via Cys719 to a CM-5 SPR sensor chip functionalized with N-[ε-maleimidocaproic acid]-hydrazide to generate thiol-reactive groups (Figure 3.2). F0-F3 was then flowed over the chip at concentrations up to 1.0 μM. The resulting sensorgrams (Figure 3.7A) could be fit to two binding events with dissociation constants of 155 nM and 3.5 μM. The biphasic behavior could have resulted from heterogeneity of β3 on the chip surface or heterogeneity of the interaction between F0-F3 and the carboxymethylated dextran (118). Regardless, the interaction between the talin-1 FERM domain and the β3 CT may be sensitive to such heterogeneity since we hypothesize that the FERM domain binds to the β3 CT and the inner membrane surface simultaneously. We chose not to pursue experiments with carboxy-dextran-immobilized integrin further, as membrane immobilized β3 is more biologically relevant and immobilization of small peptides on dextran matrices can result in heterogenous interaction surfaces.
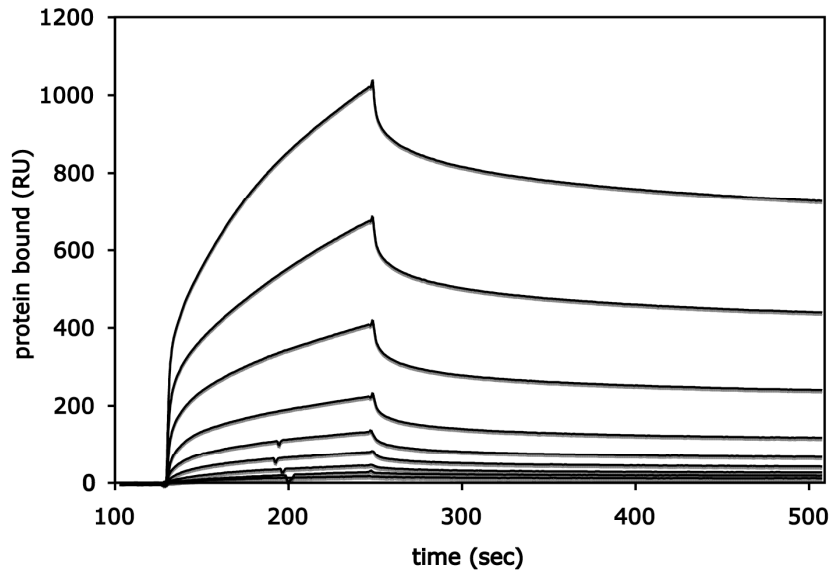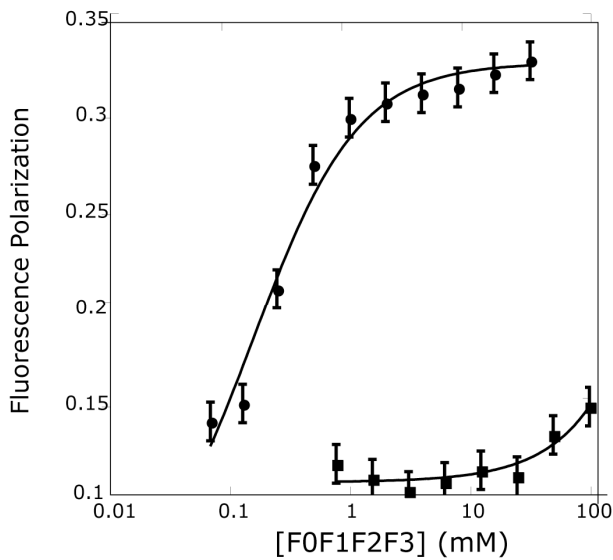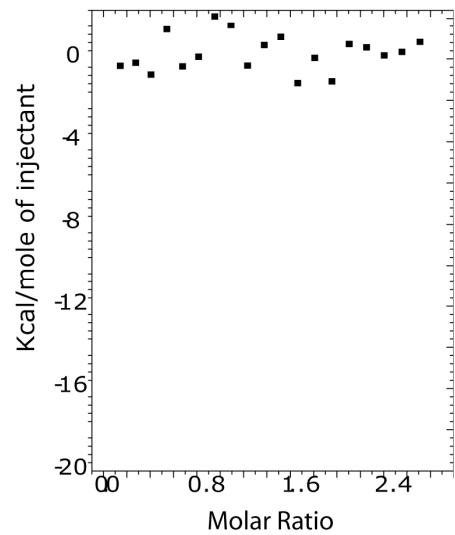
Figure 3.7. Talin-1 FERM domain binding to the β3 CT immobilized on negatively-charged surfaces or free in solution.

(A) The β3 CT (600 RU) was immobilized on a carboxy-methylated dextran SPR chip and F0-F3 to maximum concentration of 1 μM was flowed over the chip. (B) FP of F0-F3 titrated into 20 nM BODIPY-TMR β3. FP was measured at 575 nm after excitation at 530 nm (squares). F0-

F3 was also titrated into a 20 nM FITC-labeled PIP5KI-γ (black circles). FP was measured at 528 nm after excitation at 485 nm. (C) ITC of 140 µM β3 CT titrated into buffer-matched 10.5 µM F0-F3 revealed no significant enthalpy above the heat of dilution. ITC samples were in 25 mM MOPS 100 mM NaCl, pH 6.8. *{SPR data are representative of two independent experiments. Fluorescence polarization experiments were performed in triplicate using the same protein sample. ITC data are representative of three independent experiments – no binding enthalpy was generated in all three experiments.   SPR was performed and analyzed by PN using protein prepared by DTM. FP performed by DTM. PIP5K1γ peptide was prepared by HJ. Integrin peptide was prepared by DTM. ITC performed by DTM.}*

Binding of the talin-1 FERM domain to the β3 CT domain tethered to negatively-charged bilayer.

To address whether the talin-1 FERM domain binds the β3 CT and

a negatively-charged surface in a concerted fashion, we first used

fluorescence polarization (FP) and ITC to measure the affinity of talin-1

FERM domain for the β3 CT when both are free in solution.

For FP, the β3 CT was labeled with maleimide-functionalized

BODIPY-TMR at Cys719. When F0-F3, at concentrations up to 100 µM,

was titrated into a 20 nM solution of labeled β3 CT, the FP increased from

0.1 to 0.16. (Figure 3.7B). These results were fit to a binding isotherm

with a K_d of approximately 600 µM. Since the interaction between talin-1

and β3 CT was not saturated at the concentrations used, the exact

dissociation constant could not be calculated, however other laboratories

have reported values on the order of several hundred micromolar (62,

112), which is in line with our results. As a positive control for talin-1

activity, we titrated F0-F3 into a 20 nM solution of a fluorescein isothiocyanate (FITC)-labeled peptide corresponding to the C-terminus of PIP5KIγ (Figure 3.7B). The resulting change in FP was fit to an isotherm with a K_d of 160 nM ± 50 nM, consistent with reported affinities of 170 nM to 1.4 μM for other PIP5KIγ constructs with slightly different sequences (119, 120).

We also used ITC to confirm that the β3 CT and F0-F3 does not interact strongly in solution. There was no significant enthalpy above background heats of dilution when F0-F3, up to a final concentration of ≈ 30 μM protein, was titrated into 10 μM peptide (Figure 3.7C). This contrasts with a recent report in which talin-2 and the β1D cytoplasmic domain interacted with a K_d of ≈ 20 μM and a molar enthalpy of ≈ -17 kcal/mol (112). This difference is associated with several subtle but significant differences between the β1D CT and β3 CT sequences. Our result can be interpreted either as a lack of interaction between talin-1 and the β3 CT at the concentrations used or a lack of significant enthalpy at the concentrations used. Given that the structural similarity of the talin-2 / β1D interaction (ΔH ≈ -17 kcal/mol), we would expect the β3 interaction to have measurable enthalpy at the concentrations used in this experiment. Furthermore, the lack of observed enthalpy corroborates our FP data and previously published NMR experiments (62, 112).
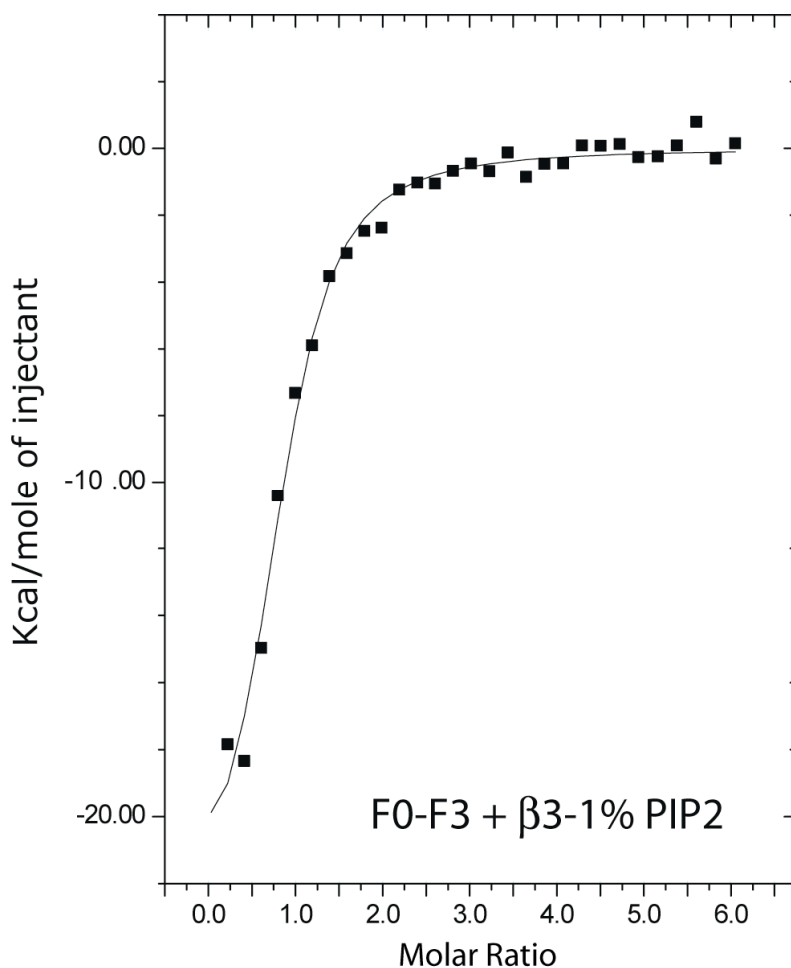
Figure 3.8. Talin-1 FERM domain binding to the β3 CT conjugated to phospholipid bilayers containing 1% PtdIns(4,5)P_2.

The β3 CT at a final concentration of 5 μM was immobilized onto the surface of LUVs containing 1% PtdIns(4,5)P_2 (20 μM)/ 2% maleimide-PE (40 μM) / 97% POPC (2 mM total lipid). Buffer matched talin-1 FERM domain (F0-F3, 150 μM) was titrated at 20°C into the suspension of immobilized β3. Background heats of dilution were subtracted. The titration was globally fit to a OneSite binding model using MicroCal/Origin. All ITC experiments were performed in 25 mM MOPS buffer 100 mM NaCl, pH 6.8. Thermodynamic parameters are summarized in Table 3.5. *{Data represent three independent experiments. Experiments performed by DTM.}*

Because the interaction between the talin-1 FERM domain and

PtdIns(4,5)P_2 occurs with very low enthalpy, we were able to use ITC to

76

measure talin-1 FERM domain binding to the β3 CT in the presence of PtdIns(4,5)P_2. Accordingly, we immobilized the β3 CT on phospholipid bilayers by reacting a β3 CT construct containing Cys at residue 719 with maleimide-functionalized phosphatidylethanolamine on the surface of LUVs composed of POPC and 1% PtdIns(4,5)P_2, 20% PS, or 20% PS + 1% PtdIns(4,5)P_2 (1). Titration of F0-F3 into a suspension of LUVs containing 1% PtdIns(4,5)P_2 in the absence of immobilized β3 CT (Figure 3.5B) or into buffer containing the free β3 CT (Figure 3.4C) generated little or no enthalpy. By contrast, titration of 150 μM F0-F3 into a LUV suspension containing 5 μM β3 CT immobilized on 1% PtdIns(4,5)P_2 was exothermic (Figure 3.8). The titration was globally fit to a one-site binding isotherm, revealing a K_d of 860 nM and a molar enthalpy of -25.0 kcal/mol (Table 3.5). When the experiments were repeated with the β3 CT immobilized on bilayers containing 20% PS or 20% PS with 1% PtdIns(4,5)P_2 similar results were obtained (Figure 3.9A/B; Table 3.5). Thus, these experiments demonstrate that immobilizing the β3 CT on phospholipid bilayers increases its affinity for the talin-1 FERM domain by at least three orders of magnitude compared to the β3 CT free in solution, increasing its affinity from that of a very weak to a high-affinity interaction.
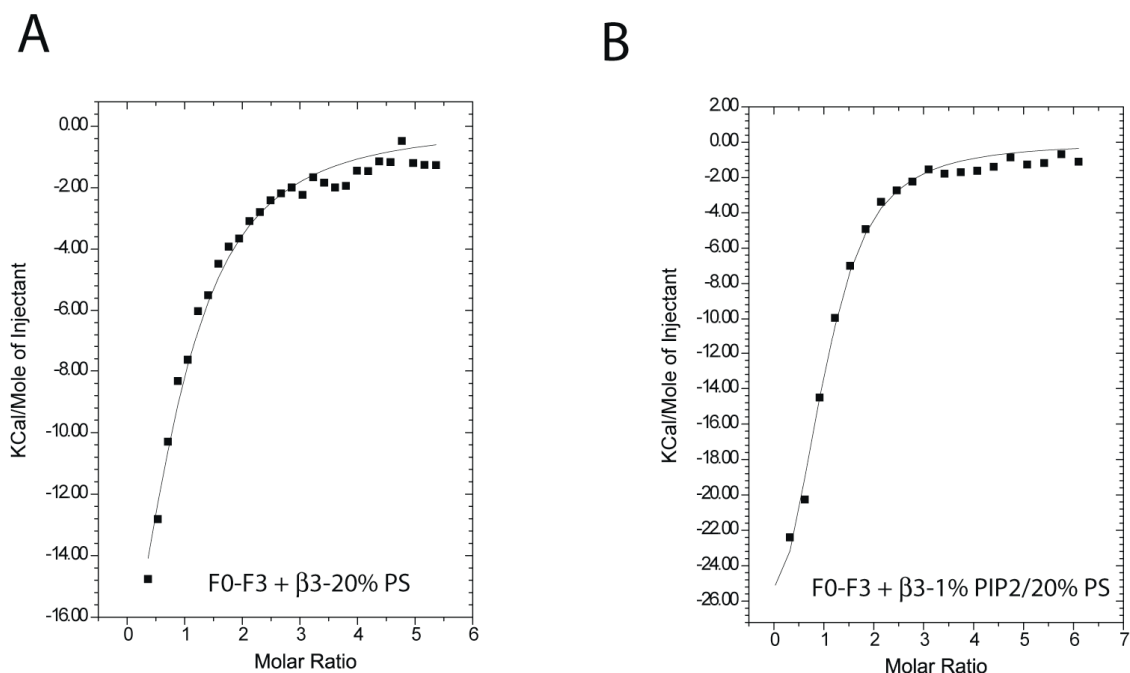
Figure 3.9 FERM domain binding to the β3 CT conjugated to negatively-charged phospholipid bilayers.

As in Figure 3.5k, the talin-1 FERM domain (F0-F3, 150 µM) was titrated at 20°C into a buffer-matched suspension of LUVs composed of (A) 20% PS or (B) 20% PS + 1% PtdIns(4,5)P_2 to which 5 µM β3 CT had been conjugated via a maleimide-functionalized lipid head group (Methods). The titrations were globally fit to a OneSite binding model using MicroCal/Origin. Thermodynamic parameters are summarized in Table 3.5. *{Data are representative of triplicate experiments performed with the same protein sample. Experiments were performed by DTM.}*

Table 3.5 ITC measurements of talin-1 FERM domain binding to the β3 CT attached to large unilamellar phospholipid vesicles (LUVs).

The talin-1 FERM domain was titrated into LUV suspensions containing 5 µM immobilized β3 CT (Figures 3.8 and 3.9). All experiments were performed at 20ºC in 25 mM MOPS pH 6.8 with 100 mM NaCl and background heats of dilution were subtracted. Titrations were fit to one-site binding isotherms. *{Titration into β3 on 1% PtdIns(4,5)P_2 was performed as three independent experiments and errors are reported as standard deviations. Titration into β3 on 20% PS and 20% PS with 1% PtdIns(4,5)P_2 was performed once with each sample and the error is reported as the fitting error. All experiments were performed by DTM.}*

	K_a (x10^6 M^{-1})	K_d (μM)	ΔH(kcal/mol)	ΔS(cal/mol/K)	n
β3-1%PtdIns(4,5)P_2	1.19 ± 0.21	0.86	-25.0 ± 1.5	-55.8	0.80 ± 0.04
β3-20% PS	0.29 ± 0.02	3.4	-32.3 ± 0.9	-83.3	0.8 (held)
β3-20%PS + 1%PtdIns(4,5)P_2	0.61 ± 0.11	1.6	-34.0 ± 2.8	-87.5	0.95 ± .06

III. Discussion

Here we found that presentation of the β3 CT in the context of an acidic bilayer enhances its affinity for the talin-1 FERM domain up to three orders of magnitude, depending on the phospholipid composition of the bilayer. However, FERM domain binding to the β3 CT contrasts with the stronger interaction of the FERM domain with PIP5K1γ and with the interaction of the talin-2 FERM domain and the β1D CT. Small changes in integrin β CT sequences have been shown to significantly increase their affinities for talin family FERM domains (112). This suggests that the interaction between the talin-1 FERM domain and the β3 CT has been evolutionarily tuned to be intrinsically weak, allowing it to be modulated by changes in phospholipid composition, post-translational modifications, and additional protein-protein interactions.

To understand how these protein-protein and lipid-protein interactions modulate affinity, it is important to consider the various

energetic components associated with the interaction of the talin-1 FERM domain and the β3 CT with lipids, as well as their interaction with each other. Previous studies reported the interaction of the talin-1 FERM domain and the β3 CT with micelles and phospholipid vesicles (1, 16, 38, 54, 106). Here, we studied this interaction using the β3 CT tethered to phospholipid bilayers to understand the energetics of the overall process. Previously, we used this construct to study the dynamics of the β3 CT in the presence of bilayers by hydrogen-deuterium exchange (HDX). Although the construct lacks a transmembrane domain, it was designed computationally to attach via a residue predicted to be at the membrane interface and it contains all of the β3 residues necessary for interaction with talin-1. While it is possible that the TM domain could affect this interaction, our NMR and HDX studies indicate that the TM helix is broken by a kink as it exits the membrane, implying that the structure of the β3 CT distal to the helix disruption is unlikely to depend on residues buried within the membrane. Furthermore, our construct contains all of the β3 residues necessary for formation of the kink (Figure 2.5).

We can consider the overall free energy for the interactions of the bilayer-tethered β3 CT ($RT\ln(K_{obs}) = \Delta G_{overall}$) in terms of several components according to Eq. 1 below. It should be noted that this thermodynamic decomposition is path-independent and does not require kinetic ordering; nevertheless, all interactions here were rapid, on the

80

second to msec time scale, indicating that they might rapidly interconvert on a physiologically relevant time scale.

Eq. 1: $\Delta G_{overall} = \Delta G_{talin-bilayer} + \Delta G_{talin-peptide} + \Delta G_{reorganization}$

where:

$\Delta G_{talin-bilayer}$ is the energy associated with talin-1 head interaction with lipid, as determined directly from the titration of the FERM domains into lipid bilayers;

$\Delta G_{talin-peptide}$ is the energy associated with talin-1 head interaction with the β3 CT, as determined directly from the NMR or the fluorescent titrations reported above and which is sequence-specific (112) but only weakly favorable (K_{diss} on the order of 0.2 to 0.6 mM).

$\Delta G_{reorganization}$ is the free energy required to rearrange the conformations of isolated individual components and binary complexes to allow formation of a ternary complex.

The electrostatic surfaces of F3, F2F3, and the full FERM domain (44, 104) suggest that F2F3 binds negatively-charged bilayers in a manner highly conducive to forming a simultaneous interaction with the β3 CT; this finding has been supported by detailed coarse-grained molecular dynamics calculations (106). Thus, there is likely little reorganization energy associated with the interaction of these subdomains with bilayers.

By contrast, the β3 CT, tethered to a bilayer, is in a rapid equilibrium that favors a conformation in which the peptide interacts with the membrane in a way that masks residues important for talin-1 binding and that would otherwise be located 10 – 30 Å into the cytoplasm (1). A second minor conformation is more exposed to the aqueous surroundings, presumably allowing rapid kinetic access to the FERM domain. Hydrogen-deuterium exchange showed that the equilibrium favors the membrane-associated state by 100 to 1000-fold relative to the exposed state (Chapter 2), decreasing the overall affinity for binding cytosolic proteins by an equivalent amount. Thus, we expect that $\Delta G_{rearrange}$ would be dominated by the rearrangement of the β3 CT within the bilayer.

Consideration of Eq. 1 shows that cytosolic protein binding to the β3 CT in a proper context depends on an energetic balance, which, in this case, includes a highly favorable interaction between talin-1 and the membrane. A modestly favorable free energy of interaction of the β3 CT with the talin-1 head is balanced by a modestly unfavorable free energy of rearrangement of the β3 CT within the bilayer. In net, the observed affinity for formation of the ternary complex remains similar to that for the binary interaction of the talin-1 head with acidic bilayers. Likewise, in the absence of integrin, the binary complex between the FERM domain and the membrane appears to energetically favor the F2F3 subunit, as F0F1 does not affect the overall affinity or stoichiometry of the interaction. This suggests that F0F1 might not interact favorably with the bilayer once it is

tethered in place by the more stable F2F3 interaction. Alternatively, F0F1 might interact extensively when the FERM domain binds, but only after an energetically uphill conformational change that attenuates the overall affinity gain associated with F0F1-bilayer interaction. It is likely not accidental that the binary and ternary complexes are not optimized for cooperativity. Rather they appear to be tuned to be readily regulated by changes in the lipid environment and by post-translational modifications.

In summary, our studies reveal the rich interplay between structure, dynamics, kinetics, and thermodynamics that govern formation of the ternary complex between the $\beta3$ CT, phospholipid bilayers, and talin-1 FERM domain. This energetic dissection provides the basis for understanding how posttranslational modifications and changes in lipid composition might affect such processes. The situation becomes more complex as interactions with additional domains in integrin and talin, as well as other antagonistic or synergistic cytoplasmic proteins, are considered. Nevertheless, the present study illustrates the importance of considering the role of conformational changes, structural rearrangements, and conformational entropy in these processes, and provides a general approach to energetic decomposition that can form the basis for understanding regulation of even more complex systems.

IV. Methods

Design of recombinant talin-1, β3 CT and PIP5K1γ constructs. Talin-1, β3 CT, and PIP5K1γ constructs were cloned between the NdeI and XhoI restriction sites of the vector pet28a and contained an N-terminal 6xHis tag for purification, followed by a thrombin cleavage site for affinity tag removal. The talin-1 constructs (Figure 3.2, A-C) consisted of the entire talin-1 FERM domain (F0-F3), extending from its N-terminus through residue Ser425, the F0F1 subdomains extending from the N-terminus through residue Asp201, and the F2F3 subdomains spanning residues Ser206 through Ser425.

The β3 CT construct (Figure 3.2D), encompassing residues Thr720 through the C-terminus at Thr762, was previously described (1). For the current experiments, residue Ile719 was replaced with Cys to enable the construct to be immobilized on the surface of bilayers or to be labeled via maleimide chemistry. A peptide corresponding to residues 646-654 of PIP5K1γ was also labeled with fluorescein isothiocyanate (FITC) (Figure 3.2E).

Talin-1 and PIP5K1γ were introduced into BL21-DE3 cells (Novagen) and expressed for 20 h at 20°C in the presence of 0.5 mM IPTG. Cells were then lysed by sonication on ice in 20 mM imidazole buffer, pH 7.0, containing 500 mM NaCl, 1 mM EDTA, and a protease inhibitor cocktail (Sigma-Aldrich). After the lysates were cleared by

centrifugation, the supernatants were loaded onto HiTrap Ni-NTA columns (GE Healthcare) and peptides were eluted using an imidazole gradient. Imidazole was dialyzed away overnight into 50 mM Tris buffer, pH 7.5 containing 100 mM NaCl and the 6xHis tag was removed using thrombin. The constructs were then purified by SP ion exchange chromatography (GE Healthcare) and finally size exclusion chromatography with a Superdex 75 preparative column (GE Healthcare).

Preparation of large unilamellar vesicles (LUVs). LUVs were generated by evaporating a mixture of 1-palmitoyl-2-oleoyl-*sn*-glycero-3-phosphocholine (POPC, Avanti Polar Lipids) and 1-palmitoyl-2-oleoyl-*sn*-glycero-3-phospho-L serine (POPS, Avanti Polar Lipids) dissolved were dissolved in chloroform under nitrogen; excess chloroform was removed under high vacuum overnight. Phosphoinositides (Cell Signaling) were dissolved in $CHCl_3$/MeOH/0.1% HCl, mixed with POPC, and dried under nitrogen. Evaporated lipids were then re-suspended in buffer, vortexed vigorously for 5 minutes, subjected to 3 x freeze- thaw cycles, and extruded 20 to 30 times using 100 nm diameter filters (Avanti Polar Lipids).

Preparation of membrane tethered β3. Lyophilized β3 CT was re-dissolved in bilayer conjugation buffer (25mM sodium phosphate or MOPS, 100 mM NaCl, pH 6.8) at a concentration of 50 μM. Large unilamelar vesicles (LUVs) were generated by evaporating a mixture of

1,2-dipalmitoyl-*sn*-glycero-3-phosphoethanolamine-N-[4-(p-maleimidomethyl)cyclohexane-carboxamide] (16:0 PE MCC, Avanti Polar Lipids), 1-palmitoyl-2-oleoyl-*sn*-glycero-3-phosphocholine (POPC, Avanti Polar Lipids), and the appropriate negatively charged lipid under nitrogen. The lipids re-suspended in the bilayer conjugation buffer. LUVs were prepared by extruding 20 times through a 0.1 µm filter (Avanti Polar Lipids). β3 CT was reacted with 4 fold molar excess 16:0 10 PE MCC. The conjugation reaction was performed at pH 6.8 to minimize lysine amine-maleimide side reactions which are strongly disfavored at below pH 7. After reacting the β3 CT with the surface of the membrane for three hours, the bilayers were quenched with excess β-mercaptoethanol and dialyzed overnight. The final lipid concentration was calibrated using a POPC standard to calculate the amount of POPC in the β3-conjugated bilayer.

Isothermal titration calorimetry (ITC). ITC experiments were performed on a MicroCa ITC200 (MicroCal/GE). Samples were prepared in degassed 25 mM 3-(N-morpholino)propanesulfonic acid (MOPS) buffer, pH 6.8, containing 100 mM NaCl. Samples were loaded into cells after vigorous washing with buffer and syringes were loaded with 50 µL of titrant. Each experiment consisted of 20 x 2.0 µL injections spaced at intervals of 2-5 minutes. A 0.2 µL injection preceded all experiments and was not included in fitting. Fitting was performed using the Origin software suite (MicroCal/Origin Systems) as single binding events. Heats of dilution

were calculated by titration into the prepared diazylate and subtracted prior to fitting.

Surface plasmon resonance (SPR). All SPR experiments were performed on a Biacore 3000 (GE Healthcare). Each injection was done in triplicate. Kinetic experiments were performed in degassed 10 mM (4-(2-hydroxyethyl)piperazine-1-ethanesulfonic acid (HEPES) buffer, pH 7.2, containing 100 mM NaCl. The CM5 chip was activated using an amine coupling kit (GE Healthcare). N-(2-Aminoethyl)maleimide (pH 7.0) was then injected and non-reacted activated groups were capped with 1 M ethanolamine (pH 7.0). The $\beta3$ CT was immobilized onto the CM5 chip via maleimide crosslinking to $\approx$ 600 RU. Background maleimide was quenched with 2-☐mercaptoethanol. Talin-1 FERM domain constructs were injected at 50 μL/min with a 2 min injection time and 400 sec dissociation time. Binding data were fit to a double exponential using the BIAvaluation software.

For steady-state experiments, 100 nm LUVs were loaded onto an L1 chip. Talin-1 FERM domain constructs were injected for 10 min with a 120 sec dissociation time and a 10 μL/min flow rate. Between injections, new lipid surfaces were generated when full dissociation was not observed. Steady state construct binding was compared to a reference channel containing 100% POPC. Binding was fit to a single component isotherm equation: R_{eq} = (KA * [analyte]*RU_{max})/ (KA *[analyte]*n+1)+background.

Fluorescence Polarization (FP). FP experiments were performed as previously described (121). Briefly, FP was conducted in an ATF105 spectrofluorometer (Aviv Instrument, Inc) using a 0.3 cm path length cuvette. Spectra were measured using 1.0 nm slit widths at 25°C. The β3 CT was labeled with maleimide-BODIPY-TMR at a cysteine introduced at residue 719. Talin-1 F0-F3 was titrated into 20 nM β3 BODIPY-TMR and FP was measured at 575 nm after excitation at 530 nm. When F0-F3 was titrated into 20 nM FITC-labeled PIP5KI-γ, a dissociation constant and baseline parameters were derived from the fluorescence anisotropy signal/concentration isotherm using previously described methods (121).

Chapter 4 Transmembrane communication: general principles and lessons integrins and other receptors.

I. Introduction

In this review we explore how the binding of ligands to proteins induces functional conformational changes. Ligand induced conformational changes are fundamental to every aspect of protein function; for example, when an enzyme binds its substrate the act of binding induces changes in the protein's structure and dynamics to improve catalysis (122-124). Thus, it is often difficult to separate binding from catalysis. Similarly, binding of an allosteric ligand can lead to the propagation of conformational changes over long distances. We focus primarily on the generation and transmission of conformational changes in membrane proteins; we first introduce the types and limits of coupled, ligand induced conformational changes. Next we examine in quantitative terms the effects of different coupling mechanisms.

We then explore how ligand-binding affects the structures and functions of various membrane protein including bacterial histidine kinases and integrins, exploring the mechanisms by which multiple proteins, small molecules, metal ions, phospholipids, and post-translational modifications influence their activation and signaling. Finally, we demonstrate how interdomain coupling can generate diverse integrin signals.

II. Results

The coupling of ligand binding and environmental effects to conformational changes

Ligand binding generally leads to changes in both structure and dynamics, with increases and decreases in dynamics often occurring at different sites of the same protein(125). The effect of ligand binding on protein activity can be viewed in light of classical thermodynamic concepts of allostery, induced fit or conformational selection, and cooperativity(122-127). For simplicity, we consider a two-state transition between an active and resting state. The experimentally observed change in activity depends on several factors including: 1) the free energy difference or "energy gap" between the active and resting states, which determines the fraction of the protein in the activated state in the absence of the ligand, 2) the affinity of the protein for the ligand and their concentrations, and 3) the ability of the ligand to induce a transition when fully bound. Less than complete activation occurs, even when the ligand is fully bound, if it binds to both the activated and the resting conformations; in this case, the extent of activation relates to the relative affinity of the ligand for the activated versus resting state. These concepts of coupled equilibria are well studied and understood. Relating these to such phenomena as partial activation, potentiation, and synergistic ligands, is a simple matter of algebraic book-keeping, as shown in later sections.

In the next section, we explore in more quantitative terms how these simple binding phenomena lead to a variety of activation curves, when there are multiple ligands capable of activating the protein of interest. In this case, distinct ligand-binding sites at different locations can "couple" to give a variety of outcomes; the binding of one can alter the affinity of the other for the protein, and they can have additive or non-additive effects on the degree of maximal activation upon ligand saturation.

The coupling of binding and functional transitions refers to the phenomenon by which the binding of a ligand to one site influences the structure, dynamics, and binding affinity at a second site, which relates to the protein's energy gap and the ratio of affinities of the regulatory ligand for the activated versus the resting states. Given these simple requirements, it is not surprising that coupling can be achieved in different ways. One special case is when the binding of a ligand induces a change in association state. When no change in association is observed, it is often implicitly assumed that signaling occurs via "hard connections" in which helices shift, tilt or change register, mechanically driving a conformational change that propagates across a bilayer. A second model involves communication between subunits, which can involve large-scale or subtle changes in interactions between domains or between domains connected by flexible linkers. These different modes of communication can lead to different outcomes, when one measures the effects of mutations at

positions between the binding sites. For example, if a domain shifts as a rigid body, the search for a "pathway" from one location to the other might give rise to different results than if the transition of structural and dynamic information occurs by correlated motions of sidechains that propagate in a two-state manner between the two sites.

Finally, both the magnitude as well as the sign of the energy gap of a transmembrane (TM) protein depends on the membrane environment. Any shift in structure that changes the exposure of specific residues or the width (cross-sectional surface area) of a protein at a given position in the membrane will make the energy gap sensitive to the physical properties of the bilayer. Hence, mechanosensitive channels switch on in response to changes in bilayer tension(128). Potassium channels respond to the transmembrane electrical potential, and the location and coupling of cytoplasmic loops and helices changes in response to the fraction of IP lipids, sphingomyelin, and cholesterol in the bilayer(129-132). Indeed, the hydrophobic length of transmembrane helices is reflected in the width of the bilayers in the organelles to which they localize. Additionally, once located in a given membrane, there is tight coupling between the lipid environment and the conformation of the protein, as it, for example, partitions into cholesterol/sphingomyelin rich phases(133, 134).

Simple models for energetic coupling

Energy gap It is convenient to think of functional proteins as having at least two thermodynamic states – a resting state and an active state. The free-energy gap between these, $\Delta G_{gap} = G_{active} - G_{inactive}$ determines the equilibrium fraction of active protein as $f_{active} = \dfrac{1}{\left[1 + \exp\left(\Delta G_{gap}/RT\right)\right]}$. Since the largest possible fraction of the protein in the active state is 1, this also determines the maximal attainable degree of activation due to binding of any ligand or perturbation, via $A = 1 + \exp\left(\Delta G_{gap}/RT\right)$. For example, if ΔG_{gap} is 0.41 kcal/mol, then at room temperature the fraction activation is $1/3$. Therefore, even the best activating agent can only result in a 3-fold increase in activity. However, if ΔG_{gap} is 6.82 kcal/mol, the maximal degree of activation is 10^5.

A ligand causes activation when it binds with higher affinity to the active relative to the inactive state (see Figure 4.1A/B). If K_A and K_I are the dissociation constants for the ligand binding to the active and inactive states, respectively, then the ligand is activating if $K_A < K_I$. Moreover, the fraction K_I/K_A determines the activating potential of the ligand. When the system is saturated with ligand, the free energy difference between active and inactive states becomes: $\Delta G_{gap}^{eff} = -RT\ln\left(K_I/K_A\right) + \Delta G_{gap}$. For an ideal activating ligand, K_I approaches infinity, such that ligand saturation leads to complete activation, and the degree of activation is only limited by the

intrinsic ΔG_{gap}. If a ligand binds to both states, the maximum degree of

activation is $A = \left(K_I / K_A \right) \cdot \dfrac{1 + e^{-\Delta G_{gap}/RT}}{1 + \left(K_I / K_A \right) \cdot e^{-\Delta G_{gap}/RT}}$, and is limited by both the

intrinsic ΔG_{gap} and the ratio of equilibrium binding constants K_I / K_A (see

Figure 4.1B). For a given protein (and a fixed ΔG_{gap}), this ratio of

equilibrium binding constants could differ for different ligands, leading to

varying degrees of activation upon ligand saturation. The specifics of a

biological process determine how large ΔG_{gap} needs to be and how it is

modulated by binding. Large ΔG_{gap} and K_I / K_A lead to a high degree of

maximal activation (Figure 4.1B). A large ΔG_{gap} is also useful in situations

with multiple effectors that act in a combinatorial manner.

Environment ΔG_{gap} can be modulated by environmental variables, such as

the membrane composition. While it may be possible to treat membrane

effects as ensembles of binding sites, we treat them as environmental

factors modulating ΔG_{gap} in the simplest case.

Coupling Once the receptor ectodomain shifts into its active state, this

information is transmitted onto the functional cytoplasmic end of the

molecule. This is sometimes referred to as allostery and is equivalent to

stating that one end of the molecule is thermodynamically coupled to the

other. This coupling depends on the specifics of the molecule's structure and dynamics, but can be thought of as arising from differences in inter-domain interaction free energies when in different states. This inter-domain coupling or allostery can therefore be captured with a thermodynamic coupling free energy parameter, $\Delta\Delta G_c$, which determines the extent to which the different domains experience each other's states.

Simple Model 1. A two-state extracellular receptor domain, with an energy gap ΔG_{gap}^R, receives input from a signaling ligand, which binds preferentially to the active state of the receptor (Figure 4.1C). The receptor domain is thermodynamically coupled, via the coupling parameter $\Delta\Delta G_c^R$, to the cytoplasmic domain, which carries out the function of the system in its active state. The intrinsic activity of the cytoplasmic domain is controlled by its own energy gap, ΔG_{gap}^C. Figure 4.1D shows how the activity profile of this system (e.g. level of activation as a function of ligand concentration) depends on ΔG_{gap}^C and $\Delta\Delta G_c^R$. Because the function of the overall system is based on the activity of the cytoplasmic domain, high values of its gap lead to low levels of background activity, thus more switch-like behavior (compare profiles at low and high ΔG_{gap}^C in Figure 4.1C). However, because the two domains are coupled, the energy gap of the receptor domain also influences the level of activation. In fact, the

95

energy gaps of the two domains can be thought of as jointly modulating

the overall effective energy gap of the system, as shown in Figure 4.1C.
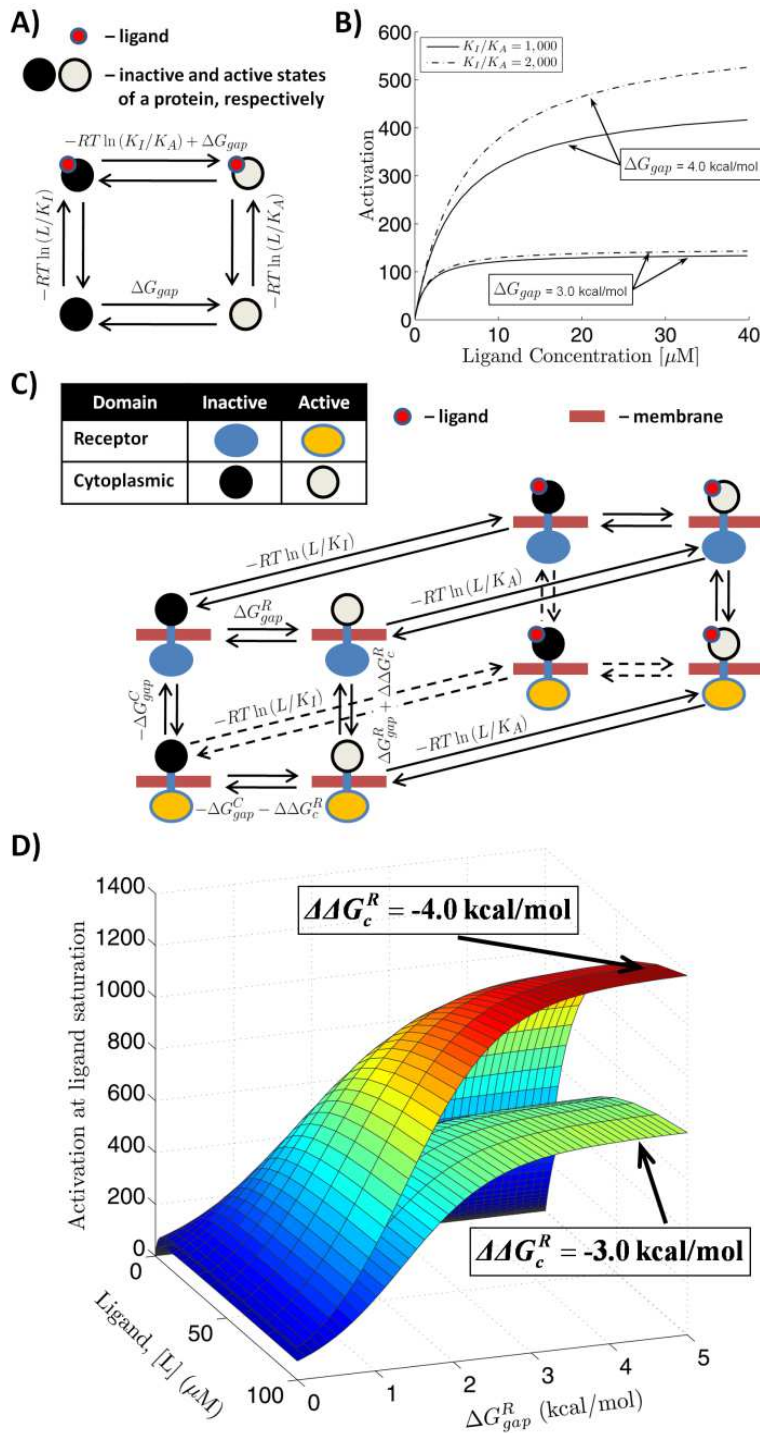
Figure 4.1 Simple linked-equilibria models.

(A) A thermodynamic cycle illustrating the coupling between activation of a two-state protein and ligand binding. (B) Activation profiles of a two-state protein as a function of an agonist ligand concentration. Ratio of dissociation constants for the inactive and active states, K_I/K_A, and the intrinsic energy gap, ΔG_{gap}, determine maximal attainable activation. (C) A diagram of a simple signal-transduction molecule. Two domains, a receptor domain and a cytoplasmic functional domain, each with two states, are thermodynamically coupled, with the receptor modulated by an activating ligand. All eight states of the system are explicitly shown and the indicated equilibrium free energy differences correspond to the direction of the arrow with which they are shown. Free energy differences between ligand-bound states (back side of the cube) are omitted for simplicity, but follow simply from thermodynamic cycles. L indicates the concentration of the cytoplasmic ligand. (D) Activation profiles of the system in (C) as a function of the energy gap of the cytoplasmic domain, ΔG_{gap}^C, and coupling of the receptor to the cytoplasmic domain, ΔG_c^R. K_A and K_I are set to 10 nM and 20 μM, respectively, and the energy gap of the receptor domain, ΔG_{gap}^R, is set to 3.0 kcal/mol. The effective energy gap for this system can be shown to be

$$\Delta G_{gap}^{eff} = \Delta G_{gap}^C + RT \ln\left(\frac{e^{\left(\Delta G_{gap}^R - \Delta\Delta G_c^R\right)/RT}\left(1 + L/K_I\right) + \left(1 + L/K_A\right)}{e^{\left(\Delta G_{gap}^R + \Delta\Delta G_c^R\right)/RT}\left(1 + L/K_I\right) + \left(1 + L/K_A\right)} \right) - \Delta\Delta G_c^R.$$ Thus, if

$\Delta\Delta G_c^R$ is zero (i.e. there is no coupling between the domain), the overall gap is just ΔG_{gap}^C, but as long as $\Delta\Delta G_c^R$ is negative (i.e. activation of the receptor promotes the active state of the functional domain), higher values of ΔG_{gap}^R contribute to a higher overall energy gap. Similarly, tighter coupling (lower $\Delta\Delta G_c^R$), leads to a higher overall gap larger degree of maximal activation.

Simple Model 2 If the TM domain has active and inactive states, the system has 16 total states (Figure 4.2A), and the activation profile depends on the energy gap of the TM domain and its coupling to the cytoplasmic domain. Whereas larger energy gaps of the cytoplasmic domain always lead to larger overall energy gaps of the system (i.e. larger degree of maximal activation), this is not necessarily the case for the energy gap of the TM domain (see Figure 4.2B), and the effect of

increasing ΔG_{gap}^{TM} can go in either direction, depending on the other parameters. Intuitively, this is because unlike ΔG_{gap}^{C}, ΔG_{gap}^{TM} does not directly modulate the activity of the functional cytoplasmic domain, but rather does so through thermodynamic coupling. Increasing ΔG_{gap}^{TM} leads to lowering of the absolute active fraction of the cytoplasmic domain, by virtue of the two domains being coupled. This serves to silence background activity in the resting state, while in the presence of activating ligand it limits the maximal fraction of active protein. The overall consequence depends on which of these two effects dominates. Because the TM domain lowers activity at resting state, it may provide higher levels of activation compared to a system without a two-state TM domain (Figure 4.2B). This illustrates the advantage of having multiple loosely-coupled domains – it allows for strong switching behavior without resorting to large energy barriers between active and inactive states. Intermediate domains also provide additional opportunities for modulation of the signal. Additional environmental conditions, such as the state of the membrane or the presence of specific ligands, can be integrated into the final output of the signaling system.
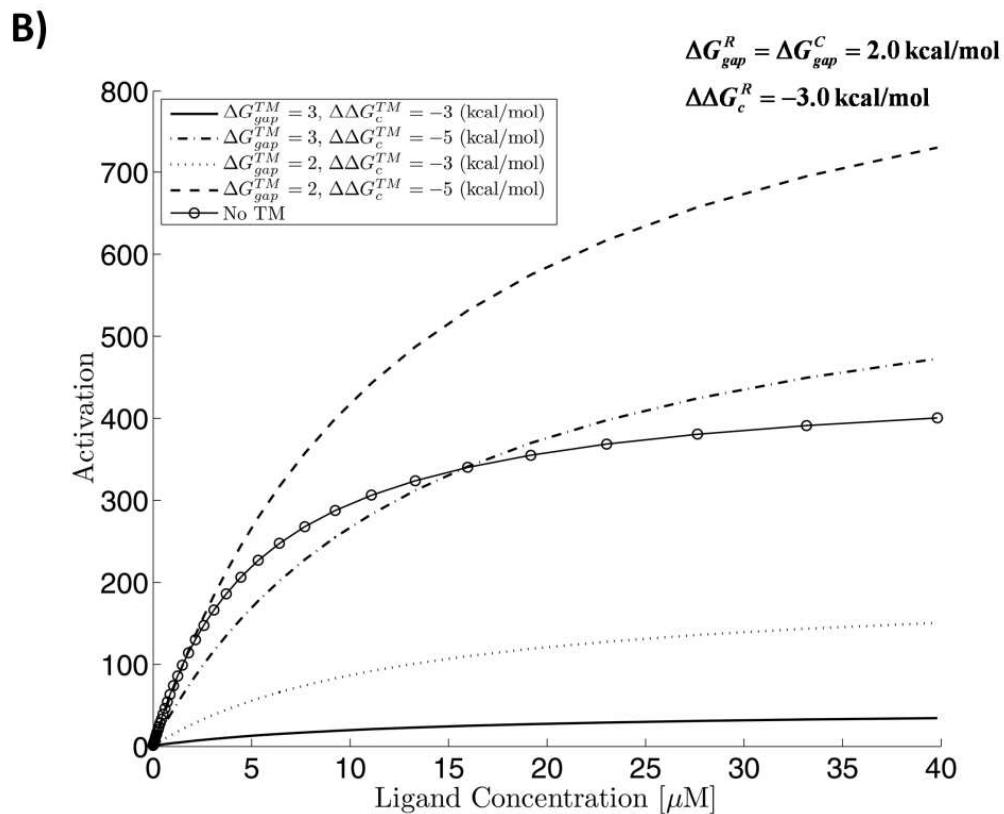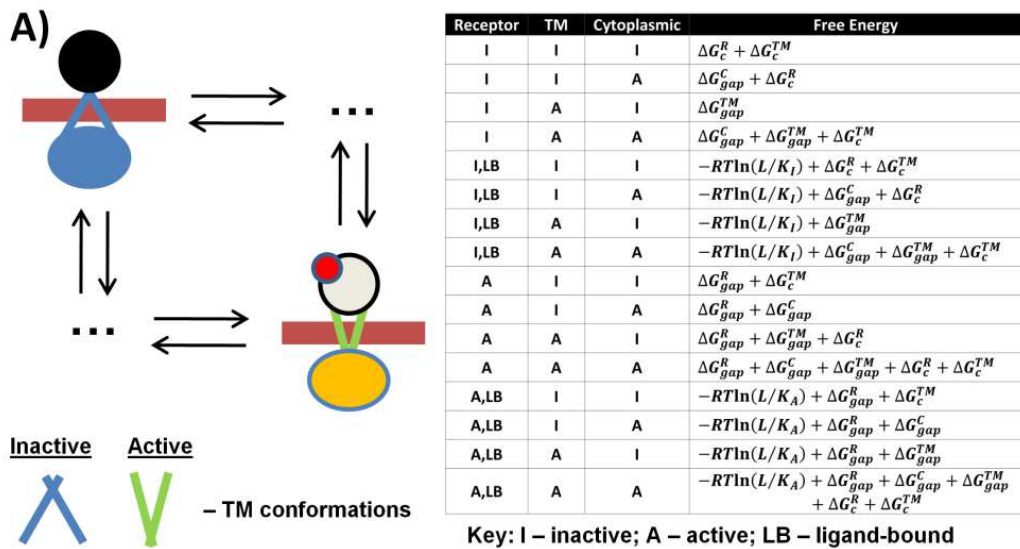
Figure 4.2 A more complex model of a signaling molecule.

(A) In addition to the receptor and functional cytoplasmic domains as in Figure 4.1, here the TM domain is explicitly modeled as having two states. The intrinsic fraction of TM domain in the active state is defined by ΔG_{gap}^{TM}, and it is coupled to the cytoplasmic domain via ΔG_c^{TM}. The sixteen states

99

of the system along with the corresponding free energies are shown in the table on the right. (B) The dependence of activation profiles on ΔG_{gap}^{TM} and ΔG_c^{TM}. K_A and K_I are set to 10 nM and 20 μM, respectively, and values of other parameters are shown. The line with circles demonstrates the case where no two-state TM domain is present, and the receptor domain couples directly to the cytoplasmic domain with the same ΔG_{gap}^{R} as in other models.

Simple Model 3 Extracellular and intracellular signals can be integrated

by the same receptor. The VirA/VirG two-component system from

Agrobacterium tumefaciens integrates multiple inputs with both its

extracellular and cytoplasmic domains, including plant phenolic signaling

molecules, monosaccharides, and pH(135). This can be modeled with the

addition of a two-state cytoplasmic linker domain (Figure 4.3A). An

intracellular ligand, such as a phenolic molecule, binds stronger to the

activated state than the inactive one (ligand *C* in Figure 4.3A), whereas a

different ligand, such as a sugar, modulates the states of the receptor

domain (ligand *L* in Figure 4.3A). Both the maximal activation as well as

the concentration of half-maximal activity (IC50) change for one ligand in

response to different concentrations of the other (Figure 4.3B). Such

cumulative modulation of activity by both ligands effectively amounts to

signal integration. It can be used by the cell to perform certain actions only

in cases, for example, where both ligands are present at certain

concentrations. In this case, both ligands were chosen to bind more tightly

to the active states of their respective domains, but repressing signals can

also modulate receptor function.
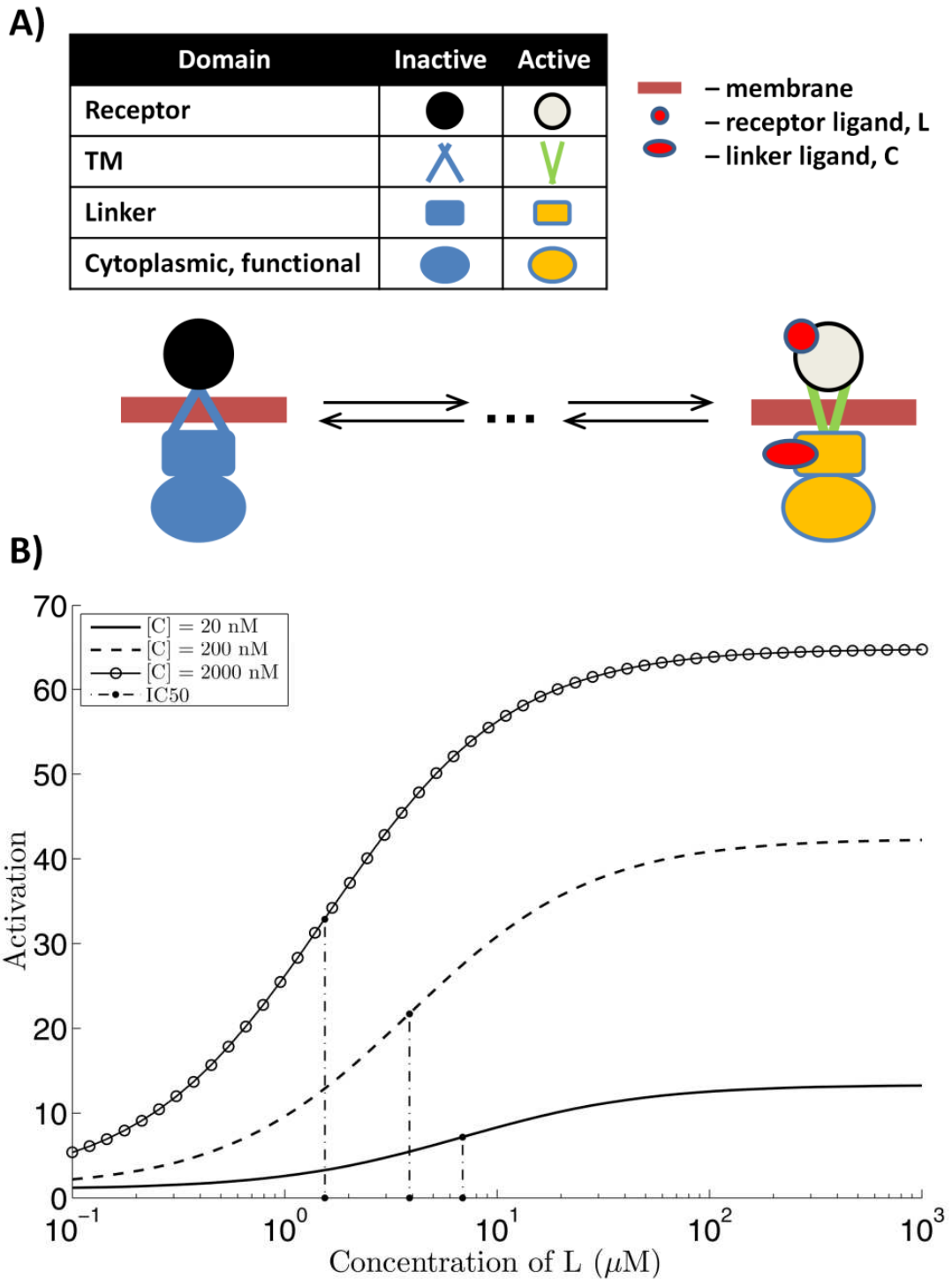
Figure 4.3 A realistic model of signal transduction, inspired by VirA protein of the VirA/VirG two-component system.

 (A) In addition to the domains and states in the model presented in Figure 4.2, there is an additional cytoplasmic linker domain, with its own active

and inactive states, which is modulated by the signaling ligand *C*, different from ligand *L* which modulates the receptor. The total number of states in this system is 64, and for clarity only the fully inactive and the fully active states are diagrammed. (B) Activation, relative to resting state, is plotted against increasing concentration of ligand *L*, in the presence of different concentrations of *C*. This illustrates the ability to integrate signals from multiple ligands. Though this model does not explicitly treat the receptor as being dimeric (as is the case for the VirA protein), it can be easily extended to do so. In this case, binding of ligand may or may not be coupled of receptor dimerization and there may exist cooperativity (negative or positive) between the two ligand-binding sites. Potential scenarios that can be explored include: 1) binding of a single ligand may push the system towards the active state, whereas binding two ligands symmetrically may favor the inactive state 2) alternatively, the receptor may signal only when two ligands are bound, or 3) binding of the second ligand may proceed independently of the first one.

Inside-to-Outside Coupling in Integrins Receptors

Integrins are $\alpha-\beta$ heterodimeric adhesion receptors that mediate interactions between the extracellular environment and the intracellular cytoskeleton (6, 95, 136-138) and demonstrate how bidirectional transmembrane signal transduction is fine-tuned by multiple coupled equilibria in the extracellular, transmembrane, and cytosolic domains (Figure 4.4A). Integrin ectodomains contain a large globular N-terminal ligand binding "head" and distinct C-terminal α and β "legs" that cross the plasma membrane as single TM domains and terminate in short cytoplasmic domains that bind intracellular molecules. The inactive integrin adopts a bent conformation placing the head in proximity to the membrane and the distal legs. Upon activation, an extended conformation is favored and the α and β legs, TM, and cytoplasmic domains separate.
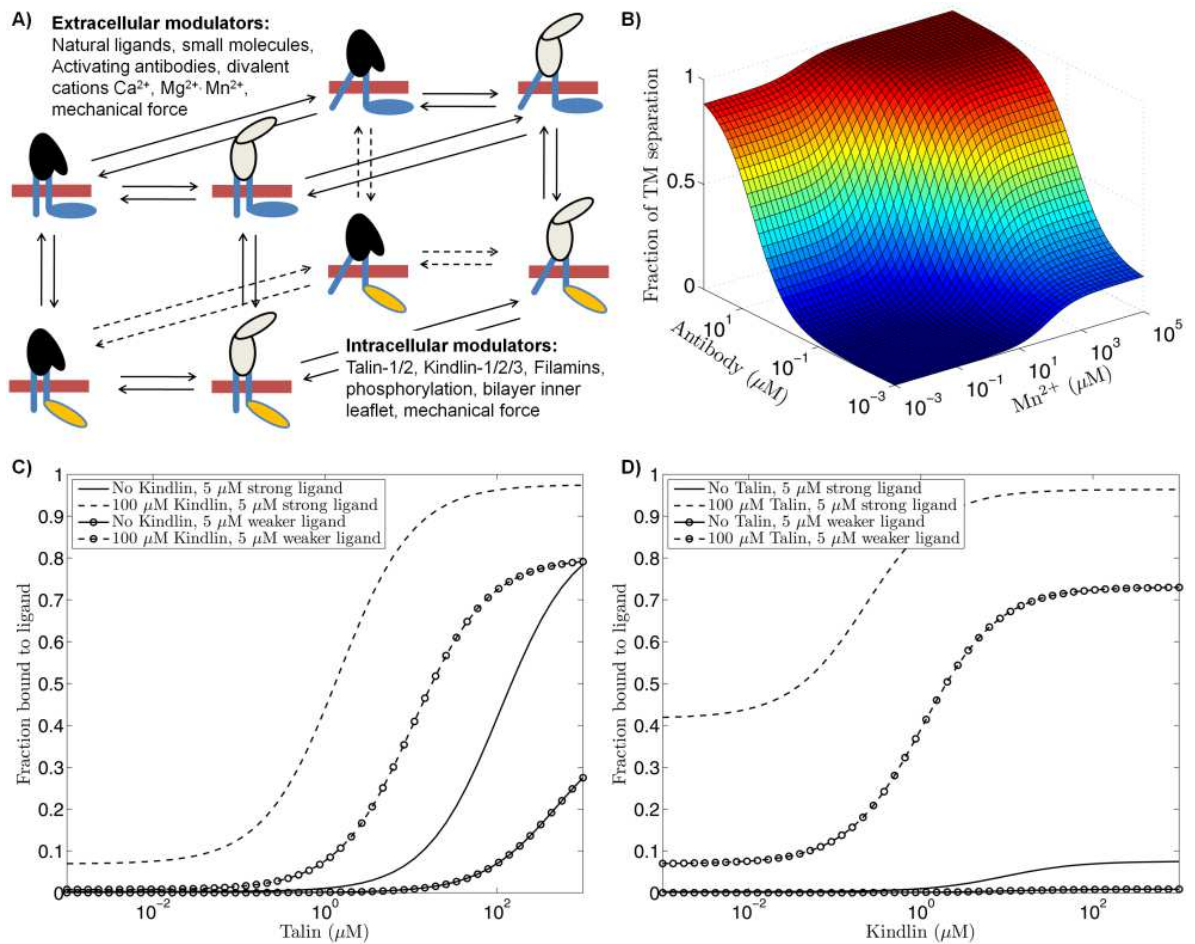
Figure 4.4 Thermodynamic model of integrin signaling.

(A) At the coarsest level, extracellular, TM, and intracellular domains of integrins can be thought as being either active or inactive, giving rise to eight coupled states as illustrated. The various effector molecules modulate integrin state by preferentially binding to select domain conformations. "Inside-out" signaling refers to modulation of the extracellular domain conformation via interactions between an integrin's cytosolic tails and intracellular signaling molecules. "Outside-in" events sometimes refer to the activation of oligomerization dependent signaling pathways subsequent to binding polyvalent ligands. However, keeping with our model, here it will refer to the ability of extracellular ligands to affect the conformation and function of intracellular domains. (B) Using reasonable values for the energy gaps and coupling constants associated with these states as well as equilibrium binding constants for the active and inactive states of different effector molecules, one can interrogate the thermodynamics of integrin signaling in a coarse, semi-approximate manner. Shown here is the level of integrin activation (separation of TM/tail regions) in response to increasing amounts of an activating

103

antibody, as a function of Mn^{2+} concentration. This illustrates outside-in signaling. (C) AND (D) Inside-out signaling as illustrated by the fraction of extracellular domain bound to native ligand as a function of different amounts of active intracellular talin and kindlin. The binding affinity of the ligand as well as the amounts of talin/kindlin all couple to determining the activation state of the integrin.

Interactions between the α and β chain legs, TM, and membrane proximal cytosolic domains, stabilize the inactive integrin. Single point mutations result in receptor activation (15, 18, 139, 140) and membrane proximal ab☐disulfide cross-linking completely abrogates TM signal transduction in either direction (141, 142). While structural studies suggest that there is a distinct TM interface, the membrane proximal regions are dynamic (15, 16, 40, 142, 143), befitting the need for rapid signal transduction.

The "loose" dynamic interactions between the α and β chains near the membrane give way to an extensive interface between globular portions of the extracellular domain, which can be perturbed via mutagenesis (144). Thermodynamic coupling occurs throughout the globular ectodomain. Crystallization with and without ligand resulted in active-extended (145) and inactive-bent (146, 147) conformations respectively. Soaking the inactive crystals with a ligand resulted in only small-scale changes in the binding site without leg extension due to crystal contact constraints (148). Without such constraint, anti-integrin drugs can generate adverse side effects by activating the receptor and generating immune reactive epitopes or Ligand Induced Binding Sites (LIBS) in the

integrin legs (138). Small molecule drugs can also uncouple subdomains. Allosteric inhibitors that compete for inter-domain contacts generate functionally split integrins in which the head is locked into an inactive conformation, but distal regions generate active LIBS(149). LIBS antibodies also shift the integrin equilibrium to an active conformation. Constraining the integrin C-termini stabilizes the bent conformation and the inactive ligand binding site, but the addition of LIBS antibodies and Mn^{2+} (an second allosteric activator) shifts the head domain equilibrium to an active state despite the distal constraints(150). Demonstrating bidirectionallity, LIBS antibodies induce TM separation when not constrained(18). The combination of LIBS antibody and a second activator, Mn^{2+}, further increased activation, while Mn^{2+} alone did not significantly affect TM separation. Therefore, as in the case of VirA/VirG (Figure 4.3), multiple stimuli are integrated to produce different intracellular responses (modeled Figure 4.4B).
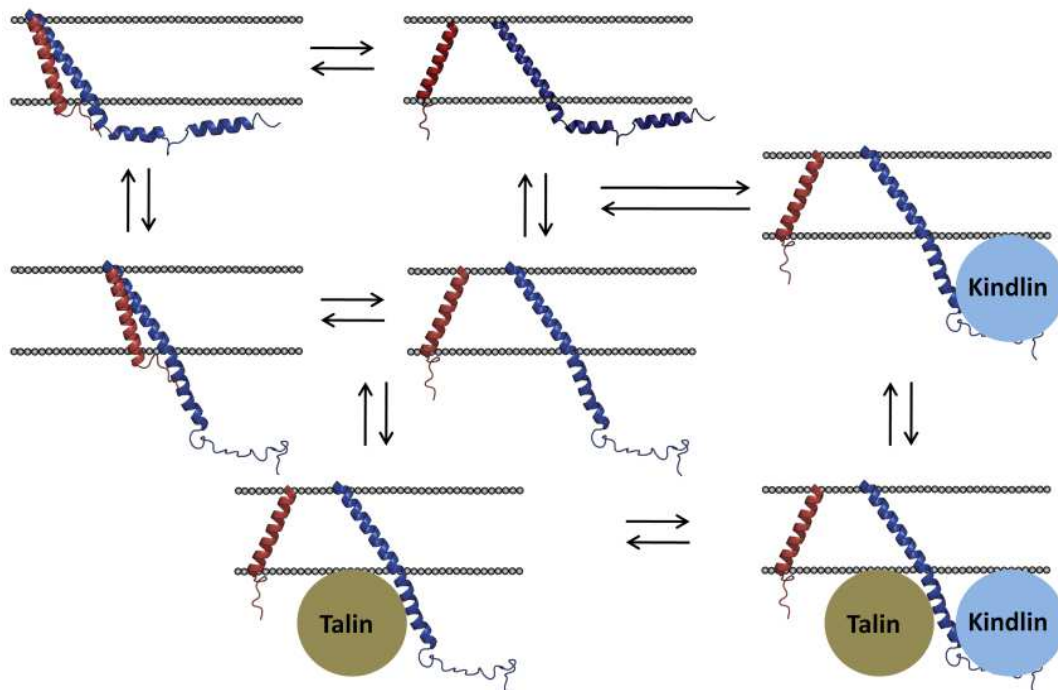
Figure 4.5 Coupled equilibria linking integrin TM interactions to cytosolic events.

Integrin αβ TM heterodimers (left) stabilize inactive ectodomain conformations and TM separation (right) stabilize active ectodomain conformations. The αβ heterodimer stabilizes interactions between the β-cytoplasmic domain and the inner leaflet of the bilayers (top). Cytosolic proteins talin-1 and kindlin-3 shift the equilibrium towards an active conformation by the stabilizing extended cytoplasmic domain and separated TM domains (bottom right).

While the integrin cytoplasmic domain is much shorter (~5-6 kD for β-integrins) than the ectodomain, it also integrates multiple signals to modulate extracellular function. There is convincing evidence of a defined αIIbβ3 TM interface, however, the membrane proximal and cytoplasmic domains have not provided consistent structures (15, 16, 38, 39, 54, 151). In Chapter 2, we describe the NMR structure and the dynamics of the αIIb and β3 membrane proximal domains (1). The αIIb cytoplasmic domain

was disordered, but caused a kink in β3 that was predicted to stabilize the interaction of two β3 cytoplasmic helices with the bilayer. Significantly, these dynamic membrane interacting helices contain the primary motifs that bind the evolutionarily related talin and kindlin families of proteins (reviewed in (20) and (19)). Figure 4.5 outlines a simple linked equilibrium model, which is quantitatively described in Figure 4.4C/D, for how coupling between talin and kindlin binding motifs allows differentiation between ligands with different affinities for the receptor, effectively recapitulating an intermediate affinity state without the need for distinct extracellular conformations (149, 150). This model is further elaborated upon below.

IV. Coupling between integrin and kindlin subdomains produces distinct integrin activation states.

Our model of αIIbβ3 describes the integrin as series of thermodynamically coupled subdomains (Figure 4.6A). Each has an intrinsic ΔG_{gap} and a coupling parameter $\Delta\Delta G_c$ that describes communication between subunits. The goal of this model is to demonstrate that the presence of multiple intracellular regulatory domains can result in a range of apparent extracellular affinity states that do not require distinct ectodomain conformations. The studies reviewed above

demonstrate that there is interdomain communication in the ectodomain that is coupled to the TM state. Our HDX results with model integrin cytoplasmic domains demonstrate that despite its short sequence, there is also communication between the TM and both the talin binding site and the distal kindlin site. This establishes a path of communication from the kindlin and talin sites to the ligand binding site.

A

Active ligand
binding site

Resting state

Intracellular
Extracellular
Events

α β

1     $\Delta\Delta G_{C,1/2}$

2     $\Delta\Delta G_{C,2/3}$

3     $\Delta\Delta G_{C,3/4}$

4

5   6

$\Delta\Delta G_{C,4/5}$

$\Delta\Delta G_{C,5/6}$
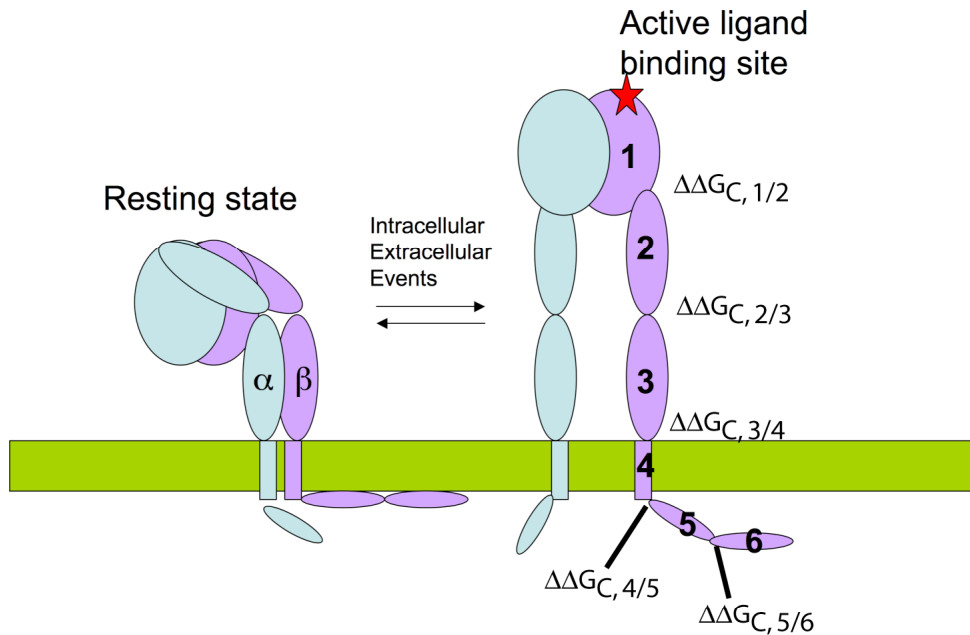
B

Domain	Conformation x	Occupancy =	# States
1) Ligand binding site	Active/Inactive	+/- Ligand	4
2) Metal binding site	Active/Inactive	+/- Mn^{2+}	4
3) Leg, LIBS antibody site	Active/Inactive	+/- LIBS antibody	4
4) Transmembrane domain	Active/Inactive		2
5) Cyto Helix 1	Active/Inactive	+/- Talin	4
6) Cyto Helix 2	Active/Inactive	+/- Kindlin	4

Figure 4.6 Simplified domain structure of αIIbβ3.

αIIbβ3 contains a series of thermodynamically coupled subdomains that bind allosteric regulators. (A) The β3 chain was modeled containing six subunits from the N-terminal ligand binding site (1) to the distal C-terminal

109

kindlin binding site (6). Each subunit an intrinsic equilibrium (ΔG_{gap}). Adjacent subunits are thermodynamically coupled ($\Delta\Delta G_C$). (B) With the exception of the TM, each subdomain recognizes a specific ligand that modulates the equilibrium between active and inactive conformations. In the case of sudomain (1), the natural ligand would be fibrinogen. Subdomain (2) includes the Mn^{2+} binding site (Mn^{2+} increases ligand fibrinogen to αIIbβ3). Subdomain (3) can bind LIBS antibodies. The combined active/inactive and ligand bound/ligand free states result in four states per domain. The TM does not have a ligand and therefore has only 2 states. Talin-1 and kindlin-3 ind regions (5) and (6) respectively.

As actual thermodynamic parameters for each subdomain are unknown, this model is mearly illustrative and intended to demonstrate the functional effects of communication between integrin subunits and not to make specific arguments as to their actual values. Thermodynamic parameters were chosen to conform to published data when possible and to fit with our experimental results. Without TM constraints, the integrin ectodomain equilibrium lies only slightly towards the inactive state (150) (152). Therefore a ΔG_{gap} of only 1 kcal/mol for each extracellular subdomain was used. We assumed that the coupling energy between subdomains was relatively high, lying between 3 kcal/mol and 6 kcal/mol. The ΔG_{gap} for the TM domain was chosen to be 3 kcal/mol as this site is the most sensitive to mutation and removal of the TM results in partial activation. Each subdomain can bind a ligand with different affinities for the active and inactive states. This ratio, K_I/K_A, which was held to 1000 i.e. activating ligands prefer the active conformation 1000 fold more than the inactive. Each subdomain can populate four states: 1) active without ligand; 2) active with ligand; 3) inactive without ligand; and 4) inactive with

ligand. The TM domain, does not have a ligand and populates only two states, active (separated) and inactive (heterodimeric) states. The affinity for talin-1 and kindlin-3 was assumed to be 100 nM, which is of the order of magnitude observed in our ITC experiments in Chapter 3.

Thermodynamic coupling between extracellular, TM, and cytoplasmic domains allows dynamic regulation of ligand binding.

With no allosteric modulator, fractional occupancy of αIIbβ3 is dependent on the intrinsic equilibrium of the receptor, ΔG_{gap} and $\Delta\Delta G_{c}$, affinity for the ligand, and the ligand concentration (Figure 4.7A). Any regulatory protein, such as talin-1, that binds preferentially to the active conformation of the cytosolic domain will shift the extracellular ligand binding curve to the left, increasing the apparent affinity of the receptor (comparing Figure 4.7A and 4.7B). Likewise, a negative regulator can stabilize the inactive conformation and shift the equilibrium to the right (comparing Figure 4.7A and 4.7C).

A

No allosteric regulator

Domain	ΔG_{gap} (kcal/mol)	$\Delta\Delta G_{C, N+1}$ (kcal/mol)	[Ligand] (μM)
1) Ligand binding site	1	6	variable
2) Metal binding site	1	6	0
3) Leg, LIBS antibody site	1	6	0
4) Transmembrane domain	3	6	0
5) Cyto Helix 1	2	2	0
6) Cyto Helix 2	1	NA	0

B

Binding of a an allosteric activator

Domain	ΔG_{gap} (kcal/mol)	$\Delta\Delta G_{C, N+1}$ (kcal/mol)	[Ligand] (μM)
1) Ligand binding site	1	6	variable
2) Metal binding site	1	6	0
3) Leg, LIBS antibody site	1	6	0
4) Transmembrane domain	3	6	0
5) Cyto Helix 1	2	2	10
6) Cyto Helix 2	1	NA	0

C

Binding of an allosteric inhibitor

Domain	ΔG_{gap} (kcal/mol)	$\Delta\Delta G_{C, N+1}$ (kcal/mol)	[Ligand] (μM)
1) Ligand binding site	1	6	variable
2) Metal binding site	1	6	0
3) Leg, LIBS antibody site	1	6	0
4) Transmembrane domain	3	6	0
5) Cyto Helix 1	2	2	10
6) Cyto Helix 2	1	NA	0

112

Figure 4.7 Binding of regulatory proteins to the integrin cytoplasmic tail affects receptor occupancy.

The fractional occupancy of a model integrin receptor was plotted as as a function of extracellular ligand concentration. Four different ligands were modeled (K_d = 10 nM, solid; 100 nM, dashed; 1 μM, solid ball; 10 μM, dashed ball). Thermodynamic parameters for integrin subdomains are displayed to the right. (A) Receptor occupancy without a regulatory protein. (B) Receptor occupancy in the presence of a distal activator such as talin (K_A = 100 nM, K_I = 100 μM). (C) Receptor occupancy in the presence of a distal inhibitor such as talin (K_A = 100 nM, K_I = 100 μM).

On the surface of platelets, αIIbβ3 is surrounded a high affinity ligand, fibrinogen, which has a serum concentration between 5 and 10 μM, well above its approximate K_d of 3-10 nM (153). Therefore, the intrinsic equilibrium of the receptor must favor the inactive state strongly to prevent spurious clotting and activation requires allosteric regulation via talin-1 and kindlin-3. In the absence of communication between the intracellular and extracellular domains ($\Delta\Delta G_c$ = 0), receptor occupancy is independent of the talin-1 concentration and depends only on the overall ΔG_{gap} of the ectodomain, the ligand concentration, and the ligand's affinity for the integrin (Figure 4.8A). Coupling through the TM results in ligand binding that is dependent on the concentration of active talin-1 (Figure 4.8B). There is minimal binding to even strong ligands (K_d = 10 nM) in the absence of talin-1, while receptor occupancy approaches 100% upon talin-1 activation. This produces switch-like behavior, in which the receptor up-regulates affinity for a given ligand in the presence of minimal background activity. Even weaker ligands, with affinities of 100 nM and 1 μM, have occupancies approaching 80% and 30%, respectively. If the

113

coupling energy is reduced from 6 kcal/mol to 3 kcal/mol, then dynamic range of the receptor decreases significantly. There would be 50% occupancy for a strong ligand (K_d = 10 nM) in the absence of talin and 90% occupancy at saturating concentrations of talin-1 (Figure 4.8C). A slightly weaker ligand with an affinity of 100 nM would have approximately 10% occupancy in the absence of talin-1 and 40% at saturating talin-1 concentrations. The 1 μM ligand would have neglible binding even at saturating talin-1 concentrations.

A

No coupling through TM

Fraction Occupancy vs [Talin] µM

Legend:
— 10 nM Kd ligand
- - - 100 nM Kd ligand
-○- 1 µM Kd ligand
-●- 10 µM Kd ligand

Domain	ΔG_{gap} (kcal/mol)	$\Delta\Delta G_{C,\,N+1}$ (kcal/mol)	[Ligand] (µM)
1) Ligand binding site	1	6	10
2) Metal binding site	1	6	0
3) Leg, LIBS antibody site	1	6	0
4) Transmembrane domain	3	0	0
5) Cyto Helix 1, Talin	2	2	variable
6) Cyto Helix 2, Kindlin	1	NA	0

B

Coupling through TM
6 kcal/mol coupling between domains

Fraction Occupancy vs [Talin] µM

Legend:
— 10 nM Kd ligand
- - - 100 nM Kd ligand
-●- 1 µM Kd ligand
-●- 10 µM Kd ligand

Domain	ΔG_{gap} (kcal/mol)	$\Delta\Delta G_{C,\,N+1}$ (kcal/mol)	[Ligand] (µM)
1) Ligand binding site	1	6	10
2) Metal binding site	1	6	0
3) Leg, LIBS antibody site	1	6	0
4) Transmembrane domain	3	6	0
5) Cyto Helix 1, Talin	2	2	variable
6) Cyto Helix 2, Kindlin	1	NA	0

C

Coupling through TM
3 kcal/mol coupling between domains

Fraction Occupancy vs [Talin] µM

Legend:
— 10 nM Kd ligand
- - - 100 nM Kd ligand
-●- 1 µM Kd ligand
-●- 10 µM Kd ligand

Domain	ΔG_{gap} (kcal/mol)	$\Delta\Delta G_{C,\,N+1}$ (kcal/mol)	[Ligand] (µM)
1) Ligand binding site	1	3	10
2) Metal binding site	1	3	0
3) Leg, LIBS antibody site	1	3	0
4) Transmembrane domain	3	3	0
5) Cyto Helix 1, Talin	2	2	variable
6) Cyto Helix 2, Kindlin	1	NA	0

115

Figure 4.8 Thermodynamic coupling between subdomains increases ligand binding dynamic range.

The fractional occupancy of a model integrin receptor as a function of talin-1 concentration in the presence of 10 μM extracellular ligand. Four different ligands were modeled (K_d = 10 nM, solid; 100 nM, dashed; 1 μM, solid ball; 10 μM, dashed ball). Thermodynamic parameters for integrin subdomains are displayed to the right. (A) Receptor occupancy without coupling through the TM. (B) Binding of ligands with affinities between 10 nM and 10 μM to the integrin with 6 kcal/mol coupling between subdomains as a function of talin-1 concentration. (C) Receptor occupancy with 3 kcal/mol coupling between subdomains as a function of talin-1 concentration.

Coupling between talin-1 and kindlin-3 produces distinct functional states.

The ability of cells to discriminate between different integrin ligands has been attributed to the existence of distinct conformations in the ectodomain (150, 154). However, this effect can also be produced by coupling between multiple regulatory domains. To demonstrate this, weak thermodynamic coupling was introduced between the talin-1 and kindlin-3 binding sites ($\Delta\Delta G_c$ = 2 kcal/mol). Binding of talin-1 (Figure 4.9A) or kindlin-3 (Figure 4.9B) to the integrin cytoplasmic tail results in distinct extracellular functional states. Kindlin-3 produces much lower ligand occupancy than talin-1, since its communication to the TM and the rest of the receptor is dampened by the ΔG_{gap} of the talin-binding site. Already, this produces two distinct extracellular states. The talin-only state has higher occupancy than the kindlin-only state. For example, in the presence of 100 μM talin, the integrin would bind the 10 nM and 100 nM

116

ligands with 90% and 50% occupancy, respectively (Figure 4.9A, black line). In contrast, the same concentration of kindlin-3 would produce only 10% and ~1% occupancy, respectively (Figure 4.9B, black line). Simultaneous binding of talin-1 and kindlin-3 to the integrin would produce further activation states. For each talin-1 concentration (white/grey/black bars) an increase in occupancy can be produced by the addition of kindlin-3 (Figure 4.9A and 4.9C).   For example, if a cell were to activate both talin-1 and kindlin-3, there would be 50% occupancy of a ligand with a 1 µM dissociation constant (Figure 4.9C, black line). By down regulating kindlin-3, but maintaining the same level of talin-1, a cell could release the 1 µM ligand, but still bind higher affinity ligands (Figure 4.9A, black line).

A

6 kcal/mol coupling between domains

Domain	ΔG_{gap} (kcal/mol)	$\Delta\Delta G_{C, N+1}$ (kcal/mol)	[Ligand] (μM)
1) Ligand binding site	1	6	10
2) Metal binding site	1	6	0
3) Leg, LIBS antibody site	1	6	0
4) Transmembrane domain	3	6	0
5) Cyto Helix 1, Talin	2	2	variable
6) Cyto Helix 2, Kindlin	1	NA	0

B

6 kcal/mol coupling between domains
Binding of kindlin-3, 2 kcal/mol coupling to talin site

Domain	ΔG_{gap} (kcal/mol)	$\Delta\Delta G_{C, N+1}$ (kcal/mol)	[Ligand] (μM)
1) Ligand binding site	1	6	10
2) Metal binding site	1	6	0
3) Leg, LIBS antibody site	1	6	0
4) Transmembrane domain	3	6	0
5) Cyto Helix 1, Talin	2	2	0
6) Cyto Helix 2, Kindlin	1	NA	variable

C

6 kcal/mol coupling between domains
Binding of talin and kindlin-3, 2 kcal/mol coupling

Domain	ΔG_{gap} (kcal/mol)	$\Delta\Delta G_{C, N+1}$ (kcal/mol)	[Ligand] (μM)
1) Ligand binding site	1	6	10
2) Metal binding site	1	6	0
3) Leg, LIBS antibody site	1	6	0
4) Transmembrane domain	3	6	0
5) Cyto Helix 1, Talin	2	2	variable
6) Cyto Helix 2, Kindlin	1	NA	5

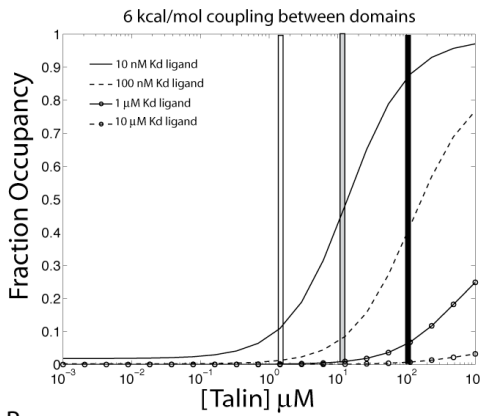**Figure 4.9 Multiple integrin regulators can produce diverse activation states.**

The fractional occupancy of a model integrin receptor as a function of talin-1 or kindlin-3 concentration in the presence of 10 μM ligand. Four different ligands were modeled (K_d = 10 nM, solid; 100 nM, dashed; 1 μM,

118

solid ball; 10 μM, dashed ball). Thermodynamic parameters for integrin subdomains are displayed to the right. (A) Receptor occupancy in the presence of talin-1, without kindlin-3 binding. White, grey, and black vertical lines mark 1 μM, 10 μM, and 100 μM of talin-1, respectively. (B) Receptor occupancy in the presence of kindlin-3, without talin-1. White, grey, and black vertical lines mark 1 μM, 10 μM, and 100 μM of kindlin-3, respectively. (C) Receptor occupancy as a function of talin-1 concentration, with a constant kindlin concentration (5 μM). White, grey, and black vertical lines mark 1 μM, 10 μM, and 100 μM of talin-1.

Chapter 5. Conclusions

We hypothesized that cytosolic regulation of the integrin αIIbβ3 is highly dependent on the membrane environment and uses coupled equilibria to transmit signals to the extracellular compartment. To test this, we studied the dynamics and structure of model αIIbβ3 cytoplasmic domains in the presence of phospholipids and detergents (Chapter 2). We showed that interactions in the integrin TM domain are coupled to structural changes in the αIIbβ3 cytoplasmic domain. The interaction between αIIb and β3 stabilizes a kink in the β3 cytoplasmic domain, which is likely to encourage interactions with the inner leaflet of the plasma membrane. These interactions occur in two helical regions that include the talin-1 and kindlin-3 binding sites. This demonstrates that both the talin-1 and kindlin-3 sites are coupled to the interactions between the αIIb and β3 TM domains, suggesting a pathway whereby both talin-1 and kindlin-3 can affect the TM state and therefore the affinity of the ectodomain for fibrinogen.

We also investigated the interactions between αIIbβ3 and its two regulators, talin-1 (Chapter 3) and kindlin-3 (Appendix A1). Preliminary studies showed that kindlin-3 binds the distal segment strongly in the absence of membrane. The distal kindlin-binding sequence is very dynamic and likely samples the cytoplasmic compartment frequently (Chapter 2). This suggests that kindlin-3 may bind the β3 cytoplasmic

domain without requiring a concerted interaction with the membrane, though membrane colocalization could serve to increase its affinity. This contrasts with talin-1. We showed that talin-1 binding to the integrin cytoplasmic domain is dependent on concerted interactions with the bilayer as its affinity for $\beta3$ increases nearly 1000 fold when the integrin is immobilized onto negatively charged membranes. Though the membrane significantly increases the affinity of talin-1 for the $\beta3$ cytoplasmic domain, its affinity for the integrin in the presence of membranes is not significantly higher than its affinity for negatively charged phospholipids alone. Similarly, we found that though talin-1 contains multiple lipid binding subdomains and that the interactions between these subunits and the bilayer are not cooperative. These results suggest that activation of the integrin by talin-1 is not opitimized for extremely high affinity as would be expected for perfectly cooperative interactions. Rather the energetics of the system suggest that the interactions are evolved for reversibility and sensitivity to changes in structure, post-translational modification, and lipid environment.

Fine-tuning of the integrin cytoplasmic domain for regulation and reversibility is befitting a receptor that must make dynamic interactions with the extracellular environment. Using a simple linked equilibrium model, we showed that coupling between the TM and the talin-1 and kindlin-3 binding sites can produce a range of extracellular functional states. Different affinity states for extracellular ligands are due to a change

in the distribution of active and inactive states rather than adoption of specific intermediate extracellular conformations. Integrins can access a large range of affinity states by simply shifting the relative amounts of talin-1 and kindlin-3 interacting with the cytoplasmic tail.

Appendix 1. Preliminary investigations of the interaction between kindlin-3 and αIIbβ3

I. Introduction.

Among FERM domain proteins, the kindlins (kindlin-1, kindlin-2, kindlin-3) are evolutionarily the closest to the talin family. Like talin-1, kindlin-3 binds to the β3 integrin cytoplasmic domain and is necessary for platelet integrin activation (7-10, 22). As the role of kindlin-3 in integrin function has only recently been appreciated, its mechanism of integrin regulation remains largely unclear. Talin-1 and kindlin-3 F3 subunits bind adjacent regions within the β3 cytoplasmic domain though it is unknown whether they bind simultaneously (22, 155). Talin-1 recognizes a segment that spans from the end of the TM to Tyr747 and includes TMproxH and CytoH1. Kindlin-3 recognizes a distal segment that immediately follows the talin-1 binding sequence, spanning from Ser752-Tyr759, and including CytoH2 (Figure 2.5). Both proteins require intact NPxY or NxxY motifs to bind (22, 155). The spacing between the talin-1 and kindlin-3 NPxY motifs is absolutely conserved in nearly all integrins, with the exception of the β5 integrins.

Like talin-1, the kindlin-3 FERM domain contains an additional F0 subunit. Whether kindlin-3 adopts a linear arrangement of like talin-1 (Figure 3.1) is unknown, since the structure of kindlin-3 has not been

solved. The kindlin-3 FERM domain also contains an inserted pleckstrin homology (PH) domain in its F2 subunit, which talin-1 lacks. The function of the PH domain has yet to be demonstrated, though PH domains – and FERM domains in general – are often involved in phospholipid interactions (26).

Our HDX data suggest that the $\beta3$ cytoplasmic domain makes significant interactions with the bilayer. In particular, the portion that binds talin-1 is significantly protected from HDX in the presence of phospholipids.   Furthermore, our NMR experiments show that αIIb induces a kink in the $\beta3$ cytoplasmic domain, which is likely to orient the $\beta3$ CT parallel to the membrane and further stabilize the interaction. We also have shown that the interaction between talin-1 and $\beta3$ is quite weak and requires a simultaneous interaction between talin-1 and the membrane to be significantly populated. In contrast, our HDX and NMR experiments have shown that the kindlin-3 binding sequence in $\beta3$, which is connected to the talin-1 sequence by a flexible linker, is highly dynamic and less helical and therefore less likely to bind the competing membrane surface. Based upon these results we hypothesized that the kindlin-3 sequence is more accessible than the talin-1 sequence, whether or not the protein/peptide interaction is more thermodynamically stable. A more dynamic kindlin-3 binding sequence would also not adopt a particular orientation relative the inner surface of the bilayer. This would suggest that unlike talin-1, kindlin-3 binding to the integin might be less dependent

on simultaneous interactions with the membrane. If this were the case, then kindlin-3 might bind the β3 CT with reasonably high affinity in the absence of membranes.   Below are initial experiments attempting to characterize the interaction between kindlin-3 and β3 to test the above model. We describe method for the purification full-length kindlin-3 from platelets and demonstrate that kindlin-3 binds to the β3 CT in the absence of bilayers.   These are initial experiments that are intended to be the starting points for future lab members.

II. Results

Purification of kindlin-3 from human platelets.

Kindlin-3 constructs were cloned into the pet28a vector and expressed in BL21-DE3 *E. coli.*   However, expression of constructs containing full-length kindlin-3, the F2PHF3 subunit, and the F3 subunit resulted in insoluble inclusion bodies.   We varied our expression conditions with temperatures ranging from 8°C to 37°C and IPTG concentrations ranging from 0.05 mM to 2 mM.   However, only the isolated PH domain could be stably expressed in *E. coli.* We therefore purified full-length kindlin-3 from outdated platelets.   Given its close homology to talin-1 and its localization to membranes, it was likely that kindlin-3 also contain positively charged surfaces. Therefore, the purification scheme (Methods) was designed around separation based on

charge. After several rounds of SP-Sepharose and size exclusion chromatography, we produced nearly 10 mg of 95% pure kindlin-3 from six units of outdated platelets (Figure A1.1A/B). The predicted molecular weight for kindlin-3 is 75.4 kD and the purified protein had a calculated molecular weight of 74 kD by equilibrium analytical ultracentrifugation (Figure A1.1C).
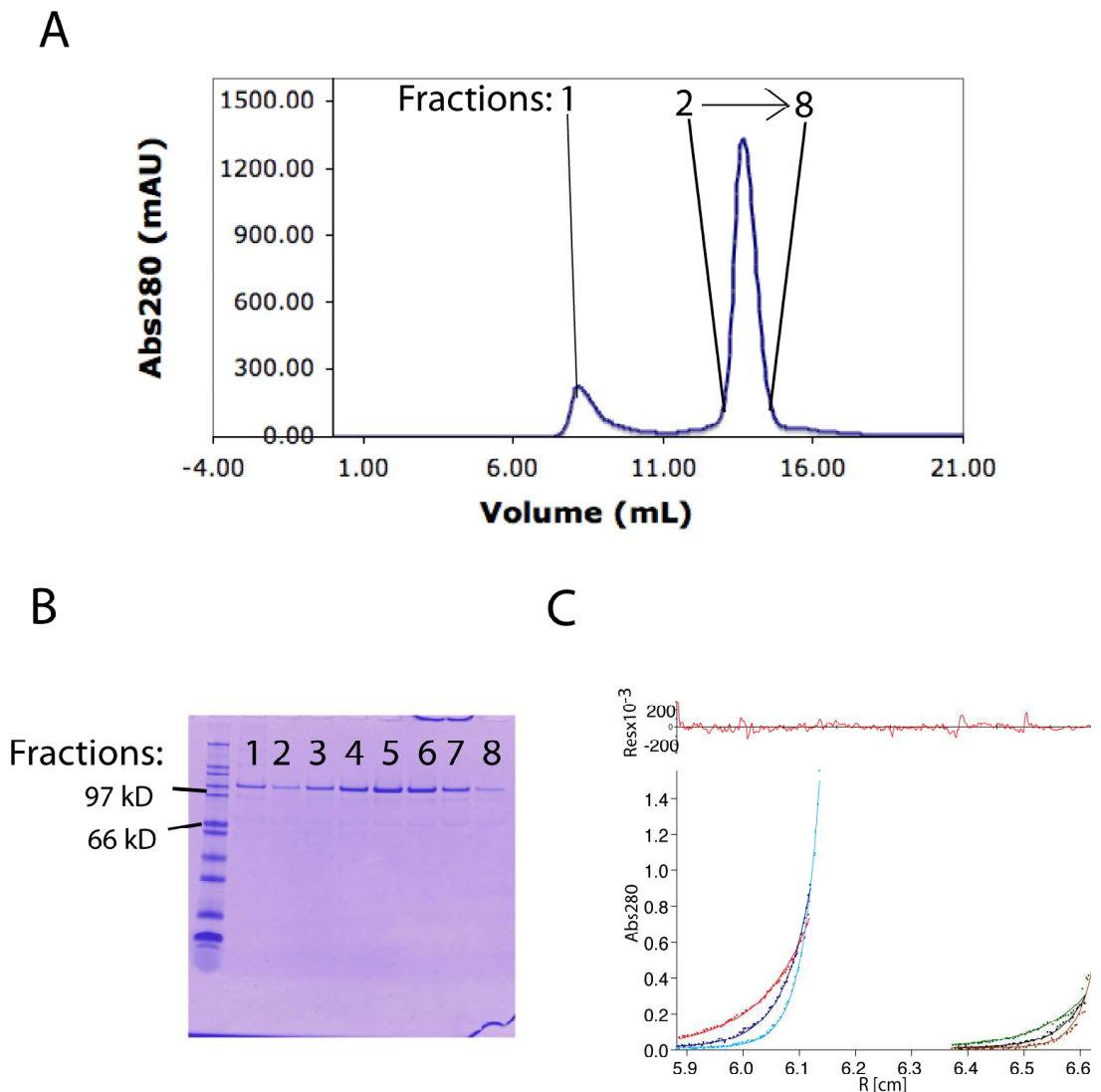
Figure A1.1 Purification of Kindlin-3 from platelets.

(A) Kindlin-3 was purified by several rounds of cation exchange chromatography (Methods) and refined by size exclusion on an analytical Superdex-200 column. (B) Analytical size exclusion chromatography fractions were run on NuPAGE SDS 10% Bis-Tris gels and stained with Coomassie Blue stain. Higher order aggregates eluted in the void volume (Fraction 1). Kindlin-3 eluted between 13 and 15 minutes (Fractions 2-8) and was found between the 66 kD and 97 kD bands of a Mark12 molecular weight standard. (C) Equilibrium analytical ultracentrifugation of the purified protein. Kindlin-3 was prepared in 25 mM MOPS 100 mM NaCl, pH 7 at 3 μM (left) and 1.5 μM (right). The samples were sedimented at 15000 rpm, red/green, 20000 rpm, dark blue/black, and 25000 rpm, light blue/brown. Data were globally fit using the Igor software

program to a MW of 74 kD. *{AUC experiments were performed once. Performed by DTM with the guidance of PB.}*

Preliminary experiments suggest kindlin-3 binds β3 with high affinity in the absence of bilayers.

Our HDX and NMR measurements of the β3 cytoplasmic domain showed that the kindlin-3 binding sequence is very dynamic and likely adopts many conformations relative to the membrane surface. We therefore hypothesized that, unlike talin-1 interaction with β3, kindlin-3 might not depend on a coordinated interaction with the bilayer surface. If this were the case, then the complex between kindlin-3 and β3 should be stable at much lower concentrations than the interaction between talin-1 and β3. We used analytical ultracentrifugation to measure the interactions of labeled β3 with both talin-1 and kindlin-3 in the absence of membranes. In each case 1 μM of BODIPY TMR labeled β3 CT (MW 6242 kD, prepared as in Chapter 2 for FP) was sedimented in the presence of excess kindlin-3 (3.5 μM or 1.75 μM) or excess talin-1 (10 μM). In the presence of 10 μM talin-1, labeled β3 cytoplasmic domain sedimented with an apparent molecular weight of 7.7 kD (Figure A1.2A), which is close to its predicted monomeric 6.2 kD mass. In the presence of kindlin-3, there was a clear shift towards higher molecular weight species. Global fitting of both kindlin-3 concentrations resulted in estimation of a dissociation constant between 100 nM and 3 μM (Figure A1.2B). Single

species fits produced molecular weights of 43 kD and 12 kD for the 3.5:1 and 1.75:1 experiments, respectively, suggesting a Kd on the order of several micromolar. However, without higher concentrations of kindlin-3 and β3, it is impossible to calculate the affinity for β3 with higher accuracy. This would require more kindlin-3 than could be prepared for the experiment.

Figure A1.2 Equilibrium AUC of Kindlin-3 and β3.

(A) Equilibrium AUC of 10 μM talin-1 and 1 μM BODIPY TMR-β3. Sedimentation was monitored at 600 nm. The sample was sedimented at four velocities (10000 rpm black, 15000 rpm blue, 20000 rpm green, 25000 rpm red). Data were globally fit to a single species of 7.7 kD using Igor. (B)Kindlin-3 and BODIPY-β3 were combined in two ratios: 3.5 μM kindlin-3 and 1 μM BODIPY-β3 (left) and 1.75 μM kindlin-3 and 1 μM BODIPY-β3 (right). Sedimentation AUC was performed while monitoring 600 nm absorbance at three velocities (15000 rpm red/brown, 20000 rpm dark blue/light blue, and 25000 rpm green/black). Sedimentation was globally fit to a two species 1:1 binding model with the ε600 for Kindlin held to 700 cm^{-1}M^{-1} and ε600 for BODIPY-β3 held to 70000 cm^{-1}M^{-1}. Due to the low protein concentration and absorbance relative to background, sedimentation fit equally well to dissociation constants between 100 nM and 3 μM. *{AUC performed once by DTM under the guidance of PB.}*

III. Methods

Kindlin-3 purification. Six to 10 units of outdated platelets (Hospital of the University of Pennsylvania Blood Bank) were lysed by N$_2$ bomb on ice in the presence of mammalian protease inhibitors and 10 mM EDTA, 100 mM NaCl. EDTA was necessary to prevent significant proteolysis of kindlin-3. Lysates were centrifuged at either 30k x g or 100k x g to clear insoluble debris. After clearance, lysates were mixed with Q-Sepharose batch-wise for 1 hour at 4 degrees Celsius to clear serum and negatively charged proteins. The cleared lysate was loaded onto SP-sepharose (25 mL) in 50 mM NaCl batchwise and poured into a high-pressure FPLC column for elution on gradient between 50 mM NaCl and 400 mM Arginine, pH 7 on a Akta FPLC (GE Healthcare). The kindlin-3 containing fractions were then concentrated and loaded onto a high resolution SP-

sepharose column (16/10, 25 mL bed volume) (GE Healthcare) and eluted over a 400 mL gradient. At this point, the primary impurities were full length talin and talin head domain, which were largely removed by size exclusion on Superdex200 or Superdex75 analytical column (200 uL injection volume) (GE Healthcare). A final high resolution SP sepharose step was performed on a 400 mL gradient to 400 mM Arginine.

Equilibrium Analytical Ultracentrifugation. Purified peptide and protein samples were prepared in 25 mM MOPS 100 mM NaCl, pH 7.0. Experiments were performed at 25°C. Samples were loaded into a 6-channel carbon-epoxy centerpiece and centrifuged at 10000 rpm, 15000 rpm, 20000 rpm, and 25000 rpm in a Beckman XL-I analytical ultracentrifuge. Samples were monitored at 280 nm and 600 nm in a 1.2 cm path length cell. The molecular weight and partial specific volumes of kindlin-3 were calculated to be 75.4 kD and 0.73 ml/g, respectively using SEDINTERP. The buffer density was calculated to be 1.003 g/ml. Data were globally fit using Igor Pro (Wavemetrics).

Appendix 2. NMR studies of the c-Src SH3 domain and the β3 cytoplasmic domain.

I. Introduction

Src family kinases (SFKs) are a family of non-receptor tyrosine kinases implicated in a number of biological processes (156, 157). There are nine human SFKs expressed—often redundantly—in nearly all human tissues (158). Of the SFKs, c-Src is the best studied, being discovered as the first proto-oncogene in the 1970s (159). Redundancy in SFK paralog expression has resulted in single-gene knockout phenotypes that are unremarkable, especially in the case of platelets (158). In order to observe a significant platelet phenotype, it was necessary to generate platelets deficient in six kinases (c-Src, Fyn, Fgr, Hck, Lyn, and Yes), which resulted in reduced platelet spreading on the αIIbβ3 ligand fibrinogen (160). These gene-deleted platelets and wild-type platelets treated with SFK inhibitors do not have a defect in integrin activation or ligand binding. Rather they have a downstream defect in tyrosine phosphorylation and cytoskeletal mobilization after initial adhesion to fibrinogen, suggesting that SFKs participate in platelet integrin outside-in signaling, which is supported by the fact that SFKs are recruited to the integrin associated cytoskeleton after platelet aggregation (161, 162) and that c-Src activation requires binding of αIIbβ3 to fibrinogen (160).

SFKs contain well-conserved domain structures (Figure A2.1). Each SFK contains an N-terminal membrane anchor followed by a flexible

linker (black), a Src Homology 3 (SH3, purple) domain, a flexible linker (blue), a Src Homology 2 (SH2, green) domain, a flexible linker (yellow), the kinase domain (orange), and then finally a C-terminal regulatory tail (red). Inactive SFKs adopt compact structures that are stabilized by multiple intramolecular interactions (163). In the inactive state, the phosphotyrosine recognizing SH2 domain (green) binds to the phosphorylated C-terminal tail (red). The inactive conformation is also stabilized by an interaction between the SH3 (purple) domain and a second internal ligand in the linker (yellow) between the SH2 and kinase domains. C-terminal Src Kinase (CSK) phosphorylates the C-terminal tail (164), while protein-tyrosine phosphatase-1B (PTP-1B) activates the kinase by dephosphorylating the C-terminus (165). Activation also requires phosphorylation of a regulatory loop in the kinase domain.

In the active state, the SH2 and SH3 domains are free to interact with other proteins. Such interactions stabilize the active kinase state and determine the localization of SFKs (156). Localization also depends on the N-terminal membrane anchor. All SFKs are myristoylated and a subset are palmitoylated (166, 167). C-Src is not palmitoylated and contains a conserved patch of positively charged Arg and Lys residues (Figure A2.1), which has been demonstrated necessary for binding of c-Src bilayers containing negatively charged phospholipids such as phosphatidylserine and phosphatidylglycerol (25) (29).

+ + +   +++
N-terminus: Myristoyl-GSNKSKPKDASQRRR
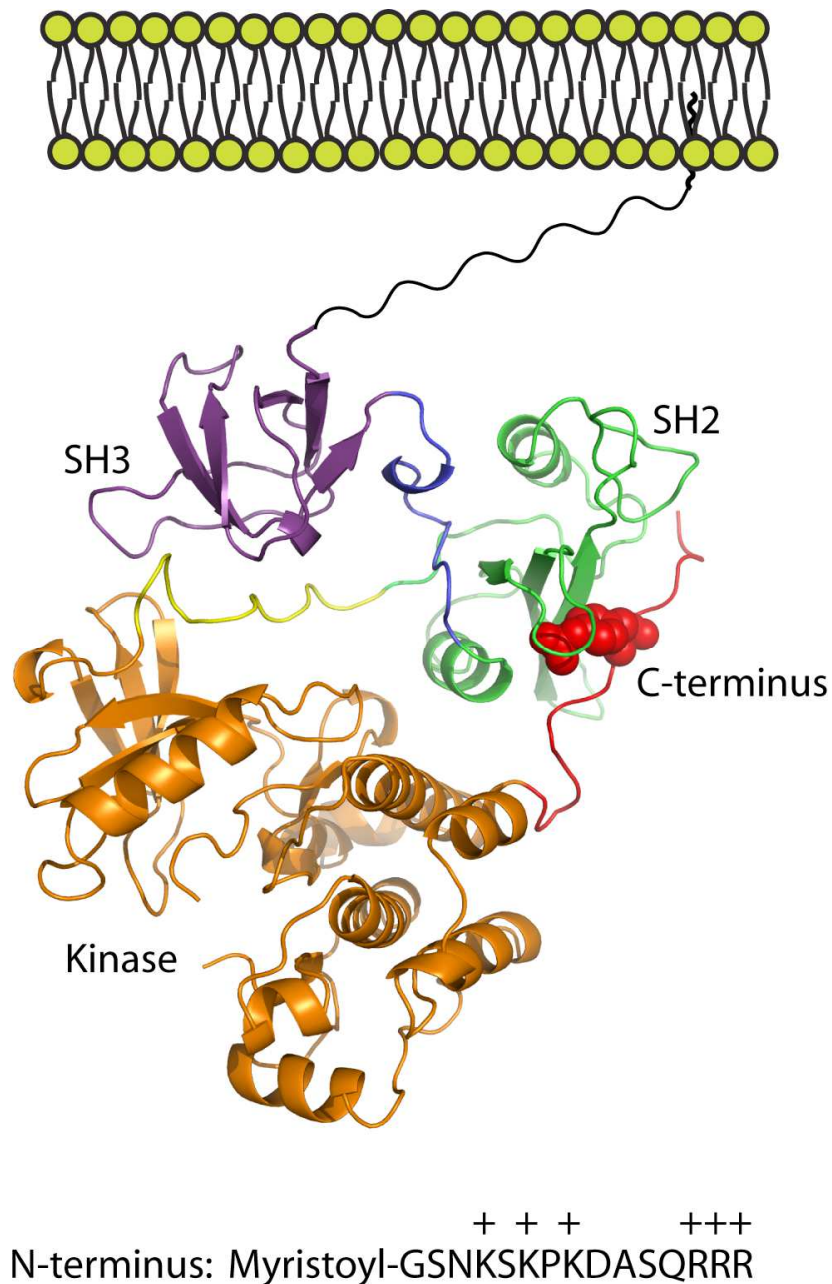
Figure A2.1 Domain structure of c-Src in its inactive conformation.

From N- to C-terminus: 1) N-terminal membrane anchor that is post-translationally myrstoylated (Black).   C-Src contains a stretch of basic amino acids (bottom). 2) SH3 domain (purple) 3) Interdomain linker (blue). 4) SH2 domain (green). 5) SH2-kinase linker (yellow) 6) Kinase domain (orange). 7) C-terminal regulatory tail (red).

SFK substrate specificity appears to be less dependent on the substrate sequence than physical proximity (168). Therefore, the specificity of SFK protein-protein and protein-lipid interactions is extremely important in determining function. Recruitment to integrin signaling complexes could potentially involve the N-terminal membrane anchor, the SH3 domain, and the SH2 domain. Both the SH3 and SH2 subunits of c-Src have been shown to interact with Focal Adhesion Kinase (FAK) (169) and p130Cas(170, 171), two proteins found in integrin signaling complexes. A number of studies have also suggested that c-Src binds directly to the last three residues (Arg760-Gly761-Thr762) of the β3 integrin cytoplasmic domain (23). Transgenic platelets containing mutations in this region exhibited defects in spreading and down-stream integrin events (137, 172). The Arg-Gly-Thr motif implicated in the c-Src / β3 interaction is quite different from the canonical polyproline sequence recognized by the c-Src SH3 domain (Figure A2.2B) (173). The polyproline backbone packs against a groove composed of aromatic residues (Tyr93, Tyr95, Tyr139) (174, 175). A specificity pocket defined by Trp121 and Tyr134 is at the end of the aromatic groove and is flanked by the n-Src loop and the RT-loop, which affect substrate specificity (173).

We hypothesized that the β3 cytoplasmic domain may bind to the c-Src SH3 domain either along the Tyr-groove or in the aromatic specificity pocket. We characterized integrin/SH3 interaction using biophysical techniques sensitive to perturbation at these residues. We were surprised

135

to find that the interaction is much weaker than predicted by published biological and biochemical studies(23, 137, 172), suggesting that the interaction may depend on other proteins or the lipid environment.
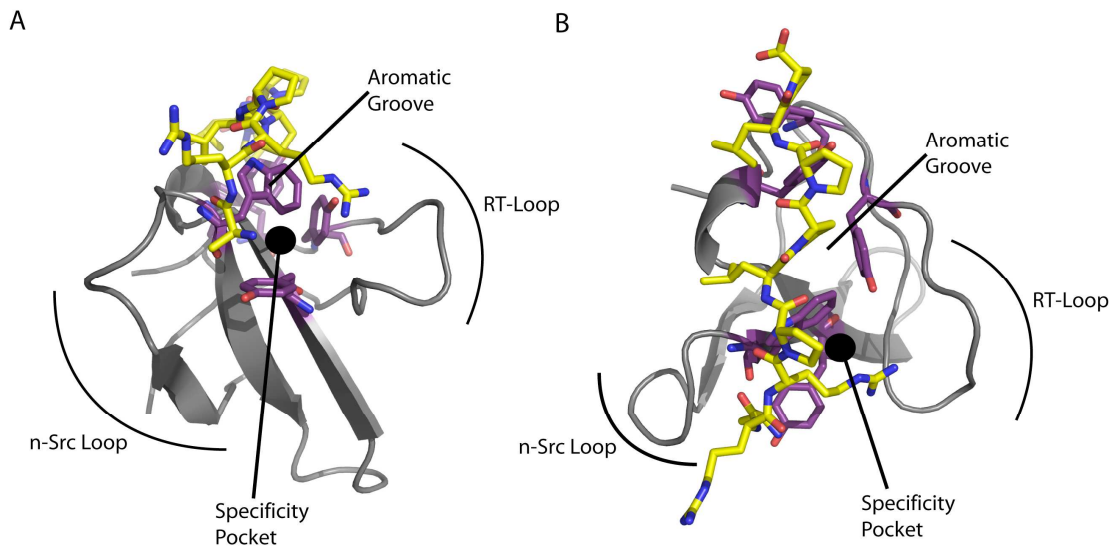
Figure A2.2. The interaction between the c-Src SH3 domain and a polyproline peptide.

Interaction between the c-Src SH3 domain and a polyproline peptide (yellow) is shown down the axis of the peptide (A) and rotated 90° (B). The interaction requires packing of the polyproline backbone against an aromatic groove and "specificity pocket" composed tyrosine and tryptophan residues (purple). Residues from the RT-loop and the n-Src loop interact with the backbone and side chains of the peptide and help determine the sequence specificity of the interaction (PDB code 1nlp)

II. Results

C-Src, β3 integrin, and polyproline constructs.

The c-Src SH3 domain was cloned between residues Ala83 and Ser143 into the pet28a vector with an N-terminal 6xHis tag followed by a thrombin cleavage site for removal of the affinity tag. The β3 cytoplasmic domain (β3-NITYRGT) between residues Asn756 and Thr762 was

synthesized on Wang resin generating a short seven amino acid peptide containing the Arg-Gly-Thr binding motif c-Src binding motif. Wang resin was chosen because the resulting peptide contained a C-terminal carboxylate like the natural sequence. The polyproline peptide Arg-Pro-Leu-Pro-Pro-Leu-Pro with a C-terminal amide was synthesized on Rink-amide resin.

Circular dichroism and Trp-fluorescence of c-Src SH3 domain and the β3 C-terminus.

It has been reported that c-Src co-immunoprecipitates αIIbβ3, that the SH3 domain interacts with the β3 C-terminus by ELISA with a micromolar binding binding constant, and that mutations to the β3 C-terminal Arg-Gly-Thr sequence results in outside-in integrin signaling defects (23, 137, 172). Though the integrin sequence is quite different from the canonical polyproline ligand, we hypothesized that the interaction might also occur along the Tyr-groove or the Trp-containing specificity pocket. Changes in the local environment surrounding aromatic residues can often be measured by changes in CD signal or Trp fluorescence (176). Binding of polyproline ligands to this region was previously observed using these techniques (177) (178). We therefore attempted similar experiments with our β3-NITYRGT peptide, reasoning that such studies would support binding to the aromatic region of the SH3 domain.

Solutions containing 40 μM SH3 domain and 650 μM β3-NITYRGT were prepared in pH 7.0 25 mM phosphate 100 mM NaCl. CD spectra

were taken of each sample (Figure A2.3). The SH3 domain was then mixed 1-to-1 with the β3-NITYRGT peptide and the CD spectrum of the mixture was taken (Figure A2.3A, green). The expected spectrum for the mixture in the absence of interaction was also calculated by averaging the SH3 and β3-NITYRGT spectra (Figure A2.3A, green dash). The difference between the expected and experimental CD spectra was then calculated (Figure A2.3A, red). There was no significant difference between the two, demonstrating that mixing the β3-NITYRGT peptide and SH3 domain resulted in no change in CD signal at the concentrations used. However, when similar experiments were performed with 650 μM polyproline RPLPPLP (Figure A2.3B), a clear shift in the CD was observed (Figure A2.3B, red). The difference spectrum for RPLPPLP has a maximum at 225 nm, which replicates previously published results (177).

A

B

C

139
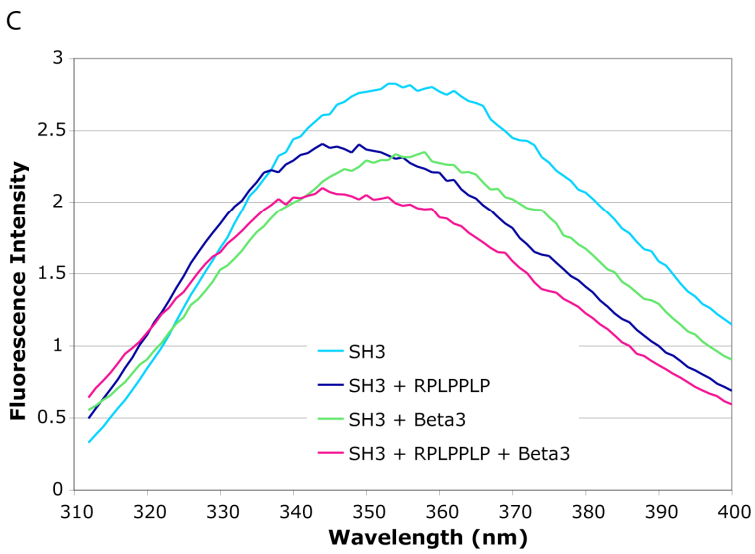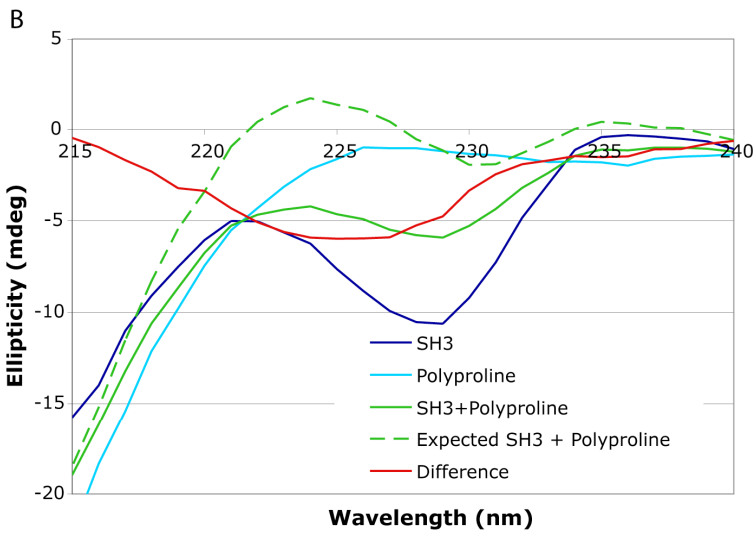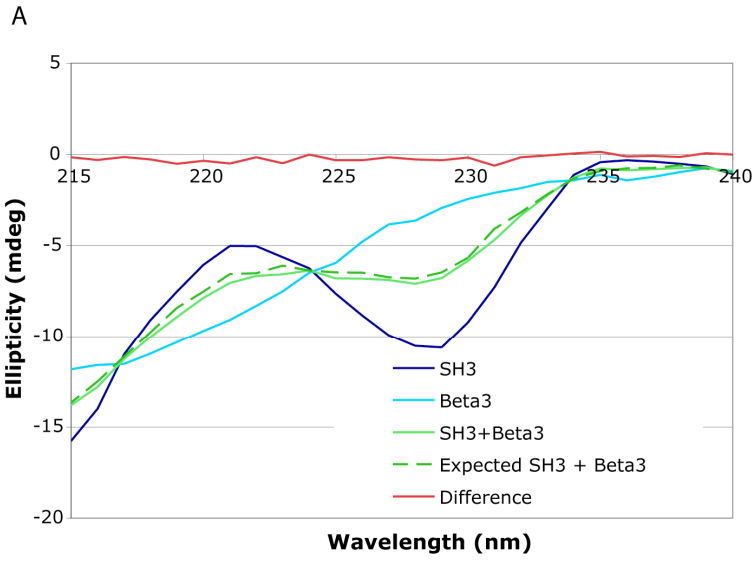
Figure A2.3 Comparison of CD and Trp fluorescence changes in the presence of a polyproline peptide and β3-NITYRGT.

Protein and peptide samples were prepared in 25mM phosphate 100 mM NaCl, pH 7.0. (A) CD spectra were taken of 40 μM c-Src SH3 domain (dark blue), 650 μM β3-NITYRGT peptide (light blue), and a 1:1 mixture of the two samples with 20 μM SH3 and 325 μM β3-NITYRGT (green). The expected spectrum in the absence of interaction was calculated by averaging the SH3 and β3 spectra (dashed green). The difference between the actual and expected spectra was calculated (red). (B) CD spectra were taken of 40 μM c-Src SH3 domain (dark blue), 650 μM polyproline (light blue), and a 1:1 mixture of the two samples with 20 μM SH3 and 325 μM polyproline (green). The expected spectrum in the absence of interaction was calculated by averaging the SH3 and polyproline spectra (dashed green). The difference between the actual and expected spectra was calculated (red). (C) Tryptophan emission spectra of the c-Src SH3 domain. SH3 solutions with or without peptide were excited at 295 nm and emission spectra were recorded from 300-400 nm. Spectra were recorded for 50 μM SH3 domain alone (light blue), 50 μM SH3 domain with 200 μM polyproline (dark blue), 50 μM SH3 domain with 200 μM β3-NITYRGT (green), and 50 μM SH3 domain with 200 μM polyproline and 200 μM β3-NITYRGT (magenta). *{CD and fluorescence experiments are representative of three independent experiments. Protein and peptide samples were made by DTM. Experiments were performed by DTM.}*

Binding of a polyproline ligand to the c-Src SH3 domain results in a blue shift in tryptophan fluorescence (178). We reasoned that though mixing of the c-Src SH3 domain and β3-NITYRGT did not result in a significant change in circular dichroism, if the β3 peptide bound to the tryptophan containing specificity pocket in the SH3 domain, it might induce in a similar blue shift in fluorescence. A 50 μM solution of SH3 was excited at 295 nm and an emission spectrum was recorded between 300 and 400 nm, with an emission maximum at 355 nm (Figure A2.3C, light blue). The same measurement was performed on a second solution

containing 50 μM SH3 and 200 μM β3-NITYRGT, with an emission

maximum at 356 nm (Figure A2.3C, green). In comparison, the addition of

200 μM RPLPPLP shifted the SH3 emission maximum to 347 nm (Figure

A2.3C, dark blue). Finally, the emission maximum for a sample containing

50 μM SH3, 200 μM β3-NITYRGT, and 200 μM RPLPPLP was at 346 nm.

These results show that unlike the polyproline peptide, the integrin

cytoplasmic domain peptide does not cause a blue shift in the SH3

domain Trp-emission spectrum. Likewise, it does not compete for binding

of the SH3 domain to the polyproline sequence.

NMR titration of the β3 cytoplasmic domain the c-Src SH3 domain.

Our CD and Trp fluorescence experiments did not demonstrate an

interaction between the c-Src SH3 domain and β3-NITYRGT at

concentrations as high as 350 μM β3-NITYRGT. We reasoned that the

interaction was either extremely weak and not observed at the

concentrations used or it might occur outside of the aromatic groove or

specifity pocket and therefore CD and Trp fluorescence would not be well

suited for the measurement. We chose to use NMR, which has

successfully been used to study weak protein-protein interactions (179).

The c-Src SH3 domain was expressed in ^{15}N M9 minimal media and

purified by nickel chromatography. The 6xHis tag was removed using

thrombin protease and the purified protein was transferred into pH 6.0

phosphate buffer containing 100 mM NaCl and concetrated. Two NMR samples were prepared for ^{1}H-^{15}N HSQC NMR. The first contained 1 mM ^{15}N SH3 (Figure A2.4, red) and the second contained 1 mM ^{15}N-SH3 and 15.7 mM β3-NITYRGT peptide (Figure A2.4, magenta). In the presence of 15.7 mM β3-NITYRGT, a number of SH3 residues exhibited changes in chemical shift. The interaction appears to be in fast exchange, as only shifts in peak location were observed. Slow exchange binding would be expected to generate two sets of peaks corresponding to the bound and unbound forms, while intermediate exchange would produce broadened signals of both species with potentially a loss of intensity. In this titration, peaks remained sharp and intense.
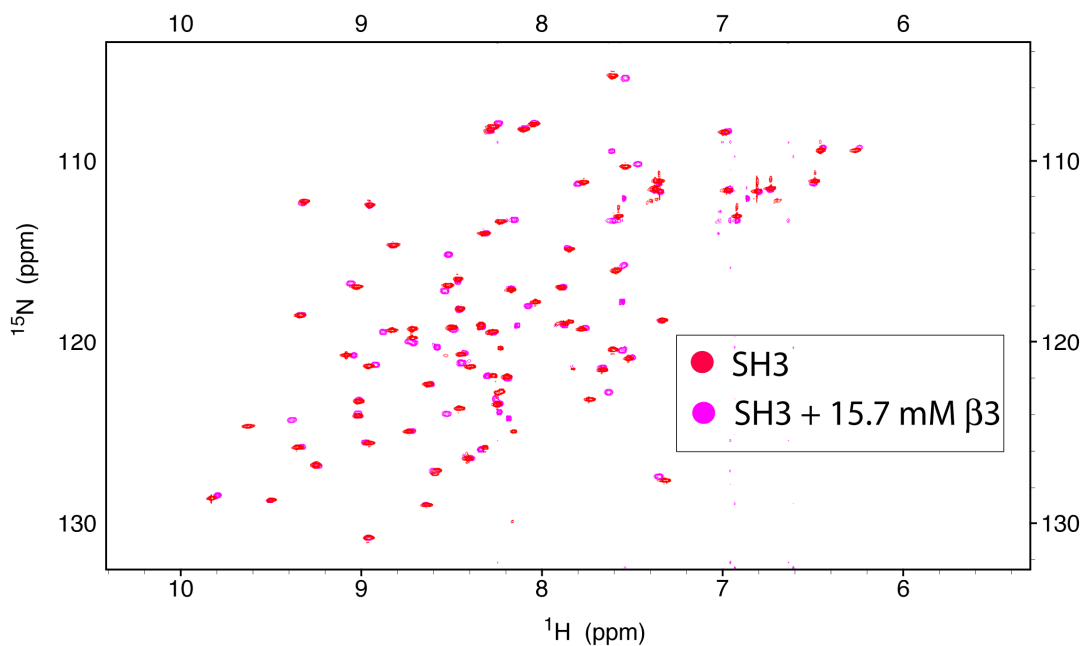
Figure A2.4 Changes in SH3 chemical shift in the presence of β3-NITYRGT

(A) ^{1}H-^{15}N HSQC spectra of samples containing 1 mM c-Src SH3 domain (red) and 1 mM ^{15}N-labeled c-Src SH3 domain with 15.7 mM β3-NITYRGT (magenta). Both samples were prepared in pH 6.0 20 mM phosphate containing 100 mM NaCl. *{Samples prepared by DTM. Experiment performed by DTM with help of HC.}*

The difference in the HSQC spectrum for each residue was calculated by the relationship $\Delta ppm = (\Delta^1H^2 + (\Delta^{15}N/5)^2)^{1/2}$ (Figure A2.5A). The standard deviation for the per residue chemical shift change was 0.04. Sixteen residues had chemical shifts greater than one standard deviation: Tyr95, Glu96, Arg98, Thr99, Glu100, Thr101, Asp102, Leu103, Phe105, Asn115, Asn116, Glu118, Trp121, Ser126, Gly130, and Tyr134. SH3 residues were color coded according to their chemical shift change and mapped onto a previously reported structure of the c-Src SH3 domain (Figure A2.5B/C). The majority of residues perturbed by β3-NITYRGT were in the n-Src and RT-loops and centered around the specificity pocket (Trp121 and Tyr134). The largest chemical shift changes occurred in residues in or adjacent to the RT-loop, especially residues Arg98 (0.25 ppm), Glu100 (0.15 ppm), and Asp102 (0.13 ppm). Tyr93, Tyr95, and Tyr139 form the aromatic polyproline binding groove (Figure A2.2, magenta) that binds polyproline ligands. Of these, only Tyr95, which is adjacent to the specificity pocket, was perturbed by β3-NITYRGT. Tyr93 and Tyr139 were unchanged (Figure A2.5B/C, magenta).
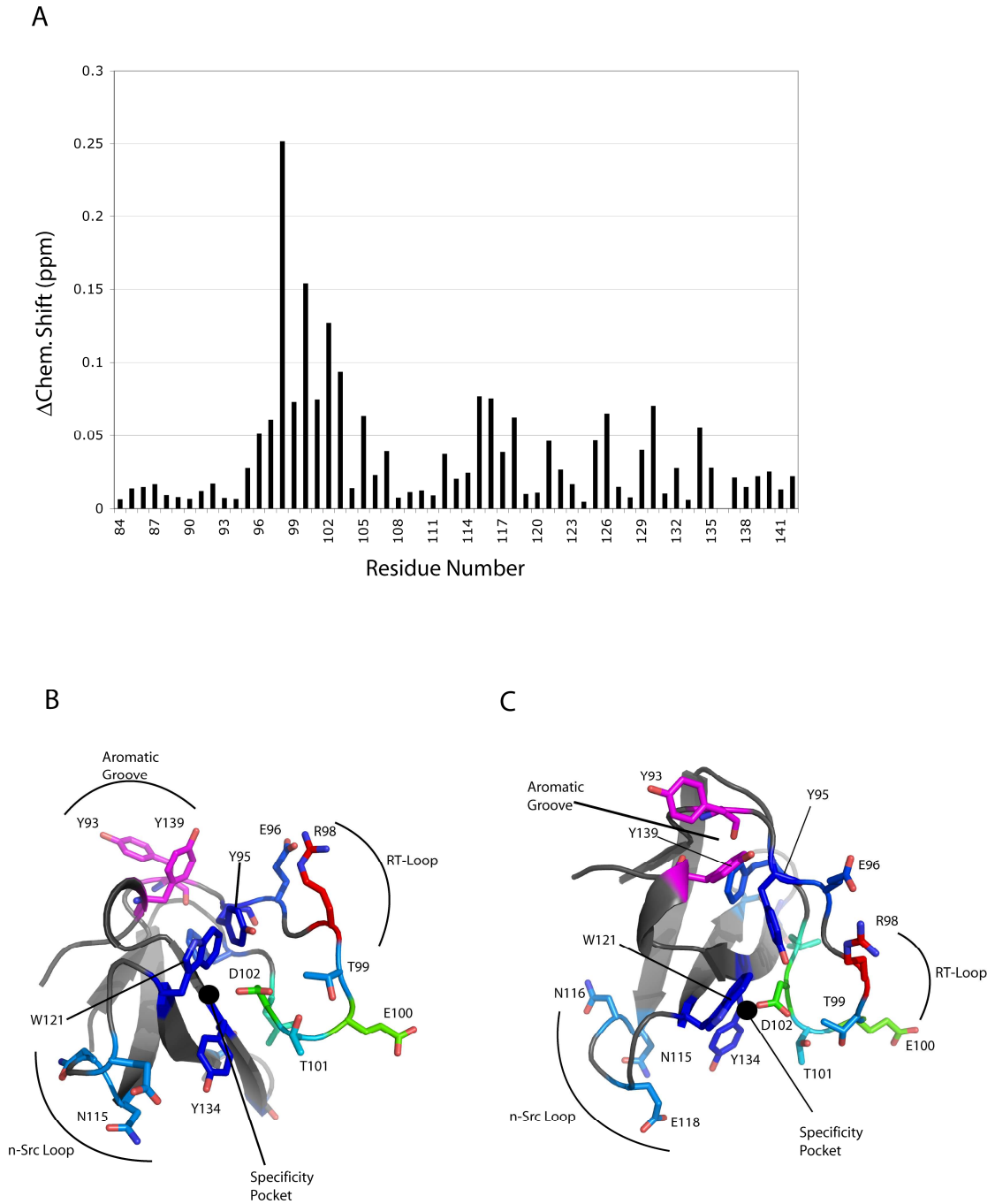
Figure A2.5 β3-NITYRGT causes chemical shift changes centered around the SH3 specificity pocket.

(A) The change in chemical shift in the presence of 15.7 mM β3-NITYRGT (Figure A2.4) was calculated by the equation $\Delta ppm = (\Delta^1H^2 + (\Delta^{15}N/5)^2)^{1/2}$. (B) Chemical shift changes were color coded and mapped onto a previously solved NMR structure of the c-Src SH3 domain (pdb

code 1nlp). The maximum chemical shift change was 0.25 ppm (red, Arg98). The minimum cutoff was 0.05 (dark blue, Tyr95). Tyr95 is part of the aromatic groove that binds polyproline ligands. The remaining residues in the aromatic groove (Tyr93 and Tyr139) did not have significant changes in chemical shift and are colored magenta.

The SH3 NMR sample containing 15.7 mM β3-NITYRGT was serially titrated against the sample containing only SH3 domain. This produced NMR samples with constant 1 mM SH3 concentrations and β3-NITYRGT concentrations ranging between 5.3 mM and 15.7 mM. HSQC spectra were recorded for each sample. Figure A2.6A shows the change in Arg98 chemical shift with the addition of β3-NITYRGT. The relationship was linear (Figure A2.6B), indicating that the titration had not reached saturation and that the majority of SH3 domain was unbound, even in the presence of 15.7 mM β3-NITYRGT. Since the majority of the protein was not bound, $[SH3]_{total}$ approximates $[SH3]_{free}$ and $[\beta3]_{total}$ approximates $[\beta3]_{free}$. Therefore, the relationship Δ(chem. shift) = Δppm_{max} * $([SH3]_{free}*[\beta3]_{free})/(K_D*[SH3]_{total})$ simplifies to Δ(chem. shift) =[Ligand]* $(\Delta ppm_{max}/Kd)$. The term Δppm_{max} represents the change in chemical shift when the SH3 domain is fully bound by ligand. As the slope is linear, it can be assumed that the maximum chemical shift change is on the order of 10 fold the observed change, or 2.5 ppm. Since the maximum reasonable change in chemical shift is 5 ppm for any protein-protein interaction, this places the Kd between 175 mM and 350 mM..
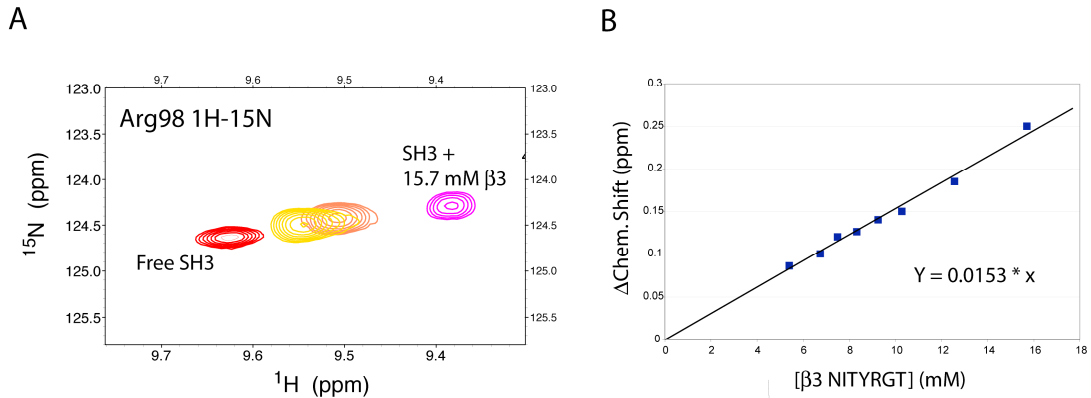
Figure A2.6 ^{1}N-^{15}N **HSQC titration of β3-cytoplasmic domain and c-Src SH3.**

(A) ^{1}H-^{15}N HSQC spectrum c-Src SH3 residue Arg98 backbone amide without (red) and with 5.3 mM (yellow), 8.4 mM (orange), and 15.7 mM (purple) β3-NITYRGT. (B) Relationship between Arg98 chemical shift change and total concentration of β3-NITYRGT. The change in chemical shift was calculated according to the equation Δppm = $(\Delta^1H^2 + (\Delta^{15}N/5)^2)^{1/2}$. The data was fit to a linear curve with a slope 0.0153 ppm/(mM titrant). *{Samples prepared by DTM. Experiments performed by DTM.}*

III. Discussion.

Though SFKs are necessary for integrin outside-in signaling, how they are recruited to these signaling complexes and the degree of specificity built into the nine different kinases remains unclear. SFKs contain multiple subunits capable of making protein-protein and protein-lipid interactions, therefore targeting to a particular signaling complex could potentially require the coincidence of multiple relatively weak interactions. There is clearly a degree of redundancy built into SFK signaling in platelets as six kinases are required to be knocked out to generate platelets that are unable to spread on fibrinogen. As a starting

point for understanding the regulation of these processes, we have investigated the interactions between c-Src and the β3 integrin cytoplasmic domain.

We sought to characterize the interaction between the c-Src SH3 domain and the β3 integrin cytoplasmic domain C-terminus. Several lines of evidence have suggested that the c-Src SH3 domain specifically binds to the β3 integrin cytoplasmic domain. It has been shown that mutations to the terminal Arg-Gly-Thr sequence result in decreased spreading of both transfected cells (23, 180, 181) and platelets on a surface coated with the αIIbβ3 ligand fibrinogen(137); that mutations to this sequence disrupt co-immunoprecipitation of c-Src and αIIbβ3(160); that mutations to this sequence block solid-phase binding of GST-SH3 domain to the β3 cytoplasmic domain (23, 181); and that a synthetic membrane permeable peptide containing the Arg-Gly-Thr sequence disrupts platelet c-Src signaling (182). The interaction was studied in solution using monomeric c-Src and β3 constructs in contrast to the previously reported solid-phase experiments, which used a dimeric GST-SH3 fusion protein(23). There was no evidence of the interaction by circular dichroism or tryptophan fluorescence and β3 did not compete with binding by a polyproline ligand. It is possible that an interaction between β3 and the SH3 occurs away from the canonical polyproline binding pocket, therefore we chose to study the interaction by NMR. We found that addition of the β3 C-terminus does in fact cause chemical shift changes in the SH3 domain in the region of

147

the specificity pocket. However this requires extremely high concentrations of β3 and even 15.7 mM β3 does not saturate the SH3 domain and the calculated dissociation constant may be as high as several hundred millimolar.

Typical polyproline ligands contain Lys or Arg residues that pack against the Trp and Tyr in the specificity pocket and make electrostatic interactions negatively charged residues provided by the n-Src or RT-loop. The β3 sequence provides a conserved Arg residue at position 759 in the Arg-Gly-Thr sequence and replacement of this sequence with a Glu-Gly-Lys is reported to disrupt c-Src signaling and interactions with β3 (181). Further NMR studies are necessary with similar mutant peptides to determine whether such a sequence substitution will also disrupt the interaction seen by NMR.

Our measured interaction is much weaker than that reported for binding of solid-supported β3. It is possible that the differences in the β3 cytoplasmic domain constructs used can account for the significant variation between our results and those reported previously. We chose to use the C-terminal seven residues for our NMR experiments as these residues have previously been shown necessary for binding. The discrepancy in apparent β3 binding affinity may partially be due to avidity effects of surface binding by dimeric GST-SH3 fusion proteins (23, 181). It is also possible a third species (or more) may be necessary for the apparent interaction to occur under biological conditions. The adjacent

sequence in the β3 cytoplasmic domain also recognizes members of the kindlin and filamin families of protein and therefore could conceivably cooperate in binding. C-Src also binds other integrin signaling molecules including FAK (169) and p130Cas(170, 171). Further studies are needed to characterize the recruitment of SFKs to integrin adhesions and to determine whether the membrane environment plays a role.

IV. Methods

Protein and peptide constructs used. The c-Src SH3 domain was cloned between Ala83 and Ser143 into a pet28a vector between the NdeI and XhoI restriction sites. Expression was performed in BL21-DE3 cells (Novagen). They were grown in LB-media to an OD600 of 0.5 at 37°C and 1 mM IPTG was added. After 3 hours of expression, cells were lysed by tip sonication on ice for 20 minutes in pH 7, 500mM NaCl, 20mM imidazole with a protease inhibitor cocktail (Sigma-Aldrich) containing 1 mM EDTA. The lysates were cleared by centrifugation at 30,000 g for 30 minutes. The supernatant was loaded onto a HiTrap Ni-NTA column (GE Healthcare) and eluted over a 50 mL gradient to 500 mM imidazole. Imidazole was dialyzed away overnight into pH 7.5 Tris, 100 mM NaCl, in the presence of thrombin protease (GE Healthcare) to remove the 6xHis tag. The SH3 domain then purified away from the 6xHis tag by DEAE ion exchange chromatography.

149

β3-NITYRGT was synthesized on Wang resin preloaded with a Thr residue using a Symphony peptide synthesizer at 0.1 mM scale in 25% DMSO/75% NMP with Fmoc-chemistry. β3-NITYRGT was N-terminally acetylated and cleaved from the resin TFA/triethylsilane/water (95/2.5/2.5 v/v) for three hours and precipitated into dry-ice cold diethylether. β3-NITYRGT was purified by reverse phase HPLC (Varian Prostar) using a C4 preparative column (Vydac) on a water/acetonitrile gradient with 0.1% TFA.

RPLPPLP was synthesized on Rink-amide resin using a Symphony peptide synthesizer at 0.1 mM scale in 25% DMSO/75% NMP with Fmoc-chemistry. RPLPPLP was N-terminally acetylated and cleaved from the resin TFA/triethylsilane/water (95/2.5/2.5 v/v) for three hours and precipitated into dry-ice cold diethylether. β3-NITYRGT was purified by reverse phase HPLC (Varian Prostar) using a C4 preparative column (Vydac) on a water/acetonitrile gradient with 0.1% TFA.

Circular dichroism. Purified c-Src SH3 domain was transferred to CD buffer (mM phosphate 100 mM NaCl, pH 7.0) by dialysis and a stock containing 40 μM protein was made (calculated by absorption at 280 nm). Stocks of β3-NITYRGT and RPLPPLP were made in the CD buffer by weighing out the respective peptides dissolving them in the appropriate volume of buffer. CD spectra were taken on a JASCO J-810

spectropolarimeter. Measurements were made stepwise for each 1 nm between 215 nm to 240 nm and averaged over three scans at 25°C.

Tryptophan fluorescence. Stocks of purified c-Src SH3, β3-NITYRGT, and RPLPPLP were prepared in CD buffer. Three samples were prepared: 50 μM SH3, 50 μM SH3 + 200 μM RPLPPLP, and 50 μM SH3 + 200 μM β3-NITYRGT. All fluorescence measurements were performed at 25°C in an Aviv Associates fluorometer. Samples were excited at 295 nm using a 2 nm band-pass filter and the emission spectrum was measured between 300 and 400 nm with 1 nm stepping and a 2 nm band-pass filter.

15N-1H HSQC NMR. SH3 grown in M9 minimal media supplemented with 15N NH$_4$Cl was transferred into pH 6.0 phosphate, 100 mM NaCl and concentrated to 1 mM. NMR data were collected on a Bruker DMX-600 spectrometer equipped with a 5-mm x,y,z-shielded pulse-field gradient triple-resonance probe (Bruker). Experiments were performed at 20 degrees Celsius. Assignments were based upon published c-Src SH3 chemical shifts (175). 1H-15N HSQC were acquired and analyzed in the Sparky software suite. Changes in chemical shift were calculated according to the relationship dCS = sqrt(dH^2+(dN/5)^2).

References

1. Metcalf DG*, et al.* (2010) NMR analysis of the alphaIIb beta3 cytoplasmic interaction suggests a mechanism for integrin regulation. *Proc Natl Acad Sci U S A* 107(52):22481-22486.
2. Moore DT*, et al.* (2012) Affinity of talin-1 for the beta3-integrin cytosolic domain is modulated by its phospholipid bilayer environment. *Proc Natl Acad Sci U S A* 109(3):793-798.
3. Grigoryan G, Moore DT, & DeGrado WF (2011) Transmembrane communication: general principles and lessons from the structure and function of the M2 proton channel, K channels, and integrin receptors. *Annu Rev Biochem* 80:211-237.
4. Kaushansky K (2008) Historical review: megakaryopoiesis and thrombopoiesis. *Blood* 111(3):981-986.
5. Bennett JS (2005) Structure and function of the platelet integrin alphaIIbbeta3. *J Clin Invest* 115(12):3363-3369.
6. Bennett JS, Berger BW, & Billings PC (2009) The structure and function of platelet integrins. *J Thromb Haemost* 7 Suppl 1:200-205.
7. Svensson L*, et al.* (2009) Leukocyte adhesion deficiency-III is caused by mutations in KINDLIN3 affecting integrin activation. *Nat Med* 15(3):306-312.
8. McDowall A*, et al.* (2010) Two mutations in the KINDLIN3 gene of a new leukocyte adhesion deficiency III patient reveal distinct effects on leukocyte function in vitro. *Blood* 115(23):4834-4842.
9. Manevich-Mendelson E*, et al.* (2009) Loss of Kindlin-3 in LAD-III eliminates LFA-1 but not VLA-4 adhesiveness developed under shear flow conditions. *Blood* 114(11):2344-2353.
10. Malinin NL*, et al.* (2009) A point mutation in KINDLIN3 ablates activation of three integrin subfamilies in humans. *Nat Med* 15(3):313-318.
11. George JN & Aster RH (2009) Drug-induced thrombocytopenia: pathogenesis, evaluation, and management. *Hematology Am Soc Hematol Educ Program*:153-158.
12. Abrams CS (2005) Intracellular signaling in platelets. *Curr Opin Hematol* 12(5):401-405.
13. Sebe-Pedros A, Roger AJ, Lang FB, King N, & Ruiz-Trillo I (2010) Ancient origin of the integrin-mediated adhesion and signaling machinery. *Proc Natl Acad Sci U S A* 107(22):10142-10147.
14. Li R*, et al.* (2003) Activation of integrin alphaIIbbeta3 by modulation of transmembrane helix associations. *Science* 300(5620):795-798.
15. Zhu J*, et al.* (2009) The structure of a receptor with two associating transmembrane domains on the cell surface: integrin alphaIIbbeta3. *Mol Cell* 34(2):234-249.

16. Yang J, *et al.* (2009) Structure of an integrin alphaIIb beta3 transmembrane-cytoplasmic heterocomplex provides insight into integrin activation. *Proc Natl Acad Sci U S A* 106(42):17729-17734.
17. Lau TL, Kim C, Ginsberg MH, & Ulmer TS (2009) The structure of the integrin alphaIIbbeta3 transmembrane complex explains integrin transmembrane signalling. *Embo J* 28(9):1351-1361.
18. Kim M, Carman CV, & Springer TA (2003) Bidirectional transmembrane signaling by cytoplasmic domain separation in integrins. *Science* 301(5640):1720-1725.
19. Moser M, Legate KR, Zent R, & Fassler R (2009) The tail of integrins, talin, and kindlins. *Science* 324(5929):895-899.
20. Shattil SJ, Kim C, & Ginsberg MH (2010) The final steps of integrin activation: the end game. *Nat Rev Mol Cell Biol* 11(4):288-300.
21. Petrich BG, *et al.* (2007) Talin is required for integrin-mediated platelet function in hemostasis and thrombosis. *J Exp Med* 204(13):3103-3111.
22. Moser M, Nieswandt B, Ussar S, Pozgajova M, & Fassler R (2008) Kindlin-3 is essential for integrin activation and platelet aggregation. *Nat Med* 14(3):325-330.
23. Arias-Salgado EG, *et al.* (2003) Src kinase activation by direct interaction with the integrin Œ≤ cytoplasmic domain. *Proceedings of the National Academy of Sciences of the United States of America* 100(23):13298-13302.
24. McLaughlin S & Murray D (2005) Plasma membrane phosphoinositide organization by protein electrostatics. *Nature* 438(7068):605-611.
25. Murray D, Ben-Tal N, Honig B, & McLaughlin S (1997) Electrostatic interaction of myristoylated proteins with membranes: simple physics, complicated biology. *Structure* 5(8):985-989.
26. Lemmon MA (2008) Membrane recognition by phospholipid-binding domains. *Nat Rev Mol Cell Biol* 9(2):99-111.
27. Murray D, *et al.* (1999) Electrostatic properties of membranes containing acidic lipids and adsorbed basic peptides: theory and experiment. *Biophys J* 77(6):3176-3188.
28. Ben-Tal N, Honig B, Peitzsch RM, Denisov G, & McLaughlin S (1996) Binding of small basic peptides to membranes containing acidic lipids: theoretical models and experimental results. *Biophys J* 71(2):561-575.
29. Murray D, *et al.* (1998) Electrostatics and the membrane association of Src: theory and experiment. *Biochemistry* 37(8):2145-2159.
30. Lemmon MA, Ferguson KM, O'Brien R, Sigler PB, & Schlessinger J (1995) Specific and high-affinity binding of inositol phosphates to an isolated pleckstrin homology domain. *Proc Natl Acad Sci U S A* 92(23):10472-10476.

31. Saltel F, *et al.* (2009) New PI(4,5)P2- and membrane proximal integrin-binding motifs in the talin head control beta3-integrin clustering. *J Cell Biol* 187(5):715-731.

32. Ling K, Doughman RL, Firestone AJ, Bunce MW, & Anderson RA (2002) Type I gamma phosphatidylinositol phosphate kinase targets and regulates focal adhesions. *Nature* 420(6911):89-93.

33. Goksoy E, *et al.* (2008) Structural basis for the autoinhibition of talin in regulating integrin activation. *Mol Cell* 31(1):124-133.

34. Wang Y, *et al.* (2008) Loss of PIP5KIgamma, unlike other PIP5KI isoforms, impairs the integrity of the membrane cytoskeleton in murine megakaryocytes. *J Clin Invest* 118(2):812-819.

35. Hynes RO (2002) Integrins: bidirectional, allosteric signaling machines. *Cell* 110(6):673-687.

36. Hughes PE, *et al.* (1996) Breaking the integrin hinge. A defined structural constraint regulates integrin signaling. *J Biol Chem* 271(12):6571-6574.

37. Li R, *et al.* (2002) Characterization of the monomeric form of the transmembrane and cytoplasmic domains of the integrin beta 3 subunit by NMR spectroscopy. *Biochemistry* 41(52):15618-15624.

38. Vinogradova O, *et al.* (2002) A structural mechanism of integrin alpha(IIb)beta(3) "inside-out" activation as regulated by its cytoplasmic face. *Cell* 110(5):587-597.

39. Weljie AM, Hwang PM, & Vogel HJ (2002) Solution structures of the cytoplasmic tail complex from platelet integrin alpha IIb- and beta 3-subunits. *Proc Natl Acad Sci U S A* 99(9):5878-5883.

40. Metcalf DG, Kulp DW, Bennett JS, & DeGrado WF (2009) Multiple approaches converge on the structure of the integrin alphaIIb/beta3 transmembrane heterodimer. *J Mol Biol* 392(4):1087-1101.

41. Li W, *et al.* (2005) A push-pull mechanism for regulating integrin function. *Proc Natl Acad Sci U S A* 102(5):1424-1429.

42. Rabanal F, DeGrado, W. F., Dutton, P. L. (1996) Use of 2,2'-dithiobis(5-nitropyridine) for the heterodimerization of cysteine containing pepties. . *Tetrahedron Letters* 37(9):1347-1350.

43. Senes A, *et al.* (2007) E(z), a depth-dependent potential for assessing the energies of insertion of amino acid side-chains into membranes: derivation and applications to determining the orientation of transmembrane and interfacial helices. *J Mol Biol* 366(2):436-448.

44. Garcia-Alvarez B, *et al.* (2003) Structural determinants of integrin recognition by talin. *Mol Cell* 11(1):49-58.

45. Tadokoro S, *et al.* (2003) Talin binding to integrin beta tails: a final common step in integrin activation. *Science* 302(5642):103-106.

46. Richardson JS & Richards DC (1988) Amino acid preferences for specific locations at the ends of alpha helices. *Science* 240(4859):1648-1652.

47. Kay LE, Torchia DA, & Bax A (1989) Backbone dynamics of proteins as studied by 15N inverse detected heteronuclear NMR spectroscopy: application to staphylococcal nuclease. *Biochemistry* 28(23):8972-8979.
48. Alexandrescu AT & Shortle D (1994) Backbone dynamics of a highly disordered 131 residue fragment of staphylococcal nuclease. *J Mol Biol* 242(4):527-546.
49. Englander SW & Mayne L (1992) Protein Folding Studied Using Hydrogen-Excange Labeling and 2-Dimensional NMR. *Annual Review of Biophysics and Biomolecular Structure* 21:243-265.
50. Joh NH*, et al.* (2008) Modest stabilization by most hydrogen-bonded side-chain interactions in membrane proteins. *Nature* 453(7199):1266-1270.
51. Downer NW & Englander SW (1975) Molecular structure of membrane-bound rhodopsin. *Nature* 254(5501):625-627.
52. Lau TL, Dua V, & Ulmer TS (2008) Structure of the integrin alphaIIb transmembrane segment. *J Biol Chem* 283(23):16162-16168.
53. Uversky VN & Dunker AK (2008) Biochemistry. Controlled chaos. *Science* 322(5906):1340-1341.
54. Vinogradova O*, et al.* (2004) Membrane-mediated structural transitions at the cytoplasmic face during integrin activation. *Proc Natl Acad Sci U S A* 101(12):4094-4099.
55. Elinder F, Nilsson J, & Arhem P (2007) On the opening of voltage-gated ion channels. *Physiol Behav* 92(1-2):1-7.
56. Long SB, Tao X, Campbell EB, & MacKinnon R (2007) Atomic structure of a voltage-dependent K+ channel in a lipid membrane-like environment. *Nature* 450(7168):376-382.
57. Traaseth NJ*, et al.* (2008) Structural and dynamic basis of phospholamban and sarcolipin inhibition of Ca(2+)-ATPase. *Biochemistry* 47(1):3-13.
58. Stouffer AL*, et al.* (2008) Structural basis for the function and inhibition of an influenza virus proton channel. *Nature* 451(7178):596-599.
59. Schnell JR & Chou JJ (2008) Structure and mechanism of the M2 proton channel of influenza A virus. *Nature* 451(7178):591-595.
60. Xu C*, et al.* (2008) Regulation of T cell receptor activation by dynamic membrane binding of the CD3epsilon cytoplasmic tyrosine-based motif. *Cell* 135(4):702-713.
61. Wegener KL*, et al.* (2007) Structural basis of integrin activation by talin. *Cell* 128(1):171-182.
62. Anthis NJ*, et al.* (2009) The structure of an integrin/talin complex reveals the basis of inside-out signal transduction. *Embo J* 28(22):3623-3632.
63. Bergamin E, Hallock PT, Burden SJ, & Hubbard SR (2010) The Cytoplasmic Adaptor Protein Dok7 Activates the Receptor Tyrosine Kinase MuSK via Dimerization. *Molecular Cell* 39(1):100-109.

64. Ye F*, et al.* (2010) Recreation of the terminal events in physiological integrin activation. *J Cell Biol* 188(1):157-173.

65. Walsh ST, Cheng H, Bryson JW, Roder H, & DeGrado WF (1999) Solution structure and dynamics of a de novo designed three-helix bundle protein. *Proc Natl Acad Sci U S A* 96(10):5486-5491.

66. Sattler M, Schleucher, J., Griesinger, C. (1999) Heteronuclear multidimensional NMR experiments for the structure determination of proteins in solution employing pulsed field gradients. *Progress in Nuclear Magnetic Resonance Spectroscopy* 34:93-158.

67. Wittekind M & Mueller L (1993) HNCACB, a high-sensitivity 3D NMR experiment to correlate amide-proton and nitrogen resonances with the alpha- and beta-carbon resonances in proteins. *J Magn Reson* 101:201-205.

68. Grzesiek S & Bax A (1992) Correlating backbone amide and side chain resonances in larger proteins by multiple relayed triple resonance. *J Am Chem Soc* 114:6291-6293.

69. Kay LE, Ikura M, Tschudin R, & Bax A (1990) Three-dimensional triple resonance NMR spectroscopy of isotopically enriched proteins. *J Magn Reson* 89:496-514.

70. Montelione GT, Lyons BA, Emerson M, & Tashiro M (1992) An efficient triple resonance experiment using carbon-13 isotropic mixing for determining sequence-specific resonance assignments of isotopically-enriched proteins. *J Am Chem Soc* 114:10974-10975.

71. Lyons BA, Tashiro M, Cedergren L, Bilsson B, & Montelione GT (1993) An improved strategy for determining resonance assignments for isotopically enriched proteins and its application to an engineered domain of staphylococcal protein A. *Biochemistry* 32(31):7839-7845.

72. Grzesiek S, Anglister J, & Bax A (1993) Correlation of backbone amide and aliphatic sidechain resonances in 13C/15N-enriched proteins by isotropic mixing of 13C magnetization. *J Magn Reson B* 101:114-119.

73. Logan TM, Olejniczak ET, Xu RX, & Fesik SW (1993) A general method for assigning NMR spectra of denatured proteins using 3D HC(CO)NH-TOCSY triple resonance experiments. *J Biomol NMR* 3(2):225-231.

74. Fesik SW*, et al.* (1990) 2D and 3D NMR spectroscopy employing carbon-13/carbon-13 magnetization transfer by isotropic mixing. Spin system identification in large proteins. *J Am Chem Soc* 112:886-888.

75. Bax A, Clore GM, & Gronenborn AM (1990) 1H-1H correlation via isotropic mixing of 13C magnetization: A new three-dimensional approach for assigning 1H and 13C spectra of 13C-enriched proteins. *J Magn Reson* 88:425-431.

76. Majumdar G, Wang H, Morshauser ERP, & Zuiderweg ER (1993) Sensitivity improvement in 2D and 3D HCCH spectroscopy using heteronuclear cross-polarization. *J Biomol NMR* 3:387-397.

77. Olejniczak ET, Xu RX, & Fesik SW (1992) A 4D HCCH-TOCSY experiment for assigning the side chain 1H and 13C resonances of proteins. *J Biomol NMR* 2(6):655-659.

78. Neri D, Szyperski T, Otting G, Senn H, & Wuthrich K (1989) Stereospecific nuclear magnetic resonance assignments of the methyl groups of valine and leucine in the DNA-binding domain of the 434 repressor by biosynthetically directed fractional 13C labeling. *Biochemistry* 28(19):7510-7516.

79. Yamazaki T, Forman-Kay JD, & Kay LE (1993) Two-dimensional NMR experiments for correlating carbon-13.beta. and proton.delta./.epsilon. chemical shifts of aromatic residues in 13C-labeled proteins via scalar couplings. *J Am Chem Soc* 115(23):11054-11055.

80. Ulrich EL*, et al.* (2008) BioMagResBank. *Nucleic Acids Res* 36(Database issue):D402-408.

81. Vuister GW & Bax A (1993) Quantitative J correlation: A new approach for measuring homonuclear three-bond J(HNHA) coupling constants in 15N-enriched proteins. *J Am Chem Soc* 115:7772-7777.

82. Pascal SM, Muhandiram DR, Yamazaki T, Forman-Kay JD, & Kay LE (1994) Simultaneous Acquisition of 15N- and 13C-Edited NOE Spectra of Proteins Dissolved in H2O. *J Magn Reson B* 103(2):197-201.

83. Chou JJ, Gaemers S, Howder B, Louis JM, & Bax A (2001) A simple apparatus for generating stretched polyacrylamide gels, yielding uniform alignment of proteins and detergent micelles. *J Biomol NMR* 21(4):377-382.

84. Herrmann T, Güntert P, & Wüthrich K (2002) Protein NMR structure determination with automated NOE assignment using the new software CANDID and the torsion angle dynamics algorithm DYANA. *J Mol Biol* 319(1):209-227.

85. Cornilescu G, Delaglio F, & Bax A (1999) Protein backbone angle restraints from searching a database for chemical shift and sequence homology. *J Biomol NMR* 13(3):289-302.

86. Shen Y, Delaglio F, Cornilescu G, & Bax A (2009) TALOS+: a hybrid method for predicting protein backbone torsion angles from NMR chemical shifts. *J Biomol NMR* 44(4):213-223.

87. Bartels C, Xia T-h, Billeter M, Güntert P, & Wüthrich K (1995) The program XEASY for computer-supported NMR spectral analysis of biological macromolecules. *Journal of Biomolecular NMR* 6(1):1-10.

88. Schwieters CD, Kuszewski JJ, Tjandra N, & Clore GM (2003) The Xplor-NIH NMR molecular structure determination package. *J Magn Reson* 160(1):65-73.

89. Berman HM*, et al.* (2000) The Protein Data Bank. *Nucleic Acids Res* 28(1):235-242.

90. Lipsitz RS, Sharma Y, Brooks BR, & Tjandra N (2002) Hydrogen bonding in high-resolution protein structures: a new method to assess NMR protein geometry. *J Am Chem Soc* 124(35):10621-10626.

91. Schwieters CD, Kuszewski JJ, & Clore GM (2006) Using Xplor-NIH for NMR molecular structure determination. *Progress in Nuclear Magnetic Resonance Spectroscopy* 48:47-62.

92. Bai YW, Milne JS, Mayne L, & Englander SW (1993) Primary Structure Effects on Peptide Group Hydrogen-Exchange. *Proteins-Structure Function and Genetics* 17(1):75-86.

93. Laskowski RA, Rullmannn JA, MacArthur MW, Kaptein R, & Thornton JM (1996) AQUA and PROCHECK-NMR: programs for checking the quality of protein structures solved by NMR. *J Biomol NMR* 8(4):477-486.

94. Word JM, Bateman RC, Jr., Presley BK, Lovell SC, & Richardson DC (2000) Exploring steric constraints on protein mutations using MAGE/PROBE. *Protein Sci* 9(11):2251-2259.

95. Luo BH, Carman CV, & Springer TA (2007) Structural basis of integrin regulation and signaling. *Annu Rev Immunol* 25:619-647.

96. Banno A & Ginsberg MH (2008) Integrin activation. *Biochem Soc Trans* 36(Pt 2):229-234.

97. Grigoryan G, Moore DT, & Degrado WF (2011) Transmembrane communication: general principles and lessons from the structure and function of the m2 proton channel, k(+) channels, and integrin receptors. *Annu Rev Biochem* 80:211-237.

98. Harburger DS & Calderwood DA (2009) Integrin signalling at a glance. *J Cell Sci* 122(Pt 2):159-163.

99. Critchley DR (2009) Biochemical and structural properties of the integrin-associated cytoskeletal protein talin. *Annu Rev Biophys* 38:235-254.

100. Kim C, Ye F, & Ginsberg MH (2011) Regulation of Integrin Activation. *Annu Rev Cell Dev Biol.*

101. Beckerle MC, Miller DE, Bertagnolli ME, & Locke SJ (1989) Activation-dependent redistribution of the adhesion plaque protein, talin, in intact human platelets. *J Cell Biol* 109(6 Pt 2):3333-3346.

102. Dietrich C, Goldmann WH, Sackmann E, & Isenberg G (1993) Interaction of NBD-talin with lipid monolayers. A film balance study. *FEBS Lett* 324(1):37-40.

103. Goldmann WH, Senger R, Kaufmann S, & Isenberg G (1995) Determination of the affinity of talin and vinculin to charged lipid vesicles: a light scatter study. *FEBS Lett* 368(3):516-518.

104. Elliott PR*, et al.* (2010) The Structure of the talin head reveals a novel extended conformation of the FERM domain. *Structure* 18(10):1289-1299.

105. Catimel B, *et al.* (2008) The PI(3,5)P2 and PI(4,5)P2 interactomes. *J Proteome Res* 7(12):5295-5313.
106. Kalli AC, *et al.* (2010) The structure of the talin/integrin complex at a lipid bilayer: an NMR and MD simulation study. *Structure* 18(10):1280-1288.
107. Goult BT, *et al.* (2009) The structure of an interdomain complex that regulates talin activity. *J Biol Chem* 284(22):15097-15106.
108. Anonymous (!!! INVALID CITATION !!!).
109. Fehon RG, McClatchey AI, & Bretscher A (2010) Organizing the cell cortex: the role of ERM proteins. *Nat Rev Mol Cell Biol* 11(4):276-287.
110. Frame MC, Patel H, Serrels B, Lietha D, & Eck MJ (2010) The FERM domain: organizing the structure and function of FAK. *Nat Rev Mol Cell Biol* 11(11):802-814.
111. Goult BT, *et al.* (2010) Structure of a double ubiquitin-like domain in the talin head: a role in integrin activation. *Embo J* 29(6):1069-1080.
112. Anthis NJ, Wegener KL, Critchley DR, & Campbell ID (2010) Structural diversity in integrin/talin interactions. *Structure* 18(12):1654-1666.
113. Mori T, *et al.* (2008) Structural basis for CD44 recognition by ERM proteins. *J Biol Chem* 283(43):29602-29612.
114. Calderwood DA, *et al.* (2002) The phosphotyrosine binding-like domain of talin activates integrins. *J Biol Chem* 277(24):21749-21758.
115. Narayan K & Lemmon MA (2006) Determining selectivity of phosphoinositide-binding domains. *Methods* 39(2):122-133.
116. Isenberg G, Niggli V, Pieper U, Kaufmann S, & Goldmann WH (1996) Probing phosphatidylinositolphosphates and adenosinenucleotides on talin nucleated actin polymerization. *FEBS Lett* 397(2-3):316-320.
117. Martel V, *et al.* (2001) Conformation, localization, and integrin binding of talin depend on its interaction with phosphoinositides. *J Biol Chem* 276(24):21217-21227.
118. Schuck P & Zhao H (2010) The role of mass transport limitation and surface heterogeneity in the biophysical characterization of macromolecular binding processes by SPR biosensing. *Methods Mol Biol* 627:15-54.
119. de Pereda JM, *et al.* (2005) Structural basis for phosphatidylinositol phosphate kinase type Igamma binding to talin at focal adhesions. *J Biol Chem* 280(9):8381-8386.
120. Kong X, Wang X, Misra S, & Qin J (2006) Structural basis for the phosphorylation-regulated focal adhesion targeting of type Igamma phosphatidylinositol phosphate kinase (PIPKIgamma) by talin. *J Mol Biol* 359(1):47-54.

121. Yin H*, et al.* (2006) Activation of platelet alpha IIb beta 3 by an exogenous peptide corresponding to the transmembrane domain of alpha IIb. *Journal of Biological Chemistry* 281(48):36732-36741.
122. Csermely P, Palotai R, & Nussinov R (2010) Induced fit, conformational selection and independent dynamic segments: an extended view of binding events. *Trends Biochem Sci* 35(10):539-546.
123. Monod J (1966) From enzymatic adaptation to allosteric transitions. *Science* 154(748):475-483.
124. Monod J, Wyman J, & Changeux JP (1965) On The Nature Of Allosteric Transitions: A Plausible Model. *J Mol Biol* 12:88-118.
125. Boehr DD, Nussinov R, & Wright PE (2009) The role of dynamic conformational ensembles in biomolecular recognition. *Nat Chem Biol* 5(11):789-796.
126. Koshland DE, Jr., Nemethy G, & Filmer D (1966) Comparison of experimental binding data and theoretical models in proteins containing subunits. *Biochemistry* 5(1):365-385.
127. Hill AV (1922) The possible effects of the aggregation of the molecules of huemoglobin on its dissociation curves. *J Physiol* 40:iv-vii.
128. Liu Z, Gandhi CS, & Rees DC (2009) Structure of a tetrameric MscL in an expanded intermediate state. *Nature* 461(7260):120-124.
129. Schmidt D, Cross SR, & MacKinnon R (2009) A gating model for the archeal voltage-dependent K(+) channel KvAP in DPhPC and POPE:POPG decane lipid bilayers. *J Mol Biol* 390(5):902-912.
130. Schmidt D, Jiang QX, & MacKinnon R (2006) Phospholipids and the origin of cationic gating charges in voltage sensors. *Nature* 444(7120):775-779.
131. Nishida M, Cadene M, Chait BT, & MacKinnon R (2007) Crystal structure of a Kir3.1-prokaryotic Kir channel chimera. *EMBO J* 26(17):4005-4015.
132. Luo W, Cady SD, & Hong M (2009) Immobilization of the influenza A M2 transmembrane peptide in virus envelope-mimetic lipid membranes: a solid-state NMR investigation. *Biochemistry* 48(27):6361-6368.
133. Schroeder C, Heider H, Moncke-Buchner E, & Lin TI (2005) The influenza virus ion channel and maturation cofactor M2 is a cholesterol-binding protein. *Eur Biophys J* 34(1):52-66.
134. Schroeder C (2010) Cholesterol-binding viral proteins in virus entry and morphogenesis. *Subcell Biochem* 51:77-108.
135. Lin YH, Gao R, Binns AN, & Lynn DG (2008) Capturing the VirA/VirG TCS of Agrobacterium tumefaciens. *Adv Exp Med Biol* 631:161-177.
136. Bennett JS & Moore DT (2010) Regulation of platelet beta 3 integrins. *Haematologica* 95(7):1049-1051.

137. Ablooglu AJ, Kang J, Petrich BG, Ginsberg MH, & Shattil SJ (2009) Antithrombotic effects of targeting alphaIIbbeta3 signaling in platelets. *Blood* 113(15):3585-3592.

138. Cox D, Brennan M, & Moran N (2010) Integrins as therapeutic targets: lessons and opportunities. *Nat Rev Drug Discov* 9(10):804-820.

139. Luo B-H, Carman CV, Takagi J, & Springer TA (2005) Disrupting integrin transmembrane domain heterodimerization increases ligand binding affinity, not valency or clustering. *Proceedings of the National Academy of Sciences* 102(10):3679-3684.

140. Berger BW*, et al.* (2010) Consensus motif for integrin transmembrane helix association. *Proc Natl Acad Sci U S A* 107(2):703-708.

141. Luo BH, Springer TA, & Takagi J (2004) A specific interface between integrin transmembrane helices and affinity for ligand. *Plos Biology* 2(6):776-786.

142. Zhu J*, et al.* (2007) Requirement of alpha and beta subunit transmembrane helix separation for integrin outside-in signaling. *Blood* 110(7):2475-2483.

143. Xie C*, et al.* (2010) Structure of an integrin with an alphaI domain, complement receptor type 4. *Embo J* 29(3):666-679.

144. Donald JE, Zhu H, Litvinov RI, Degrado WF, & Bennett JS (2010) Identification of interacting hotspots in the {beta}3 integrin stalk using comprehensive interface design. *J Biol Chem*.

145. Xiao T, Takagi J, Coller BS, Wang JH, & Springer TA (2004) Structural basis for allostery in integrins and binding to fibrinogen-mimetic therapeutics. *Nature* 432(7013):59-67.

146. Xiong JP*, et al.* (2001) Crystal structure of the extracellular segment of integrin alpha Vbeta3. *Science* 294(5541):339-345.

147. Zhu J*, et al.* (2008) Structure of a complete integrin ectodomain in a physiologic resting state and activation and deactivation by applied forces. *Mol Cell* 32(6):849-861.

148. Xiong JP*, et al.* (2002) Crystal structure of the extracellular segment of integrin alpha Vbeta3 in complex with an Arg-Gly-Asp ligand. *Science* 296(5565):151-155.

149. Shimaoka M, Salas A, Yang W, Weitz-Schmidt G, & Springer TA (2003) Small molecule integrin antagonists that bind to the beta2 subunit I-like domain and activate signals in one direction and block them in the other. *Immunity* 19(3):391-402.

150. Chen X*, et al.* (2010) Requirement of open headpiece conformation for activation of leukocyte integrin alphaXbeta2. *Proc Natl Acad Sci U S A* 107(33):14727-14732.

151. Ulmer TS, Yaspan B, Ginsberg MH, & Campbell ID (2001) NMR analysis of structure and dynamics of the cytosolic tails of integrin alpha IIb beta 3 in aqueous solution. *Biochemistry* 40(25):7498-7508.

152. Takagi J, Petre BM, Walz T, & Springer TA (2002) Global conformational rearrangements in integrin extracellular domains in outside-in and inside-out signaling. *Cell* 110(5):599-611.
153. Hantgan RR, Stahle MC, & Lord ST (2010) Dynamic Regulation of Fibrinogen: Integrin alphaIIbbeta3 Binding. *Biochemistry*.
154. Shimaoka M*, et al.* (2003) Structures of the alpha L I domain and its complex with ICAM-1 reveal a shape-shifting pathway for integrin regulation. *Cell* 112(1):99-111.
155. Bledzka K*, et al.* (2010) Tyrosine phosphorylation of integrin beta3 regulates kindlin-2 binding and integrin activation. *J Biol Chem* 285(40):30370-30374.
156. Yeatman TJ (2004) A renaissance for SRC. *Nat Rev Cancer* 4(6):470-480.
157. Kim LC, Song L, & Haura EB (2009) Src kinases as therapeutic targets for cancer. *Nat Rev Clin Oncol* 6(10):587-595.
158. Lowell CA & Soriano P (1996) Knockouts of Src-family kinases: stiff bones, wimpy T cells, and bad memories. *Genes Dev* 10(15):1845-1857.
159. Stehelin D, Varmus HE, Bishop JM, & Vogt PK (1976) DNA related to the transforming gene(s) of avian sarcoma viruses is present in normal avian DNA. *Nature* 260(5547):170-173.
160. Obergfell A*, et al.* (2002) Coordinate interactions of Csk, Src, and Syk kinases with [alpha]IIb[beta]3 initiate integrin signaling to the cytoskeleton. *J Cell Biol* 157(2):265-275.
161. Pumiglia KM & Feinstein MB (1993) Thrombin and thrombin receptor agonist peptide induce tyrosine phosphorylation and tyrosine kinases in the platelet cytoskeleton. Translocation of pp60c-src and integrin alpha IIb beta 3 (glycoprotein IIb/IIIa) is not required for aggregation, but is dependent on formation of large aggregate structures. *Biochem J* 294 (Pt 1):253-260.
162. Clark EA & Brugge JS (1993) Redistribution of activated pp60c-src to integrin-dependent cytoskeletal complexes in thrombin-stimulated platelets. *Mol Cell Biol* 13(3):1863-1871.
163. Xu W, Harrison SC, & Eck MJ (1997) Three-dimensional structure of the tyrosine kinase c-Src. *Nature* 385(6617):595-602.
164. Levinson NM, Seeliger MA, Cole PA, & Kuriyan J (2008) Structural basis for the recognition of c-Src by its inactivator Csk. *Cell* 134(1):124-134.
165. Arias-Salgado EG*, et al.* (2005) PTP-1B is an essential positive regulator of platelet integrin signaling. *J Cell Biol* 170(5):837-845.
166. Resh MD (1999) Fatty acylation of proteins: new insights into membrane targeting of myristoylated and palmitoylated proteins. *Biochim Biophys Acta* 1451(1):1-16.
167. Sato I*, et al.* (2009) Differential trafficking of Src, Lyn, Yes and Fyn is specified by the state of palmitoylation in the SH4 domain. *J Cell Sci* 122(Pt 7):965-975.

168. Miller WT (2003) Determinants of substrate recognition in nonreceptor tyrosine kinases. *Acc Chem Res* 36(6):393-400.
169. Thomas JW*, et al.* (1998) SH2- and SH3-mediated interactions between focal adhesion kinase and Src. *J Biol Chem* 273(1):577-583.
170. Sakai R*, et al.* (1994) A novel signaling molecule, p130, forms stable complexes in vivo with v-Crk and v-Src in a tyrosine phosphorylation-dependent manner. *Embo J* 13(16):3748-3756.
171. Nakamoto T, Sakai R, Ozawa K, Yazaki Y, & Hirai H (1996) Direct binding of C-terminal region of p130Cas to SH2 and SH3 domains of Src kinase. *J Biol Chem* 271(15):8959-8965.
172. Zou Z, Chen H, Schmaier AA, Hynes RO, & Kahn ML (2007) Structure-function analysis reveals discrete beta3 integrin inside-out and outside-in signaling pathways in platelets. *Blood* 109(8):3284-3290.
173. Li SS (2005) Specificity and versatility of SH3 and other proline-recognition domains: structural basis and implications for cellular signal transduction. *Biochem J* 390(Pt 3):641-653.
174. Feng S, Kasahara C, Rickles RJ, & Schreiber SL (1995) Specific interactions outside the proline-rich core of two classes of Src homology 3 ligands. *Proc Natl Acad Sci U S A* 92(26):12408-12415.
175. Yu H*, et al.* (1994) Structural basis for the binding of proline-rich peptides to SH3 domains. *Cell* 76(5):933-945.
176. Woody RW (1995) Circular dichroism. *Methods Enzymol* 246:34-71.
177. Okishio N, Tanaka T, Fukuda R, & Nagai M (2003) Differential ligand recognition by the Src and phosphatidylinositol 3-kinase Src homology 3 domains: circular dichroism and ultraviolet resonance Raman studies. *Biochemistry* 42(1):208-216.
178. Viguera AR, Arrondo JL, Musacchio A, Saraste M, & Serrano L (1994) Characterization of the interaction of natural proline-rich peptides with five different SH3 domains. *Biochemistry* 33(36):10925-10933.
179. Takeuchi K & Wagner G (2006) NMR studies of protein interactions. *Curr Opin Struct Biol* 16(1):109-117.
180. Alexandropoulos K & Baltimore D (1996) Coordinate activation of c-Src by SH3- and SH2-binding sites on a novel p130Cas-related protein, Sin. *Genes Dev* 10(11):1341-1355.
181. Arias-Salgado EG, Lizano S, Shattil SJ, & Ginsberg MH (2005) Specification of the direction of adhesive signaling by the integrin beta cytoplasmic domain. *J Biol Chem* 280(33):29699-29707.
182. Su X*, et al.* (2008) RGT, a synthetic peptide corresponding to the integrin beta 3 cytoplasmic C-terminal sequence, selectively inhibits outside-in signaling in human platelets by disrupting the interaction of integrin alpha IIb beta 3 with Src kinase. *Blood* 112(3):592-602.